

REPORT DOCUMENTATION PAGE				Form Approved OMB No. 0704-0188	
Public reporting burden for this collection of information is estimated to average 1 hour per response, including the time for reviewing instructions, searching existing data sources, gathering and maintaining the data needed, and completing and reviewing this collection of information. Send comments regarding this burden estimate or any other aspect of this collection of information, including suggestions for reducing this burden to Department of Defense, Washington Headquarters Services, Directorate for Information Operations and Reports (0704-0188), 1215 Jefferson Davis Highway, Suite 1204, Arlington, VA 22202-4302. Respondents should be aware that notwithstanding any other provision of law, no person shall be subject to any penalty for failing to comply with a collection of information if it does not display a currently valid OMB control number. PLEASE DO NOT RETURN YOUR FORM TO THE ABOVE ADDRESS.					
1. REPORT DATE (DD-MM-YYYY) 11-01-2010		2. REPORT TYPE Final Technical		3. DATES COVERED (From - To) 01-11-2006 to 30-11-2009	
4. TITLE AND SUBTITLE (U) Laser Diagnostics for Reacting Flows				5a. CONTRACT NUMBER	
				5b. GRANT NUMBER FA9550-07-1-0020	
				5c. PROGRAM ELEMENT NUMBER 61102F	
6. AUTHOR(S) Ronald K Hanson				5d. PROJECT NUMBER 2308	
				5e. TASK NUMBER BX	
				5f. WORK UNIT NUMBER	
7. PERFORMING ORGANIZATION NAME(S) AND ADDRESS(ES) Mechanical Engineering Department Stanford University Stanford CA 94305-3030				8. PERFORMING ORGANIZATION REPORT NUMBER	
9. SPONSORING / MONITORING AGENCY NAME(S) AND ADDRESS(ES) Air Force Office of Scientific Research 875 North Randolph Street Suite 325, Room 3112 Arlington VA 22203-1768				10. SPONSOR/MONITOR'S ACRONYM(S)	
				11. SPONSOR/MONITOR'S REPORT NUMBER(S)	
12. DISTRIBUTION / AVAILABILITY STATEMENT Approved for public release. Distribution is unlimited.					
13. SUPPLEMENTARY NOTES					
14. ABSTRACT Advanced optical diagnostic techniques relevant to propulsion were investigated. The techniques studied were based on laser spectroscopy, with emphasis on spectrally-resolved absorption and laser-induced fluorescence (LIF). Laser sources included tunable CW near-infrared (NIR) diode lasers and tunable (or fixed-wavelength) pulsed lasers operated at ultraviolet (UV) wavelengths. Accomplishments of note included: (1) development of a new pressure- and temperature-dependent database for tracer-based planar laser induced fluorescence (PLIF) imaging with 3-pentanone, (2) the first demonstration of high-speed PLIF using CW excitation, (3) development and demonstration of new tracer-based PLIF strategies for imaging interactions of high-speed flows with obstacles and boundary layers, (4) the extension of advanced wavelength-multiplexed diode laser sensing to absorption transitions of H ₂ O and CO ₂ in the extended NIR through use of newly available diode laser sources, (5) extension of diode laser absorption sensing to high-pressure environments, (6) the demonstration of wavelength-multiplexed strategies for quantitative measurements of hydrocarbon fuels in the presence of liquid fuel aerosols and liquid fuel films, and (7) applications of tunable-diode-laser (TDL) absorption sensors in scramjet flows at the AFRL at Wright-Patterson AFB using wavelength-multiplexed lasers and <i>I</i> _f -normalized, wavelength modulation spectroscopy with a 2 <i>f</i> detection strategy. The full spectrum of results for the reporting period was published in thirty-six papers in the peer-reviewed literature, five PhD theses, and thirty-two presentations and invited lectures.					
15. SUBJECT TERMS Laser Diagnostics, Combustion, Propulsion, Absorption, Fluorescence, Temperature, High Pressure					
16. SECURITY CLASSIFICATION OF:			17. LIMITATION OF ABSTRACT	18. NUMBER OF PAGES	19a. NAME OF RESPONSIBLE PERSON
a. REPORT	b. ABSTRACT	c. THIS PAGE			Julian Tishkoff
Unclassified	Unclassified	Unclassified	UL	84	19b. TELEPHONE NUMBER (include area code) 703-696-8478



Final Technical Report

LASER DIAGNOSTICS FOR REACTING FLOWS

Grant AFOSR FA9550-07-1-0020

Prepared for
Air Force Office of Scientific Research
Dr. Julian Tishkoff, Technical Monitor

For the Period
December 1, 2006 to November 30, 2009

Submitted by
Professor Ronald K. Hanson, Principal Investigator

HIGH TEMPERATURE GASDYNAMICS LABORATORY
Mechanical Engineering Department
Stanford University, Stanford CA 94305

H
T
G
L

Cover.....	2
1.0 Abstract.....	4
2.0 Project Summaries	5
2.1 Tracer Photophysics.....	5
2.1.1 Background.....	5
2.1.2 Absorption Cross Section	6
2.1.3 Fluorescence Quantum Yield.....	8
2.2 High-Speed PLIF/LIF Using CW Excitation.....	11
2.2.1 Background.....	11
2.2.2 Characterization of Toluene-Based CW PLIF	12
2.2.3 CW PLIF Experimental Setup	12
2.2.4 CW PLIF Performance	13
2.2.5 CW PLIF Application to a Turbulent Jet.....	15
2.3 PLIF Imaging in Shock Tube Flows.....	17
2.3.1 PLIF of Temperature in a Shock Tube	18
2.3.2 PLIF of a Supersonic Flow Temperature Over a Wedge.....	20
2.4 Tunable Diode Laser Diagnostics with Extended NIR Devices.....	22
2.4.1. Single-Laser H ₂ O and Temperature Sensor near 2.5 μm	22
2.4.2. CO ₂ Concentration and Temperature Sensor near 2.7 μm	26
2.4.3 T Measurements Behind Reflected Shock Waves Using WMS	30
2.5 Extended NIR TDL Absorption at High Pressures.....	35
2.5.1. CO ₂ Concentration and T at High Pressure Using WMS-2f/1f.....	35
2.5.2. Line Mixing and Finite Duration Collision Effects	40
2.6 Multi-Wavelength MIR Fuel Diagnostics	45
2.6.1 FTIR Spectroscopy	47
2.6.2 Vapor-Phase Fuel Diagnostics.....	51
2.6.3 Multi-Phase Fuel Measurements.....	55
2.7 Applications of TDL Sensors to Scramjets at AFRL.....	62
2.7.1 Calibration-Free <i>I_f</i> -normalized WMS-2f Sensors	62
2.7.2 Sensor Used for AFRL Scramjet Measurements	65
2.7.3 CO ₂ /H ₂ O Concentration in a Vitiated Supersonic Flow	67
2.7.4 Comparison of TDL LOS Measurements with 2D CFD	68
2.7.5 Fluctuations in Temperature Non-Uniformity Predict Unstart.....	69
2.8 References.....	72
3 Publications and Presentations.....	76
3.1 AFOSR Sponsored Publications.....	76
3.2 Refereed and AIAA Publications to appear 2010.....	78
3.3 Ph.D. Theses with AFOSR Support 2007-2009	79
3.4 Participation/Presentations at Meetings, Conferences, Seminars	79
4 Personnel.....	82
5 Interactions and Collaboration with AFRL.....	82
6 New Discoveries, Inventions, Patent Disclosures.....	83
7 Honors/Awards	84

1.0 Abstract

Advanced optical diagnostic techniques relevant to propulsion were investigated. The techniques studied were based on laser spectroscopy, with emphasis on spectrally-resolved absorption and laser-induced fluorescence (LIF). Laser sources included tunable, continuous-wave (CW) near-infrared (NIR) diode lasers and tunable (or fixed-wavelength) pulsed lasers operated at ultraviolet (UV) wavelengths. The CW lasers were spectrally narrow, allowing study of innovative diagnostics based on spectral lineshapes, while the pulsed lasers provided intense bursts of photons needed for techniques based on LIF. Accomplishments of note included: (1) development of a new pressure- and temperature-dependent database for tracer-based planar laser induced fluorescence (PLIF) imaging with 3-pentanone, (2) the first demonstration of high-speed PLIF using CW excitation, (3) development and demonstration of new tracer-based PLIF strategies for imaging interactions of high-speed flows with obstacles and boundary layers, (4) the extension of advanced wavelength-multiplexed diode laser sensing to absorption transitions of H_2O and CO_2 in the extended NIR through use of newly available diode laser sources, (5) extension of diode laser absorption sensing to high-pressure environments, (6) the demonstration of wavelength-multiplexed strategies for quantitative measurements of hydrocarbon fuels in the presence of liquid fuel aerosols and liquid fuel films, and (7) applications of tunable-diode-laser (TDL) absorption sensors in scramjet flows at the AFRL at Wright-Patterson AFB using wavelength-multiplexed lasers and $1f$ -normalized, wavelength modulation spectroscopy with a $2f$ detection strategy. The full spectrum of results for the reporting period was published in thirty-six papers in the AIAA proceedings and peer-reviewed literature, five PhD theses, and thirty-two presentations and invited lectures.

2.0 Project Summaries

2.1 Tracer Photophysics

2.1.1 Background

Tracer-based planar laser induced fluorescence (PLIF) has a long history as a diagnostic for assessing temperature fields, as well as fuel-mixing behavior, in combustion systems [1]. 3-pentanone is used commonly as a tracer due to its ease of use, similar boiling point compared to iso-octane, and relative simplicity in interpreting LIF results; however, the accuracy of 3-pentanone PLIF measurements depends on understanding of the detailed photophysics of 3-pentanone molecules. During the past grant period significant progress was made in the development of a database for the high-pressure, high-temperature photophysics of 3-pentanone

The PLIF signal can be described by the fluorescence equation

$$S_f = \frac{E\lambda}{hc} \frac{\chi p}{k_b T} L \sigma(\lambda, T) \phi(\lambda, p, T) \frac{\Omega}{4\pi} \eta \quad (2.1.1)$$

where E is the incident laser energy, λ is the laser wavelength, p is the total pressure, T is the temperature, χ is the mole fraction of fluorescing tracer, L is the length of the illuminated volume, Ω is the detector collection angle, and η is the detector collection efficiency. The fluorescence quantum yield (FQY) ϕ and absorption cross-section σ are photophysical parameters specific to each tracer. Interpretation of PLIF results depends on knowledge of the variation of these parameters with excitation wavelength, temperature, and pressure.

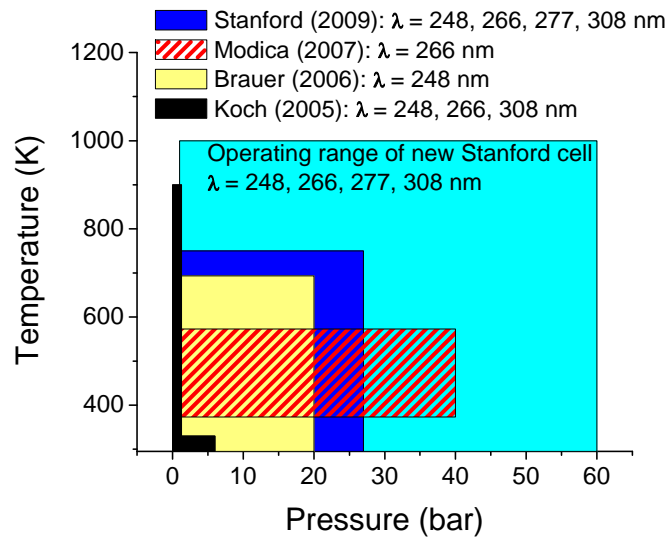


Figure 2.1.1 Conditions of previous work and capabilities of new Stanford setup.

Previous measurements of 3-pentanone photophysics, in particular the FQY, were made over limited ranges of temperature and pressure; Fig. 2.1.1 shows the temperature and pressure ranges that previous studies of FQY have covered [2,3,4]. Additional photophysics data at high pressure and high temperature are important for accurate interpretation of PLIF diagnostic measurements in harsh, high-pressure, high-temperature applications. In addition, these data are useful for creating accurate photophysical models for 3-pentanone at various pressure and temperature conditions.

2.1.2 Absorption Cross Section

The absorption spectrum for both acetone and 3-pentanone was measured in the reflected shock region of a shock tube at various elevated temperatures with broadband UV light using the experimental setup shown in Fig. 2.1.2, as was described in detail in Ref. 5. A mixture of 4% 3-pentanone in argon was fed into the driven end of the shock tube at pressures ranging from 60 to 220 mbar. The post-shock temperature ranged from 540 K to 1090 K, and post shock-pressure ranged from 1 to 2 bar.

The optical measurements used UV-grade fused-silica windows located 2.0 cm from the endwall. Light from a deuterium lamp was collimated using a lens and passed through the shock tube. The light exiting the shock tube, after being absorbed by the tracer, was focused using a lens onto the entry slit of a spectrograph. The output from the spectrograph was imaged using a kinetic-readout frame transfer CCD camera with a 512 x 1024 pixel array. The spectral resolution of the spectrograph-CCD system was 2.6 nm full width half maximum (FWHM).

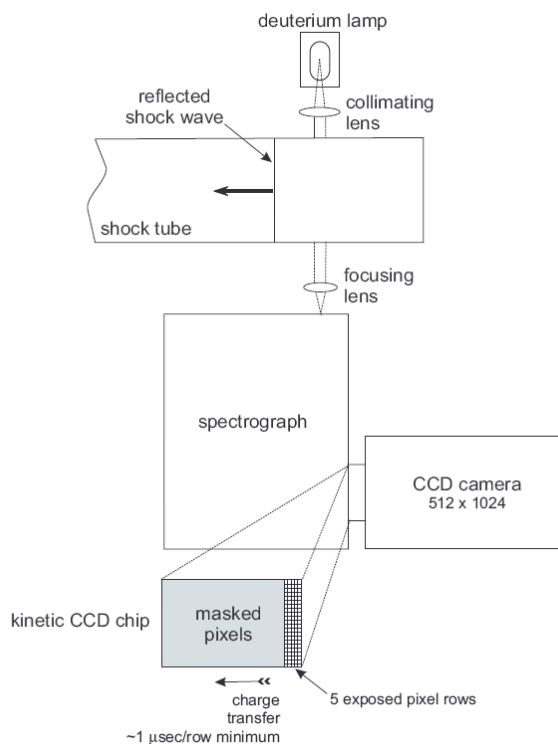


Figure 2.1.2 Experimental setup for absorption spectrum measurements.

The absorption cross section was derived by comparing the measured spectrum of light exiting the shock tube before the shock tube was filled with the tracer argon mixture (I), and the measured spectrum after the shock heating of the mixture (I_0). The absorption cross section (cm^2/molec) was determined with the Beer-Lambert equation:

$$\sigma(\lambda) = -\frac{1}{nL} \ln \left(\frac{I(\lambda)}{I_0(\lambda)} \right), \quad (2.1.2)$$

where n represents the number density of the tracer during the post-reflected-shock conditions and L is the pathlength, 15.2 cm.

Figure 2.1.3 shows the measured 3-pentanone absorption spectrum for five temperatures between 300 K and 875 K. The room temperature spectrum agreed well with previous data. The measured absorption cross sections agreed well with cell-based measurements at elevated temperature with 248, 266, and 308 nm laser excitation. We found that the peak absorption cross section increased by nearly a factor of two as the temperature was increased from 300 K to 1090 K. In addition, the wavelength of the peak cross section shifted to the red by about 10 nm over this temperature range. These dramatic changes to the spectrum occur to the red of 270 nm; between 220 and 265 nm, there was little change in magnitude of the absorption cross section with temperature.

A Gaussian profile described the shape of the absorption spectrum, and a Gaussian expression with semi-empirical parameters was fit to predict the absorption cross section as a function of wavelength and temperature:

$$\sigma = A(T) \exp \left(- \left(\frac{\lambda - \lambda_c}{w(T)} \right)^2 \right) \quad (2.1.3)$$

In this expression, A is the amplitude, w is the characteristic width, and λ_c is the center wavelength. Temperature-dependent expressions for these three parameters are shown in Table 1.1.

Table 1.1 Fitting coefficients for the temperature-dependent absorption spectra of acetone and 3-pentanone for 230–330 nm, 300–1040K

Parameter	$A(T)$, 10^{-20} cm^2	$\lambda_c(T)$, nm	$w(T)$, nm
Acetone	$3.43 + 0.00482 \times T \text{ [K]}$	$271.4 + 0.0156 \times T \text{ [K]}$	$26.8 + 0.00950 \times T \text{ [K]}$
3-Pentanone	$4.77 + 0.00487 \times T \text{ [K]}$	$273.7 + 0.0186 \times T \text{ [K]}$	$25.1 + 0.0101 \times T \text{ [K]}$

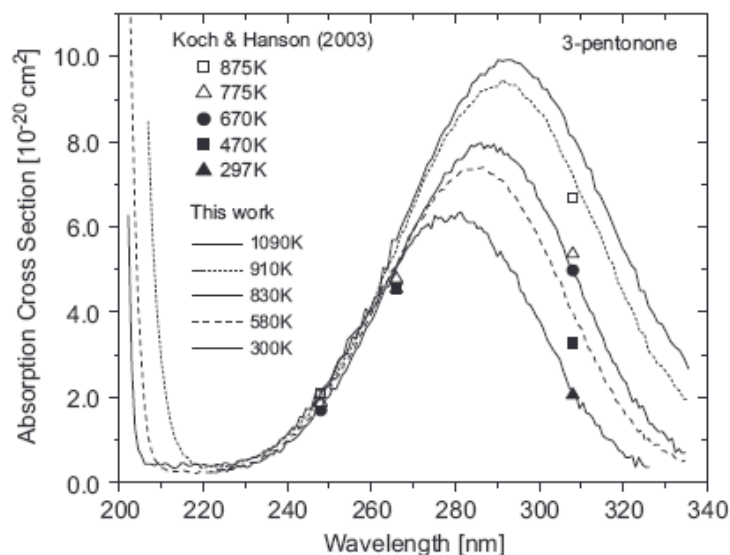


Figure 2.1.3 Absorption spectra of 3-pentanone at high temperatures.

2.1.3 Fluorescence Quantum Yield

Precision measurements of the fluorescence quantum yield (FQY) were made with laser excitation utilizing a new high-pressure, high-temperature flowing cell facility, as shown in Fig. 2.1.4. A flowing stream of nitrogen or air, seeded with 3-pentanone, was passed through the cell. The flow of the nitrogen or air was controlled using a mass flow controller. Liquid 3-pentanone was introduced into the flow stream using a metering pump and was evaporated by heating the surrounding plumbing to ~ 370 K. A baffled chamber was located downstream of the introduction point to mix the stream completely. Pressure was controlled by a needle valve located downstream of the cell. The cell itself was located inside an oven to control the temperature of the cell. Measurements of FQY were made for temperatures from 300 to 750 K over a range of pressures from 1 to 25 bar. The partial pressure of 3-pentanone in these measurements was 20 mbar.

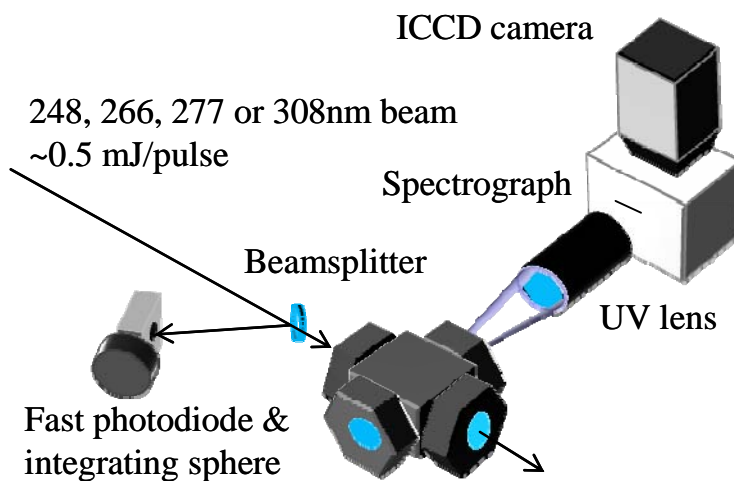


Figure 2.1.4 Experimental setup for measurements of FQY at high temperature and pressure.

The laser beam (1 mm diameter, ~0.5 mJ/pulse) was passed through sapphire windows (1.27 cm diameter). The pulse-to-pulse beam energy was monitored using a fast Si photodiode with an integrating sphere. The fluorescence signal was collected through a window orthogonal to the laser beam with a UV-grade fused-silica lens and imaged onto the entry slit of a spectrograph. A 320 nm high-pass filter was placed in front of the UV lens to reject the Rayleigh scattering of laser beam. The output of the spectrograph was imaged by an intensified ICCD camera with a 512 x 512 pixel array. The measured fluorescence spectrum was integrated from 320 nm to 565 nm to determine total fluorescence signal. Measurements were divided by number density and absorption to determine relative FQY. The relative FQY measurements were scaled to absolute values using previous measurements of absolute FQY made at Stanford [6].

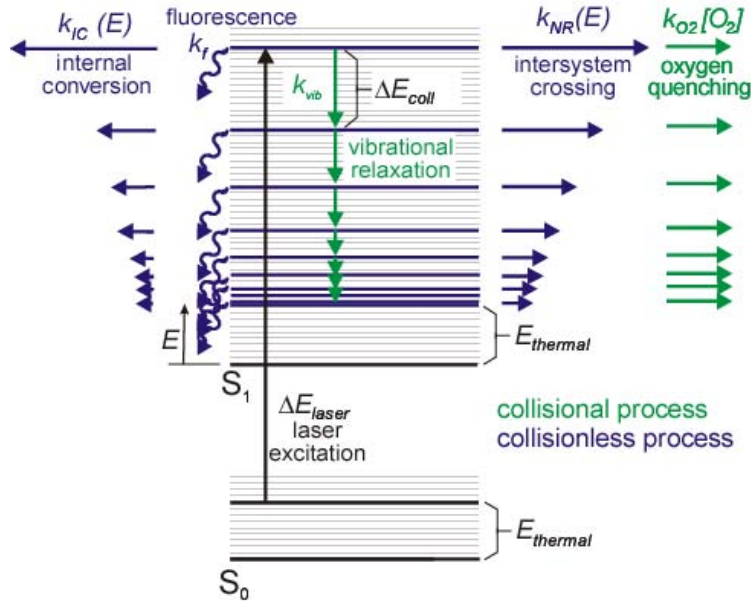


Figure 2.1.5 3-pentanone fluorescence model diagram.

The measured FQY values were used to improve our understanding of the photophysical process of 3-pentanone LIF. The multistep decay model for FQY developed previously at Stanford is described graphically in Fig. 2.1.5 [7]. The laser photon excites the molecule from the S_0 state to an upper vibrational level with energy E in the S_1 state. In the S_1 state, in addition to fluorescence, the molecule can undergo several processes. Once in the upper state, the molecule can fluoresce, undergo intersystem crossing (ISC) to the triplet state T_1 , undergo internal conversion (IC) to the upper vibrational levels of the S_0 state, or vibrationally relax via collisions. The molecule also can be removed from the excited electronic state by oxygen quenching. The probability of a molecule fluorescing from a particular vibrational level with energy E_n in the S_1 state is the ratio of the fluorescence rate to the total rates of all processes. The fluorescence yield is the sum of these fluorescence probabilities weighted by the probability that a molecule is in the vibrational level:

$$\phi = \sum_{n=0}^{\infty} \frac{k_f}{k_f + k_{vib} + k_{nr}(E_n) + k_{ic}(E_n) + k_{O_2}(E_n, n_{O_2})} p(E_n)$$

In this expression k_f is the fluorescence rate, k_{vib} is the collision rate, k_{nr} is the ISC rate, k_{ic} is the IC rate, and k_{O_2} is the oxygen quenching rate. $p(E_n)$ is the probability the molecule is in a vibrational level with energy E_n .

Vibrational relaxation affects the probability that a molecule is in a particular vibrational level. This model assumes that the molecule steps one collision at a time through the vibrational levels according to the following expression:

$$E_{n+1} = E_n - \Delta E_{coll} = E_n - \alpha(T)[E_n - E_{thermal}]$$

$E_{thermal}$ is the equilibrium vibrational energy in the upper electronic state, and $\alpha(T)$ is a temperature and collision partner-dependent proportionality constant.

Koch in 2005 determined a preliminary set of the model parameters using 3-pentanone FQY data taken for limited range of temperature and pressure. During the past grant period, the model parameters were updated using our new high-pressure and high-temperature FQY data following 277 and 308 nm excitation. The parameters for the model are summarized in Table 1.2.

Table 1.2 Updated model parameters using high pressure and high temperature FQY data with 277 and 308 nm excitation

Parameter	Value or Expression
$k_f (1/s)$	4.15×10^5
$k_{nr} (1/s)$	$k_{nr} = 4.77 \times 10^8 - 1.38 \times 10^5 E + 8.11 \times 10^1 E^2 - 2.53 \times 10^{-2} E^3 + 4.07 \times 10^{-6} E^4 - 3.08 \times 10^{-10} E^5 + 9.01 \times 10^{-15} E^6$
a_{N_2}	$\alpha_{N_2} = 0.0039 \left(\frac{T}{300} \right)^{-1.2}$
a_{O_2}	$\alpha_{O_2} = 0.0528 \left(\frac{T}{300} \right)^{-1.1}$
$k_{O_2}/[O_2]$	$k_{O_2}/[O_2] = 0.001 + 0.00845 \exp \left(-2 \left(\frac{(E - 12000)}{11000} \right)^2 \right)$

Figure 2.1.6 shows a comparison among these new FQY data, the updated model, and the model using parameters from the previous work with 277 nm excitation in panel a and with 308 nm excitation in panel b. The cell data and model from the current work agreed with the previous model by Koch at room temperature; however, at both high temperatures and high pressures, the Koch model significantly deviated from the new cell data. The updated model captured these variations. Improved understanding of the photophysical processes behind ketone fluorescence will enable the quantitative interpretation of PLIF diagnostics over a wider range of conditions than was previously possible.

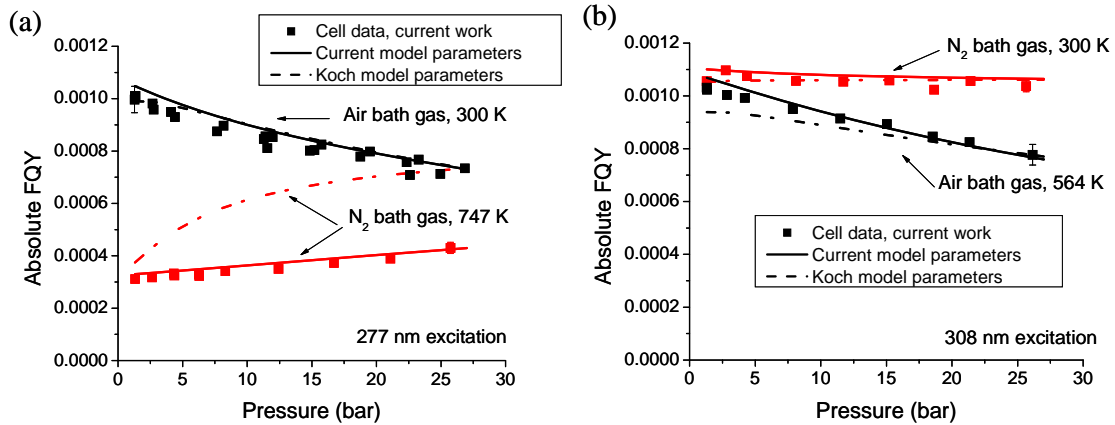


Figure 2.1.6 FQY variation with pressure at various temperatures for 277 nm excitation in panel a and 308 nm excitation in panel b.

2.2 High-Speed PLIF/LIF Using CW Excitation

2.2.1 Background

Tracer-based planar laser induced fluorescence (PLIF) imaging has been an effective diagnostic for measuring spatial variations of temperature and composition in a variety of flowfields [1]. Generally speaking, these diagnostics utilize pulsed laser systems for excitation with higher photon flux, compensating for the low fluorescence quantum yield of many of the available tracers. Utilizing a pulsed laser limits the temporal resolution of the diagnostic to the pulse rate of the laser. Many commercially available ultraviolet lasers, such as excimers, frequency-quadrupled Nd:YAGs, and pumped dye lasers, typically have repetition rates of 10-30 Hz, which is significantly slower than the time scales of mixing and combustion phenomena. Interests in high-speed flow phenomena have driven such research toward high-speed PLIF using high-repetition-rate pulsed lasers [8,9]; however, CW lasers offer an alternative laser source for high-speed imaging. Preliminary studies of this new diagnostics approach were completed recently with AFOSR support.

Previous CW excitation of laser-induced fluorescence was limited by low average laser power especially for UV excitation [10,11]; however, high-power CW lasers recently have become available commercially for visible wavelengths, and we have frequency-doubled such a laser to produce high power CW laser light in the UV. For example, we have used a high-efficiency frequency-doubling cavity to produce a CW beam of 266 nm laser light with more than 600 mW average power using only 5.5 W of 532 nm light from a commercial diode-pumped-solid-state (DPSS) laser. By exploiting the large fluorescence quantum yield of toluene as a tracer, we demonstrated the potential for high-speed imaging using CW excitation in a turbulent jet. The results are summarized below with the details found in Ref. 12.

2.2.2 Characterization of Toluene-Based CW PLIF

The diagnostic sensitivity was assessed by examining the fluctuation detection limit, defined as the minimal detectable change in LIF signal. These detection limits were determined for single-point (0-D) LIF, line imaging (1-D) LIF, and 2-D PLIF imaging.

The weak-excitation fluorescence equation describes the LIF signal:

$$S_f = \frac{P\lambda}{hc} \Delta t \frac{\chi p}{k_b T} L \sigma(\lambda, T) \phi(\lambda, p, T) \frac{\Omega}{4\pi} \eta \quad (2.2.1)$$

where P is the incident laser power, λ is the laser wavelength, Δt is the exposure time, p is the total pressure, T is the temperature, χ is the mole fraction of fluorescing tracer, L is the length of the illuminated volume, Ω is the detector collection angle, and η is the detector collection efficiency. The FQY, ϕ , and absorption cross section, σ , are measured photophysical parameters describing variation of LIF signal with temperature, pressure, and excitation wavelength. The fluctuation detection limit f was determined from the ratio of noise to the mean signal, where the noise value was defined as the root-mean-square (RMS) variation of the signal.

$$f = \frac{\sigma_f}{S_f} = \frac{1}{SNR} \quad (2.2.2)$$

For sufficient LIF signal levels, the noise characteristics of the diagnostic will be in the shot-noise limit, a fundamental limit of the LIF signal intensity noise related to the discrete nature of photons. In the shot-noise limit, the fluctuation detection limit can be predicted using

$$f = \frac{1}{\sqrt{S_f}} \propto \sqrt{\frac{B}{nVP}} \quad (2.2.3)$$

where S_f is given by equation (2.1.1), B is the frame rate or bandwidth of the detector, n is the number density of the tracer, V is the illuminated volume imaged by the detector, and P is laser power. Demonstration measurements were performed in a free jet expansion to determine the detection limits.

2.2.3 CW PLIF Experimental Setup

The visible laser was frequency-doubled into the UV, collimated and directed through a free jet of 4% toluene in nitrogen. The toluene LIF signals were lens-collected and focused onto the detector. Single-point LIF was detected with a photomultiplier tube, line imaging was detected with a time-shifted, kinetic-readout, frame-transfer CCD camera with a 512 x 1024 array, and PLIF was detected using an interline-transfer intensified CCD camera that was capable of taking 2 sequential images with a 3 μ s interframe time. The experimental setup used for 2D-PLIF is illustrated in Fig. 2.2.1.

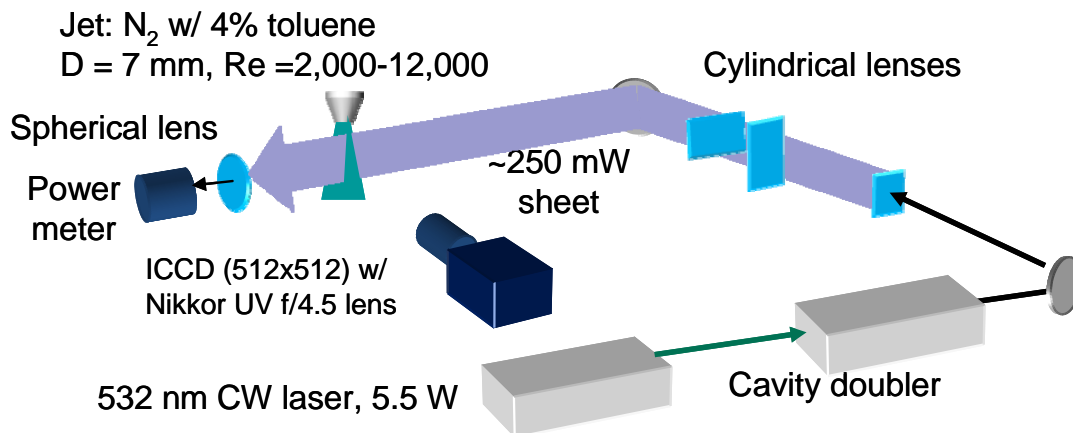


Figure 2.2.1. CW LIF of toluene excited at 266 nm CW light.

The maximum laser output power at 266 nm used for these experiments was 440 mW. The beam was 0.4 mm in diameter as it passed through the jet. For 2-D imaging, the laser beam was expanded with cylindrical lenses into a sheet that was 20 mm tall by 0.4 mm thick. The maximum power available energy in the laser sheet was ~250 mW due to clipping of the sheet. The fluorescence signal was imaged using a frame-transfer intensified CCD camera with 512 x 512 pixel array.

The measurements were performed in a free jet from a 7 mm diameter stainless steel orifice, 4% toluene was seeded into nitrogen using a saturating percolator. The Reynolds number of the flow was 1670, and the central core of this jet was assumed to be steady. In the point and line imaging cases, the laser beam was passed through the center of the jet, ~ 1 mm from the jet exit. In the 2-D imaging case, the laser sheet was passed through the center of the jet just below the jet exit. Since the LIF signal was collected from the central core of the jet, we assumed that there were no oxygen quenching effects on the toluene fluorescence signal; thus, fractional changes in the signal corresponded to fractional changes in toluene mole fraction.

Multiple LIF images were taken of the flowfield for different laser powers and exposure times. The pixels imaging the central core of the jet were used to calculate the noise. The RMS variation of the signal was calculated using the equation below:

$$\sigma = \frac{1}{N_p} \sum_{x=1}^{N_p} \sqrt{\frac{1}{N} \sum_{i=1}^N (S_{x,i} - \overline{S_x})^2}$$

where N is the number of time steps, N_p the number of pixels in the region, $S_{x,i}$ the signal at time step i and pixel x , and $\overline{S_x}$ the mean signal at pixel x over the N time steps. The fluctuation detection limit was calculated from the ratio of this value with the mean signal.

2.2.4 CW PLIF Performance

Figure 2.2.2 illustrates the variation of the fluctuation detection limit with laser power for single-point imaging with a photomultiplier tube (PMT). The bandwidth of the PMT and

associated electronics was measured to be 8.5 kHz. A fluctuation detection limit of 0.028% was achieved with a laser power of 440 mW. The variation of detection limit

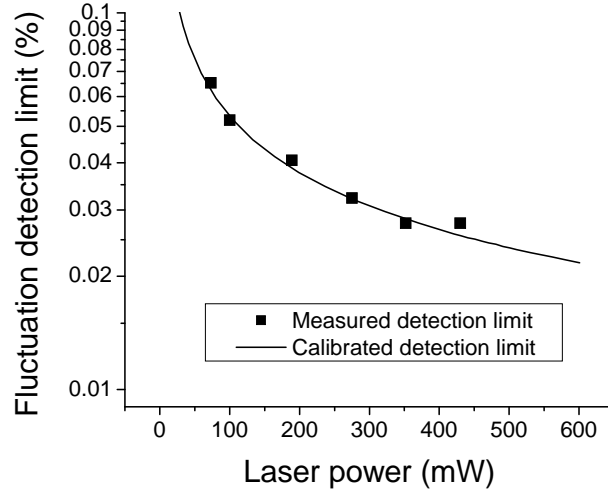


Figure 2.2.2. Variation of fluctuation detection limit with laser power for a jet seeded with 4% toluene in N_2 at 1 atm for single-point measurement of a 1 mm^3 region. The detector has a bandwidth of 8.5 kHz.

with laser power followed an inverse square root relation, confirming that the measured detection limit was shot-noise limited.

Figure 2.2.3 illustrates the fluctuation detection limits for line LIF imaging. Figure 2.2.3a shows the variation of fluctuation detection limit with laser power for four exposure times. For these results, each pixel imaged a region in the jet that was $0.04 \times 0.2 \times 0.4 \text{ mm}$ in size. A fluctuation detection limit of 2.63% was observed for a laser power of 461 mW for a $4 \mu\text{s}$ (250 kHz) exposure time; this limit decreased to 0.55% for a longer exposure of $104 \mu\text{s}$

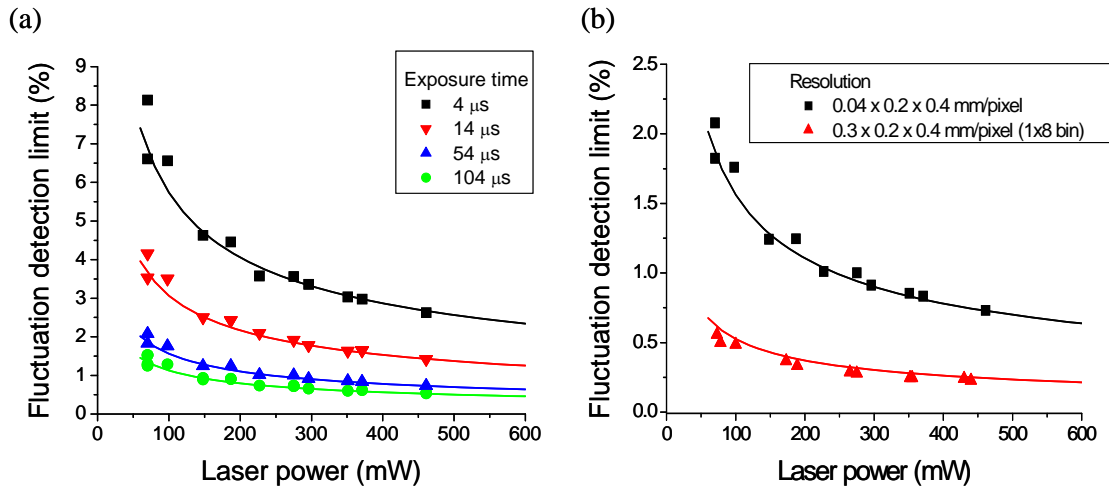


Figure 2.2.3. Line LIF imaging detection limits for each pixel as a function of laser power. Detection limits shown in (a) for 4, 14, 54 and $104 \mu\text{s}$ exposure times (250, 71.4, 18.5 and 9.6 kHz frame rates) where each pixel images a region $0.04 \times 0.2 \times 0.4 \text{ mm}$; in (b) the detection limits are shown for $54 \mu\text{s}$ exposure time for two spatial resolutions, $0.04 \times 0.2 \times 0.4 \text{ mm/pixel}$ and $0.3 \times 0.2 \times 0.4 \text{ mm/pixel}$.

exposure time (9.7 kHz). Figure 2.2.3b shows the effect of varying the spatial resolution on the fluctuation detection limit. For a laser power of 440 mW, a detection limit of 0.23% was achieved for a 54 μ s exposure time (18.5 kHz frame rate) with a 0.3 x 0.2 x 0.4 mm pixel resolution.

Figure 2.2.4 illustrates the detection limits measured for 2-D PLIF imaging. The variation of fluctuation detection limits for four different exposure times is shown in Fig. 2.2.4a. The effect of different spatial resolution on the fluctuation detection limit is shown in Fig. 2.2.4b. The fluctuation detection limit followed an inverse square root relation with laser power, consistent with the diagnostic being shot-noise limited. When each pixel imaged a region in the jet 0.05 x 0.05 x 0.4 mm in size, a detection limit of 20.3% was achieved for a 1 μ s exposure time and 271 mW. A detection limit of 2.47% was achieved for a 100 μ s exposure time and 235 mW of laser power. When the pixel resolution was changed to 0.4 x 0.4 x 0.4 mm, a detection limit of 0.88% was achieved with only 205 mW of laser power and a 100 μ s exposure time.

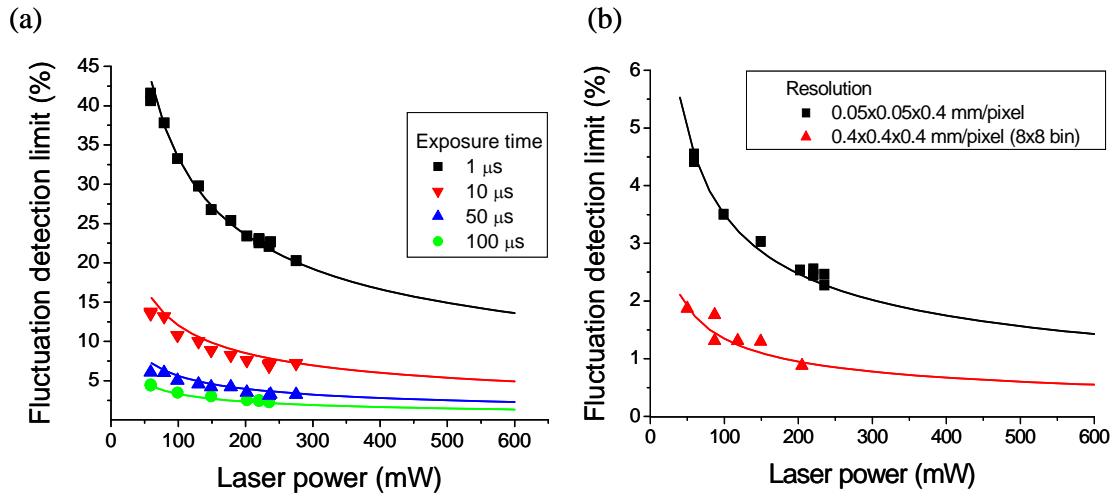
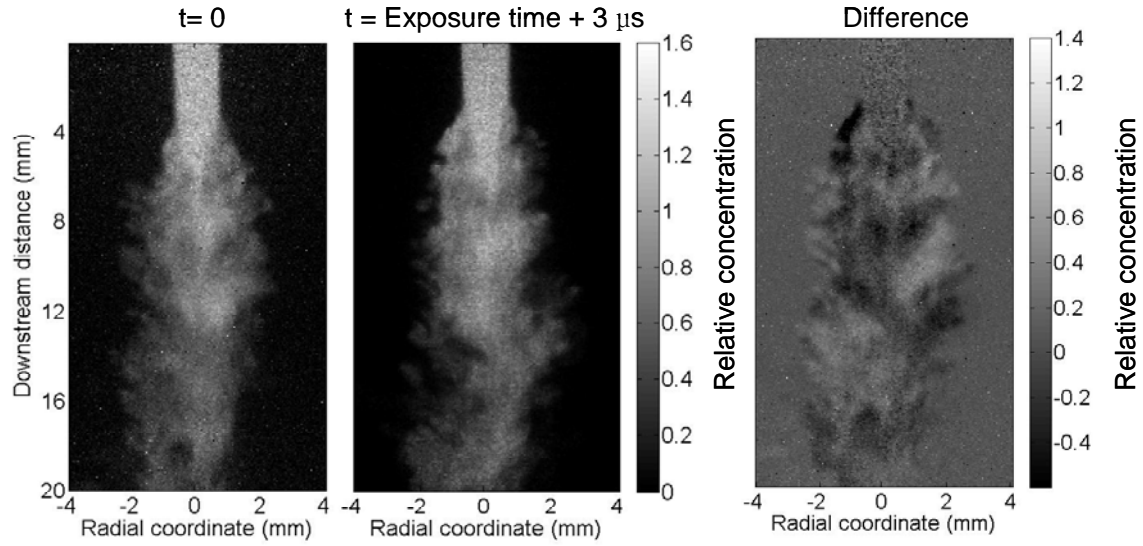


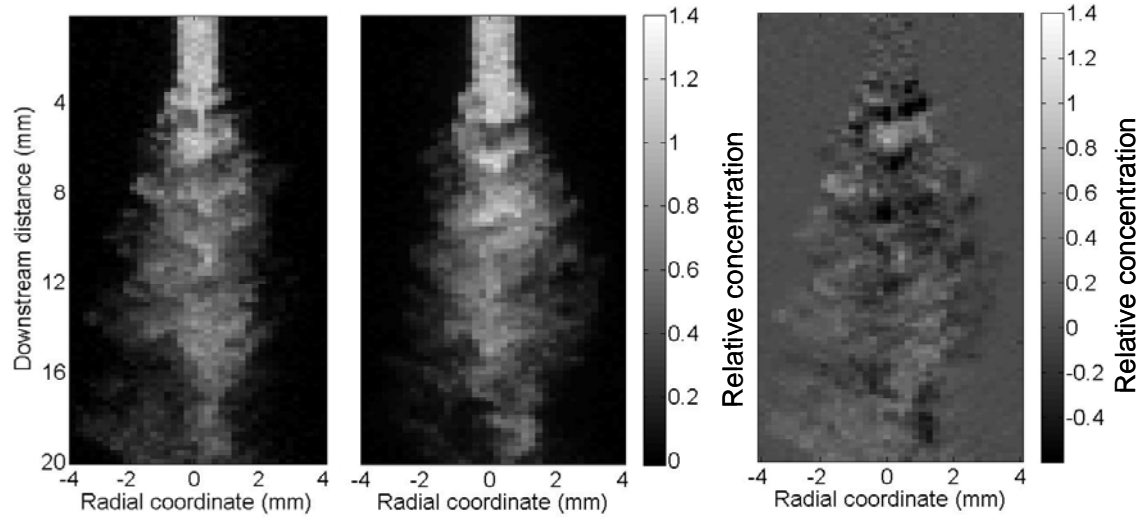
Figure 2.2.4. PLIF imaging detection limits for each pixel as a function of laser power. Detection limits shown in (a) for 1, 10, 50 and 100 μ s exposure times, where each pixel images a region 0.05 x 0.05 x 0.4 mm; in (b) the exposure time is 100 μ s and detection limits are shown for two spatial resolutions, 0.05x0.05x0.4 mm/pixel and 0.4x0.4x0.4 mm/pixel.

2.2.5 CW PLIF Application to a Turbulent Jet

A 1.7 mm diameter turbulent jet of N_2 seeded with 4% toluene ($Re=10700$) was used to test the diagnostic. To avoid reduction of the LIF signal from oxygen quenching, a N_2 coflow also was used with the turbulent jet. A 20 mm x 0.4 mm laser sheet with 203 mW of power was passed through the turbulent jet. The resulting fluorescence was imaged using an interline-transfer intensified CCD camera, which was capable of taking 2 sequential images with a 3 μ s interframe time. Figure 2.2.5 shows two pairs of sequential images and the difference between these two sequential images. One image pair was taken with a 50 μ s exposure time (18.9 kHz frame rate) and the second with a 10 μ s exposure time (76.9 kHz frame rate). These images demonstrate the potential for CW PLIF as a sensitive high-speed imaging diagnostic.



(a)



(b)

Figure 2.2.5. Time-resolved 2-D PLIF imaging of relative toluene concentration in a turbulent jet ($Re = 10700$) using PI-MAX2 camera. 203 mW of laser power was used. Two sequential images and the difference between them are shown. In (a), images are 400×150 pixels in size with $0.054 \times 0.054 \times 0.4$ mm/pixel resolution and $50 \mu s$ exposure time (18.9 kHz frame rate). In (b), images are 100×38 pixels in size with $0.2 \times 0.2 \times 0.4$ mm/pixel resolution and $10 \mu s$ exposure time (76.9 kHz frame rate).

2.3 PLIF Imaging in Shock Tube Flows

Planar laser-induced fluorescence (PLIF) imaging of temperature in a shock tube was demonstrated for both uniform and non-uniform compressible flow fields. Although there is a history of PLIF measurements of flow dynamics including supersonic flow over a bluff body, flow over a sphere [13], and temperature of shock layers using fluorescence tracers such as acetone [14], nitric oxide [15], 3-pentanone [16], and toluene [17], there have been few studies conducted in shock tube flows and none with toluene as a tracer. Initial interest in toluene as a tracer was focused on its strong fluorescence quenching in the presence of oxygen, which led to its use for fuel-air ratio and residual-gas measurements in internal combustion (IC) engines [18]. The absorption cross-section and fluorescence quantum yield have been measured in detail for a wide range of temperature and pressure conditions. The absorption cross-section for 248 nm excitation is insensitive to temperature between 300 and 850K, with a measured value of approximately $3.1 \pm 0.2 \times 10^{-19} \text{cm}^2$. The FQY of toluene following 248nm excitation is quite sensitive to temperature for this same range, and the overall temperature sensitivity of the LIF signal is larger than other ketone and aromatic tracers [19]. Vibrational relaxation of the electronic excited state plays an important role in determination of the FQY, as illustrated by the pressure-dependent FQY data in Fig. 2.3.1 for four different partial pressures of toluene in nitrogen bath gas at 296K. These data show that vibrational relaxation must be considered for total pressures below 1 bar or toluene partial pressures below 50 mbar. A fluorescence model for toluene was developed by Koban et al. with AFOSR support [19], which enables PLIF thermometry with toluene as the tracer. Using this model, temperature measurements using toluene PLIF were validated first in shock-heated gases where the temperature and pressure are well-known from the ideal shock relations. Preliminary temperature measurements then were made for supersonic flows over a wedge to generate a target data set needed for evaluation of computational fluid dynamic (CFD) models for high-speed flows.

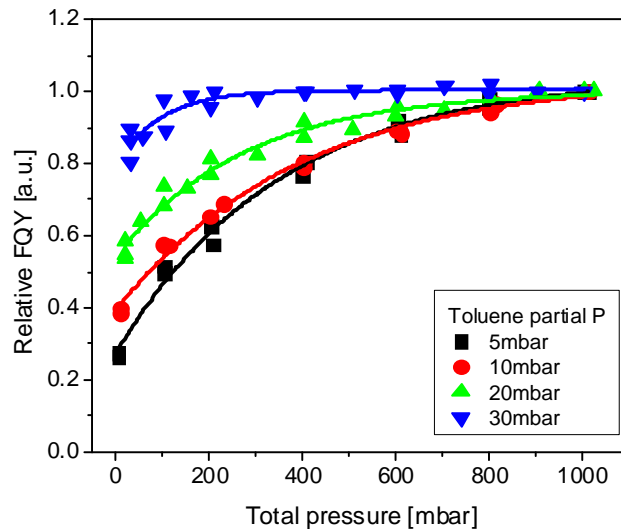


Figure 2.3.1 Relative FQY for toluene dilute in nitrogen at 296K as a function of total pressure and toluene partial pressure.

2.3.1 PLIF of Temperature in a Shock Tube

A new PLIF test section for the Stanford shock tubes was designed and built to enable optical access for PLIF imaging near the shock tube walls, which allowed measurements to characterize boundary layers near a flat wall or near the intersection of two walls. The imaging section was constructed of four flat plates. Three of the plates were fused silica windows 10x10x2.5cm thick, which allowed optical access on two sides and the top of the square flow section. The endwall also was fabricated from a 10x10x2.5 cm thick fused silica window. The endwall window provided access for the excitation laser sheet to be directed toward the approaching incident shock wave, as illustrated in the experiment schematic in Fig. 2.3.2. The fluorescence was collected normal to the excitation laser sheet through one of the side windows or the top window. The fourth side plate was made of polished aluminum to enable mounting of pressure transducers. Seals and sealing clamps were fabricated to avoid any obstruction to the optical access of any point in the flow field, including the flows in the corners where two adjacent plates join.

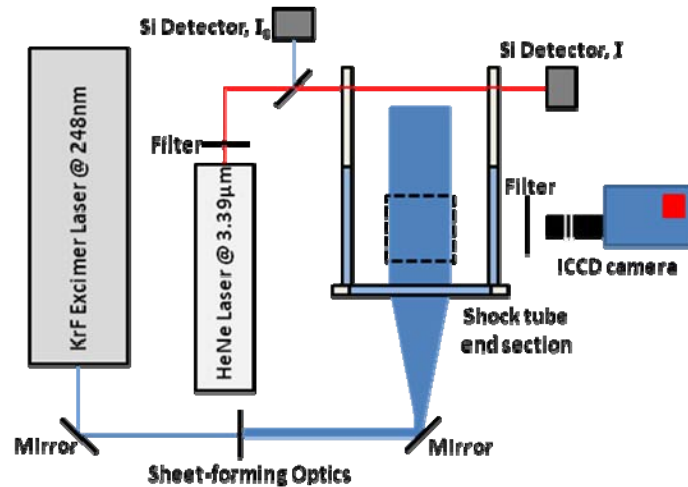


Figure 2.3.2 PLIF set up for 248 nm excitation of toluene seeded into shock-heated flows. The schematic shows the laser sheet directed through the fused silica endwall toward the oncoming incident shock wave. Absorption of 3.39 μm HeNe laser light provided a monitor of the toluene concentration.

The shock tube has a driver section 3 m long with 15 cm internal diameter, which transitions smoothly at the diaphragm to a driven section 9.6 m long and 11 cm in diameter. The flow in the driven section then transitions to a square end section (2 m long with 10 cm height/width). This square section has a 0.5" radius at the corners of the square. For this work we desired a square corner, and a transition section was fabricated to transition the corner radius to square to match smoothly with the new PLIF test section. A straight flow section of 15 cm was added to mitigate any non-ideal flow effects of this transition. A variety of diaphragm thicknesses was used to generate a wide range of post-shock conditions.

Toluene was premixed with nitrogen bath gas in a separate mixing tank (magnetically stirred to facilitate uniform mixing). The toluene seeding level was monitored by absorption of HeNe laser light at 3.39μm [20]. For PLIF imaging, the toluene was

excited at 248 nm by a KrF excimer laser (250mJ/pulse). The laser beam was formed into a sheet 5 cm wide and 0.5 mm thick and directed into the shock tube through the endwall window. Fluorescence signals were collected perpendicular to the laser sheet and imaged onto an intensified CCD camera. Images of the toluene PLIF were collected ~6cm upstream of the endwall with a camera resolution of 0.06 mm/pixel. A notch filter was placed in front of the camera to suppress Rayleigh scattering. The initial conditions of the test gas (pressure, temperature, and fuel loading) were combined with the measured shock speed in the ideal shock relations to provide known temperature and pressure behind the incident and reflected shock waves, thereby testing the toluene PLIF temperature measurements. The PLIF measurements were corrected for laser intensity variations over the laser sheet and converted to temperature fields.

Shown in Fig. 2.3.3 are two examples of PLIF images that were taken in the core flow (far from the walls). The images are oriented with the endwall at the bottom of the figure. On the left side of Fig. 2.3.3, the PLIF image captured the propagation of the incident shock wave towards the endwall. The gases near the endwall were at the initial conditions ($p_1=50$ Torr of nitrogen with 3.8% toluene mole fraction), and the region at the top showed the temperature increase (to 410K) from heating by the shock wave. On the right side of the figure, the shock wave had reflected from the endwall and was propagating towards the top of the figure. Again, the temperature rise behind the shock wave was evident. The flat uniform temperature data and the sharp rise of temperature behind the shock wave show that our assumption of a planar shock wave was quite good.

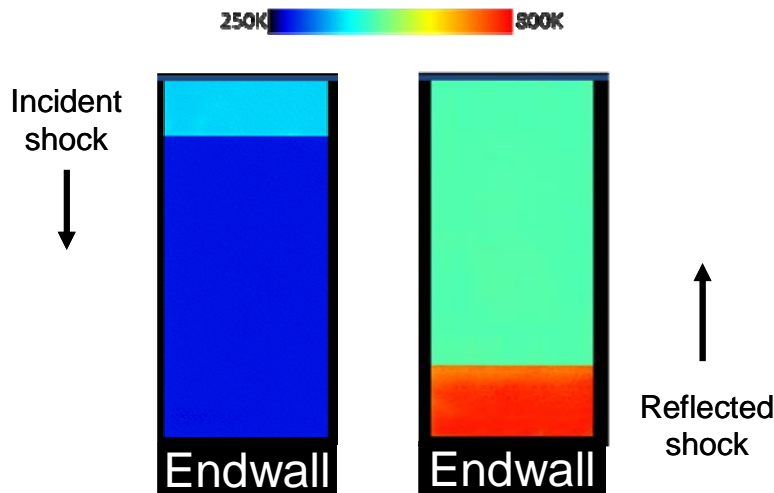


Figure 2.3.3 Left panel: PLIF temperature measurement in the shock tube capturing the propagation of the incident shock wave toward the endwall with $p_1 = 50$ Torr of nitrogen with 3.8% toluene mole fraction; right panel: PLIF temperature measurement, capturing the propagation of the shock wave reflected from the endwall.

Similar data were collected for a wide range of shock conditions, and the quantitative agreement of the PLIF temperature with the core temperature expected from the ideal shock relations is given in Fig. 2.3.4. Near room temperature the mean measurement uncertainty was $<0.4\%$; however as the temperature rose, the mean uncertainty increased to $\sim 1.6\%$ for the post-incident shock and $\sim 3.6\%$ for the post-reflected shock. These data

were in remarkable agreement considering the ~6% uncertainty in the absorption cross section and ~10% uncertainty in the model for the FQY.

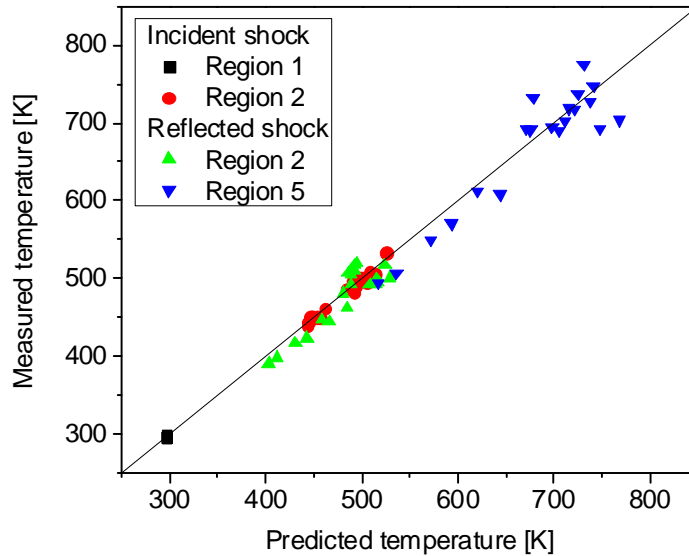


Figure 2.3.4 Comparison of the temperature inferred from the PLIF measurements with the temperature predicted by the ideal shock relations in region 1 before shock heating, region 2 behind the incident shock, and region 5 behind the reflected shock.

2.3.2 PLIF of a Supersonic Flow Temperature Over a Wedge

PLIF of toluene was used to infer the gas temperature associated with incident shock propagation over a wedge. For these experiments the laser sheet was directed across the flow through a side window. The wedge was 7.5 cm long with a 30° angle facing upstream, as illustrated in Fig. 2.3.5. The temperature measurement captures all of the expected structure in the flow of the shock wave over the wedge.

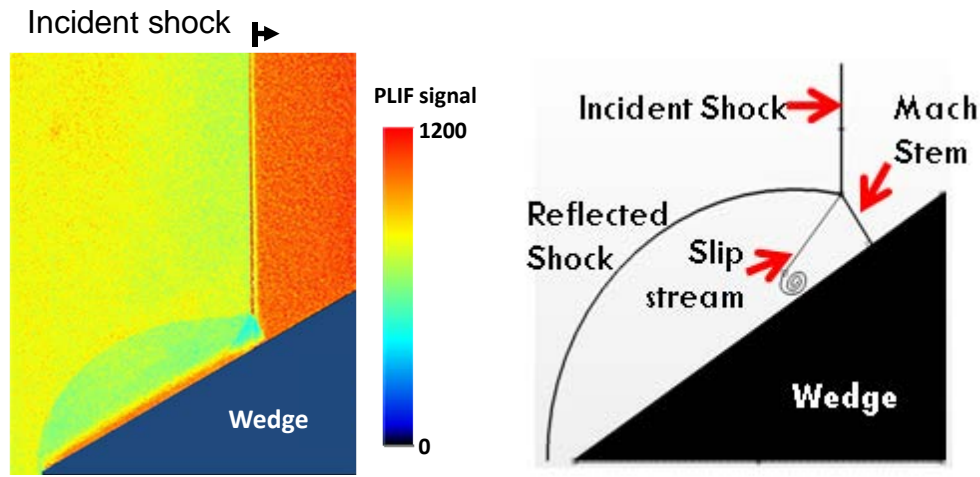


Figure 2.3.5 Left panel PLIF of toluene used to infer temperature for a shock wave propagating over a wedge; right panel shows the expected shock structure for this flow.

The flow field for shock propagation over a wedge cannot be solved analytically; however, we used a commercial CFD code (Fluent 6.0) to simulate the temperature and pressure fields for a quantitative comparison with the temperature inferred from toluene PLIF measurements. A coupled density solver was used to solve the continuity equation in the control volume. The ratio of specific heats for toluene and nitrogen was expressed as third-order polynomial fits, and viscosity was treated via the Menter shear stress transport (SST) model [21]. The simulated temperature field is shown in the left panel of Fig. 2.3.6 and this image captured the same flow structures that were observed in the PLIF temperature data (right panel).

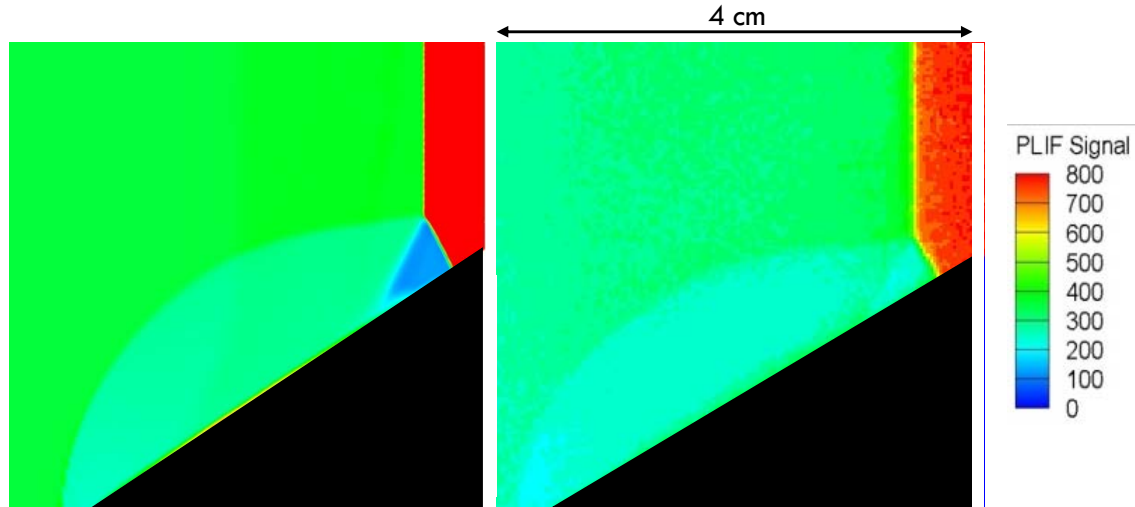


Figure 2.3.6 Left panel simulated temperature field using Fluent; right panel temperature field inferred from PLIF measurements.

The values matched extremely well except within the slipstream region. A quantitative comparison is given in Table 2.3.1. A 5% discrepancy in the PLIF signal at these pressures corresponded to only 0.5% variation in temperature. The reason for the discrepancy in the slipstream region is uncertain; however, this region is the only one where viscous terms are important, so perhaps the simulation was not capable of capturing the necessary flow physics in the slipstream. Although there might be an error associated with the experiment that remains unaddressed, the excellent agreement between model and measurement in all inviscid regions suggested potential model deficiencies associated with the viscous terms.

Table 2.3.1 Measured and simulated temperatures for selected regions in the flowfield

Regions	Actual PLIF signal level	Synthetic PLIF signal level
Bow shock at nose	260	250
Reflected shock	280	275
Free stream	375	365
Slip stream	310	135

Further work is planned to investigate flow regions near the side- and endwalls to characterize the thermal boundary layer and bifurcation of the reflected shock. Other

plans include study of the temperature field generated by shock reflection from a curved or notched endwall. Potential extensions to the technique include adding a second excitation wavelength to determine pressure and temperature simultaneously. Ultimately, the expansion of high-speed PLIF using CW excitation would be exploited to monitor the time evolution of the shock and boundary layer interaction.

2.4 Tunable Diode Laser Diagnostics with Extended NIR Devices

Recently developed room-temperature, CW, single-mode diode lasers operating at longer wavelengths, up to 2.9 μm , provide the capability to access transitions in the fundamental vibrational bands of H_2O and stronger combination vibrational bands of CO_2 . The increased absorption strength at these longer wavelengths offers greater sensitivity and potential for making measurements in systems with short optical pathlength. The first demonstrations of this new class of diode lasers for absorption measurements of CO_2 and water vapor were performed on this AFOSR-sponsored grant [22,23]. To further improve the sensitivity, noise immunity, and robust application to harsh environments a sensor strategy then was investigated using wavelength-modulation spectroscopy (WMS) with detection at twice the modulation frequency ($2f$) normalized by the signal at the modulation frequency ($1f$) [24]. This WMS- $2f/1f$ strategy achieved very high signal-to-noise ratio (SNR) absorption data which was used then for extremely precise temperature measurements behind reflected shock waves.

2.4.1. Single-Laser H_2O and Temperature Sensor near 2.5 μm

Sensor systems based on room-temperature diode lasers and high-resolution absorption spectroscopy techniques are advantageous because of their non-invasive nature, fast time-response, and *in situ* measurement capability. These sensors have proven to be highly attractive for practical combustion and propulsion applications owing to their compactness, reasonable cost, robustness, and ease of use. These tunable diode laser (TDL) sensors can provide a sensitive, fast, and reliable solution for measurements of multiple flow-field parameters such as temperature, gas species concentration, velocity, density, mass flux, and pressure. Water vapor (H_2O) is one of the primary hydrocarbon combustion products and has a strong rovibrational spectrum throughout the near-infrared (NIR) and mid-infrared (MIR), as illustrated in Fig. 2.4.1, where the absorption line strengths of H_2O are plotted versus wavelength from 1 to 3 μm at a representative combustion temperature of 1500 K. The $2\nu_1$, $2\nu_3$ and $\nu_1+\nu_3$ absorption bands in the NIR have been used for most of the previous absorption sensor research, as fiber-coupled telecommunications-grade semiconductor diode lasers are available commercially in this wavelength range. These overtone and combination vibrational bands of H_2O are approximately 20 times weaker compared to the two fundamental vibrational bands (ν_1 and ν_3) in the region 2.5-3.0 μm . While the NIR sensors can take advantage of current optical fiber technology for applications such as wavelength-multiplexing, the relatively small absorption strength of transitions in this region can limit these sensors to high concentration and/or long pathlength applications. As a first demonstration of this new

class of diode lasers near 2.5-3.0 μm , a TDL sensor based on water vapor absorption near 2.5 μm was designed and tested in a heated static cell and laboratory burner [22].

Since there are several thousands of water vapor absorption features in the wavelength range of interest, a design-rule-based line selection procedure [25] was used to optimize sensor performance by identifying lines with appropriate absorption strengths and good isolation from interference by other gases, as well as adequate immunity to the effects of cold boundary layers. The ratio of absorbance of two transitions with different lower-state-energy provides gas temperature and is termed two-line absorption thermometry. By suitable choice of laser wavelength it is possible to perform two-line absorption thermometry using a single tunable diode laser. The use of a single laser can simplify the sensor system and reduce cost compared with dual-laser techniques. Here we utilized scanned-wavelength direct absorption strategy for water vapor concentration and gas temperature sensing. Compared with a fixed-wavelength strategy, the current technique can lead to lower sensor bandwidth and more complex data analysis but offers significant mitigation of potential problems encountered in fixed-wavelength sensors, such as optical scattering, contamination by optical emission and interference absorption. Also, scanned-wavelength direct absorption does not require precise knowledge of accurate broadening parameters and precise adjustment of laser line-center.

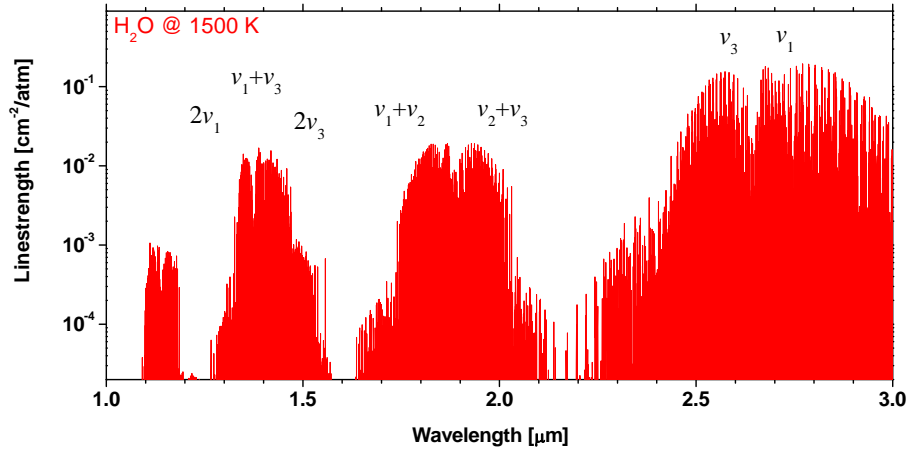


Figure 2.4.1. Absorption line strengths of H_2O at 1500K (from HITRAN [26] database).

Spectroscopic Measurements

An important step in the design of a TDL sensor is the determination of fundamental spectroscopic parameters such as line strength, line position and line-broadening parameters. Accuracy of the scanned-wavelength direct absorption strategy relies strongly on accurate knowledge of line strength as a function of temperature. Although HITRAN [26] provides a powerful tool for sensor design, the line strength values listed in the HITRAN database can have large errors, especially for transitions that only are strong at high temperatures; therefore, it is essential to perform laboratory experiments to measure and validate line strength and line shape parameters (e.g., pressure broadening coefficients). Line strength values were measured for the two selected water vapor transitions as functions of temperature in a heated static cell, and the results are shown in Fig. 2.4.2. The measurements were compared with two spectroscopic databases

(HITRAN and its high-temperature counterpart HITEMP). The transition sensitive to low temperatures (low E'') had measured line strength in good agreement with the database values, but the transition sensitive to high temperatures (high E'') had a line strength with significant deviation from the values in HITRAN. These data represented the first high temperature diode laser absorption measurements of water vapor line strength in the fundamental vibrational band and demonstrated the importance of validating database values through careful experiments.

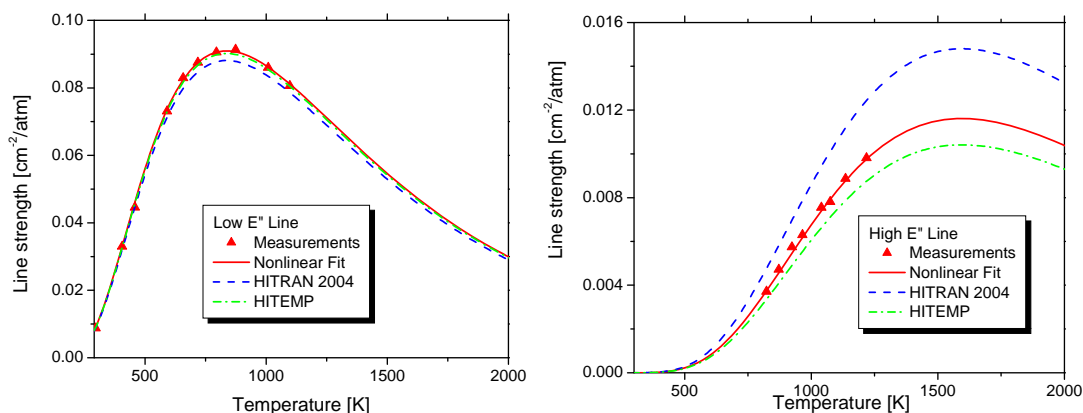


Figure 2.4.2. Calculated (HITRAN and HITEMP) and measured line strengths as a function of temperature for the low E'' H_2O line at 3982.06 cm^{-1} and high E'' H_2O line at 3982.75 cm^{-1} .

Combustion Measurements

To illustrate the potential of this sensor for combustion applications, absorption measurements of H_2O vapor and temperature were made in the burned gases above a flat-flame burner. The 25.4-cm-long burner, operated on premixed ethylene (C_2H_4) and air, provided a relatively uniform temperature distribution. Varying the fuel and/or air flow rates produced a range of equivalence ratios of $\Phi = 0.6 - 1.4$. At a specific operating point of the burner (Φ , T), the laser was tuned over the two H_2O transition by ramp-modulating laser current at a repetition rate of 1 kHz. The measured absorption spectra were fitted with a 2-line Voigt profile to determine the integrated absorbance of each transition, as illustrated in Fig. 2.4.3. The ratio of integrated areas of the two transitions is independent of species concentration and is a function of temperature only. The mole fraction of water vapor then was obtained using the measured temperature and integrated absorbance of either transition. Such measurements were carried out for several values of equivalence ratio in fuel-lean and fuel-rich flames. The measured temperatures are plotted in Fig. 2.4.4 as functions of equivalence ratio and compared with radiation-corrected thermocouple data. The excellent agreement (within 1.5%) demonstrated the ability of the TDL sensor for accurate determination of combustion temperatures. The measured H_2O concentrations are compared with chemical equilibrium calculations in Fig. 2.4.5 and were found to be in very good agreement (within 2%). The high absorbance levels obtained in these measurements reflected the advantage of using strong transitions in the $2.5\text{ }\mu\text{m}$ region, thereby offering better sensitivity and SNR than obtained with transitions at shorter wavelengths.

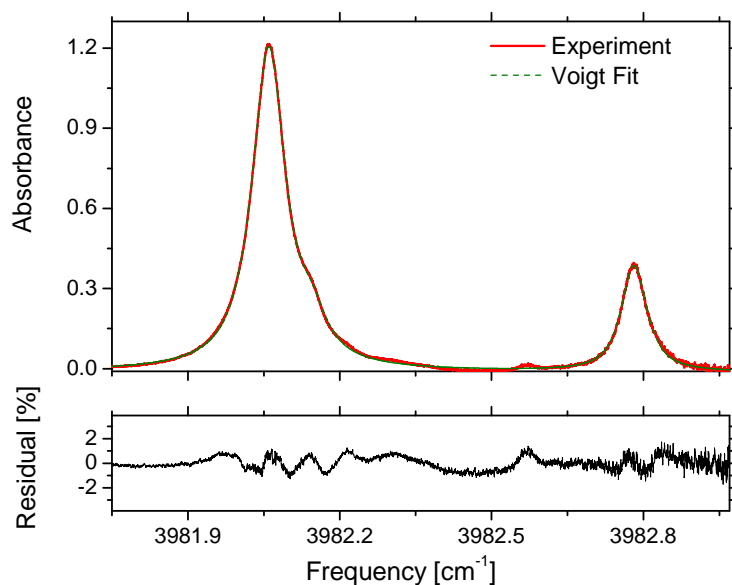


Figure 2.4.3. Single-scan absorption data taken at 1 kHz in a flat-flame burner for the two H_2O transitions near 3982.06 and 3982.75 cm^{-1} . $L = 25.4$ cm, $P = 1$ atm, $\Phi = 0.80$. Shown in the top panel is the best-fit Voigt profile to the experimental data. The residual of the fit is shown in the bottom panel.

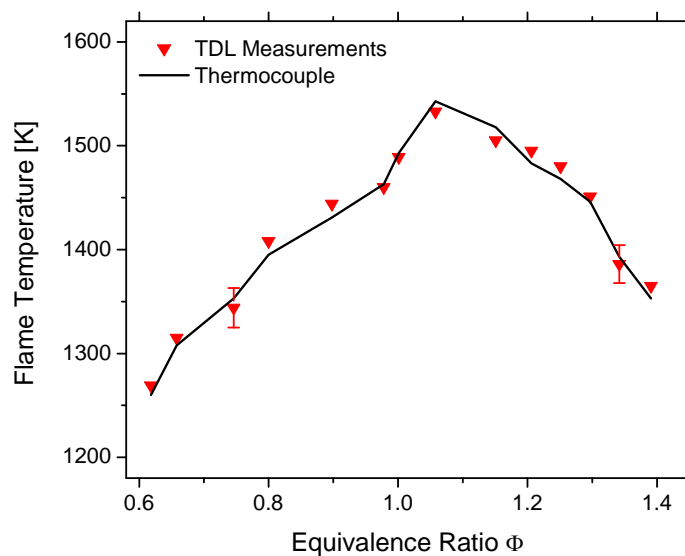


Figure 2.4.4. Measured and thermocouple flame temperature as a function of equivalence ratio in the exhaust gases above a flat-flame burner.

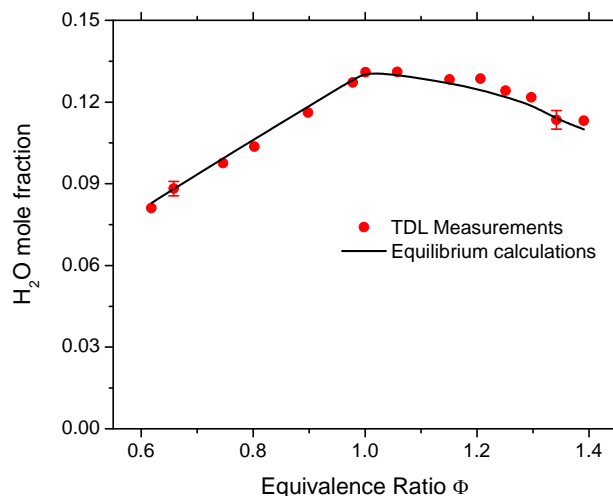


Figure 2.4.5. Comparison of measured H₂O mole fractions in the exhaust gases above a flat-flame burner with chemical equilibrium calculations.

2.4.2. CO₂ Concentration and Temperature Sensor near 2.7 μm

The information provided by TDL sensors can be quite useful in the development of modern propulsion and combustion systems with design advancements, improved efficiency, and reduced pollutant emissions. CO₂ is an attractive target gas for hydrocarbon-fueled systems as it is a primary combustion product and its concentration can be interpreted to indicate combustion efficiency. CO₂ has absorption spectra in the NIR to MIR region, as illustrated in Fig. 2.4.6, where the absorption line strengths of CO₂ are plotted as functions of wavelength from 1-3 μm at a representative combustion temperature of 1500 K. Most previous CO₂ absorption sensors were designed to exploit robust telecommunications diode lasers and optical fiber technology in the 1.3-

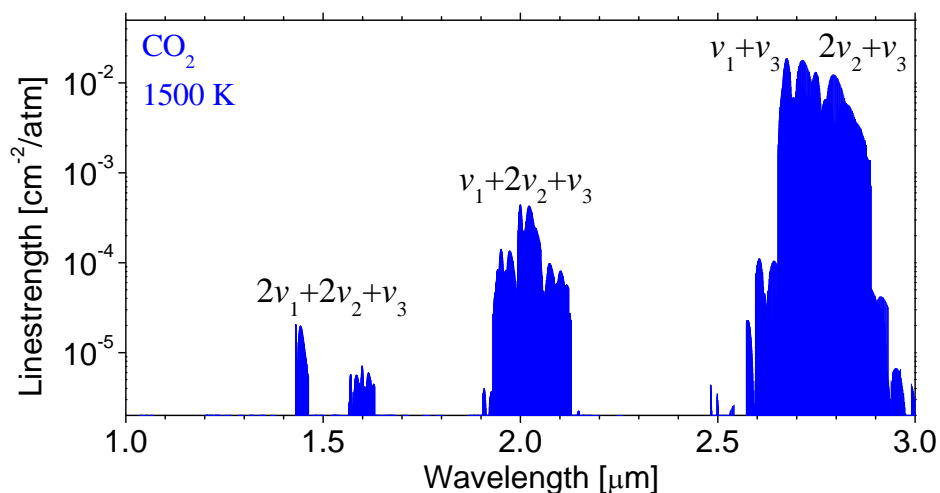


Figure 2.4.6 Absorption linestrengths of CO₂ at 1500K (from HITRAN).

1.6 μm wavelength region. Thus, previous sensors for CO_2 used the combination bands near 1.55 μm and 2.0 μm that are approximately 1000 and 50 times weaker (respectively) compared to the bands near 2.7 μm . The small absorption strengths of the transitions used previously generally have led to sensors with relatively long pathlengths and/or required significant time averaging.

Recent developments in semiconductor diode-laser technology extended the range of room-temperature single mode diode lasers to 2.9 μm , allowing access to stronger combination bands of CO_2 . Absorption sensors at these longer wavelengths offer greater sensitivity and potential for measurements in systems with short optical pathlength. For the design of a CO_2 sensor near 2.7 μm , candidate transitions were selected based on absorption strength and isolation from interference of neighboring transitions of $\text{CO}_2/\text{H}_2\text{O}$ as well as from other combustion gases, using the HITRAN database. For gas temperature sensing using the ratio of absorption, two CO_2 transitions with well-separated lower-state internal energies provided sensitivity of the absorption ratio to temperature. The selected CO_2 transitions, R(28) and P(70), belong to the $\nu_1+\nu_3$ vibrational band. The two CO_2 transitions were accessed with two different lasers, and a fixed-wavelength direct-absorption technique was used in situations where large sensor bandwidth was required, e.g. for time-resolved measurements in shock-heated gases.

For the selected lines, fundamental spectroscopic parameters (line strength, line position, self-broadening coefficient) were measured first in a heated static cell and compared with literature and database values [23]. Argon broadening parameters also were measured for these two transitions for the use of this sensor in shock tubes where the primary bath gas is often Ar.

Flat-Flame Burner Measurements

CO_2 absorption measurements were made in the burned gases above a flat-flame burner. Large sensor bandwidth was not required in these measurements, as the flame conditions remain quite uniform; therefore, the 2752 nm laser was tuned over the R(28) transition by modulating its current at 1 kHz, and the measured profile was fitted with a Voigt line shape to determine the integrated absorbance. The mole fraction of absorbing species then was obtained from Beer's law using radiation-corrected thermocouple data for temperature. Fig. 2.4.7 shows measured absorption line shape fitted with the Voigt function at the flame conditions to deduce CO_2 mole fraction from the integrated absorbance. The measured CO_2 concentrations were found to be in very good agreement with chemical equilibrium. Fig. 2.4.8 shows CO_2 measurements carried out at different fuel-air equivalence ratios compared with equilibrium values at the measured temperature. The high absorbance levels obtained in these measurements reflected the advantage of using strong transitions near 2.7 μm region, thereby offering better sensitivity and signal-to-noise ratio than obtained with transitions at shorter wavelengths.

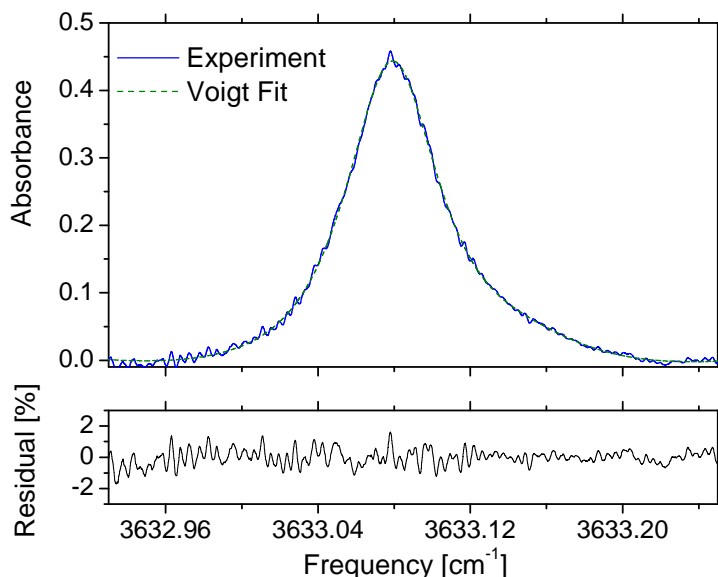


Figure 2.4.7 Single-scan absorption data taken at 1 KHz for concentration measurement in a flat-flame burner with CO₂ transition near 3633.08 cm⁻¹ at T = 1495 K, P = 1 atm, L = 25.4 cm, equivalence ratio $\phi = 0.98$. Shown in top panel is the best-fit Voigt profile to the experimental data while the residual of the fit is shown in bottom panel.

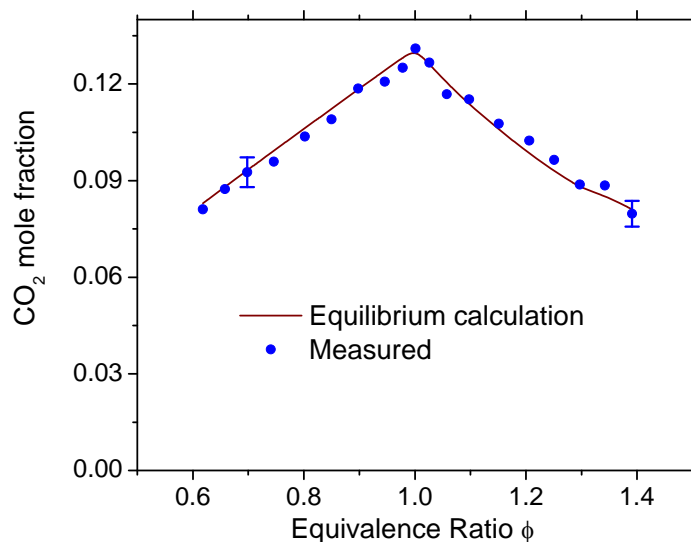


Figure 2.4.8. Comparison of measured CO₂ mole fractions in the exhaust gases above a flat-flame burner with chemical equilibrium calculations.

Shock Tube Measurements

To illustrate the potential of this sensor for monitoring CO₂ concentration and temperature in studies of the combustion mechanisms of hydrocarbon fuels, tests were conducted in shock-heated CO₂-Ar mixtures to validate the sensor accuracy and response at combustion temperatures. Experiments were performed behind reflected shock waves in a helium-pressure-driven stainless-steel shock tube. The driven section was 8.54 m long and the driver section 3.35 m long. Both sections have an inner diameter of 14.13

cm. The shock tube driven and driver sections were separated by a polycarbonate diaphragm. The diaphragm was ruptured as the driver section was filled with helium. Incident shock velocities were measured over four intervals using five piezoelectric pressure transducers and four counters, allowing accurate determination of the velocity at the shock tube endwall. Reflected shock temperature was calculated from these measured velocities and one-dimensional shock wave relations, assuming vibrational equilibrium and frozen chemistry.

TDL measurements were made at a location 2 cm from the endwall. Since the typical test times of interest in the shock tube experiments were on the order of $10\ \mu\text{s}$ - 2 ms, fast time-response was needed for measurements of CO_2 concentration and temperature, and the fixed-wavelength direct absorption approach was used. Prior to each experiment, the shock tube was evacuated by a turbomolecular pump. Baseline intensity I_0 was recorded for each laser, and then the shock tube was filled with CO_2 -Ar mixture. The data acquisition system was triggered by the pressure transducer to record pressure and transmission signals (I_t) for both CO_2 lasers during the shock heating to infer the time history of gas temperature and CO_2 concentration. Fig. 2.4.9 plots the measured time history of pressure and temperature during a shock with initial 5% CO_2 /Ar mixture. The average measured temperature over the time interval 0-1 ms (where T and P are expected to be almost constant) was 1274 K with a standard deviation of 13 K (1%). This value was in excellent agreement with the value calculated from the ideal shock equations, $T_5 = 1285\ \text{K}$. The CO_2 mole fraction can be computed using the measured pressure, temperature, and transmission signal of either laser. The measured mole fraction was multiplied with the pressure trace, and the resulting partial pressure of CO_2 is shown in Fig. 2.4.10.

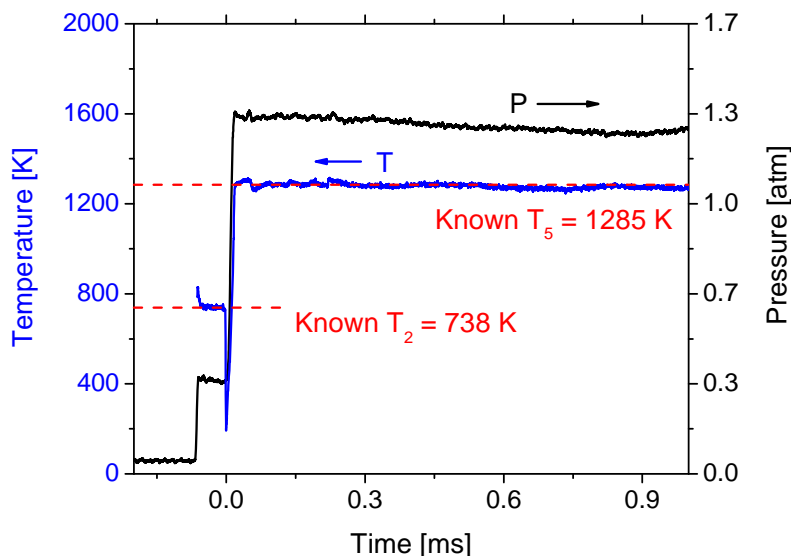


Figure 2.4.9 Measured temperature and pressure trace during a shock with 5% CO_2 -Ar mixture. Initial conditions: $P_1 = 39.8\ \text{Torr}$ and $T_1 = 297\ \text{K}$.

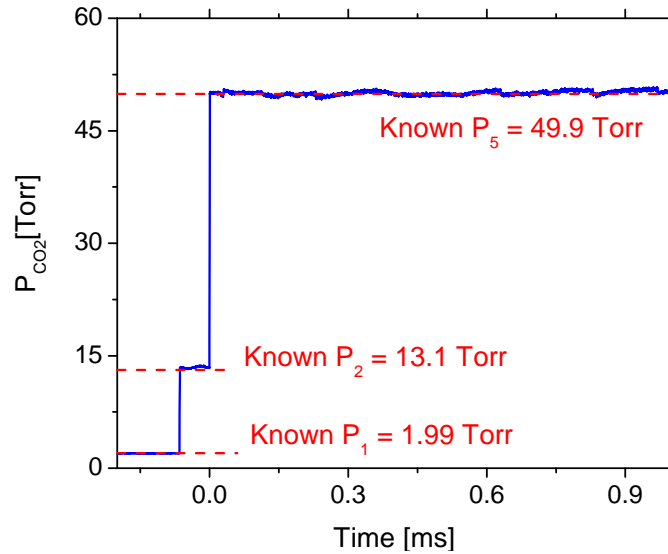


Figure 2.4.10 Measured CO₂ partial pressure from the same experiment as Fig. 2.4.9.

2.4.3 T Measurements Behind Reflected Shock Waves Using WMS

The design and optimization of combustion systems relies heavily on accurate predictive modeling. These combustion models provide information regarding performance such as efficiency and pollutant emissions. An important component of any combustion model is the reaction mechanism that describes the chemistry of the combustion event. The constitution of a reaction mechanism requires a database of accurate chemical reaction rate constants for the temperature range of interest. The test of the performance of such a mechanism requires careful experiments to determine ignition times and species concentration time-histories in reacting or combusting flow with well-controlled temperature, pressure, and reaction time. Shock tubes can provide well-defined initial temperatures and pressures for such kinetic investigations. While ignition-delay times provide an overall measure of the performance of kinetic mechanisms, refinement and validation of the detailed chemistry of the system requires a time-dependent picture of temperature and the species concentrations. Laser absorption diagnostics can provide these data for shock tube experiments. An improved tunable diode laser sensor was developed with support from this AFOSR grant for non-intrusive measurements of gas temperature and CO₂ concentration behind reflected shock waves [24].

Most previous TDL sensors were based on direct absorption techniques due to the relatively simple interpretation of measurement results. The tuning rates of many TDLs limited much of the reported scanned-wavelength direct absorption sensor bandwidths to several kHz. Fixed-wavelength direct absorption sensors are limited only by the detector bandwidth, but this strategy can be prone to errors for low-absorption applications because of various noise sources, such as beam steering, window fouling, and radiative emission. WMS-2f is a well-known technique for improving the SNR for small amounts of absorption [27]. Second-harmonic line shapes reduce the sensitivity to baseline-fitting errors encountered in direct absorption, since they are sensitive to line shape curvature, making them advantageous in dealing with noisy signals and weak absorption levels. Thus, for combustion environments with uniform properties along the measurement line-

of-sight like shock tubes, WMS-2f can be an effective method of yielding temperature measurements with higher accuracy and bandwidth than direct absorption measurements. Fortunately, for injection-current-tuned TDLs the wavelength modulation is accompanied with simultaneous intensity modulation. This intensity modulation can be exploited to normalize the 2f signal by the 1f signal to account for laser transmission variations due to beam steering, emission, window fouling, and scattering [28,29]. Our earlier work with extended NIR lasers was advanced by incorporating a 1f-normalized WMS-2f strategy and improved hardware to achieve higher SNR and accuracy of temperature measurements behind reflected shock waves. These experiments also reported the first application of our WMS-2f/1f strategy using the new class of diode lasers near 2.7 μm .

Sensor Validation in Non-Reactive Shock Tube Experiments

The WMS-2f/1f CO₂ sensor was tested in non-reactive CO₂-Ar mixtures behind reflected shock waves. Experiments were performed in the reflected-shock region of the high-purity, stainless-steel shock tube used in the preceding work. Under normal shock tube conditions, the driver section was 3.35 m long, and helium was used for the driver gas. This geometric configuration provided 2-3 ms of high-quality test time of uniform temperature and pressure. This test time was limited by either the arrival of rarefaction waves from the driver section or reflected shock-contact surface interactions near the test section. Recently, the test time of the shock tube has been extended to ~ 30 ms for measurements at lower temperatures by making two modifications: (1) the driver section was lengthened to a total of 6.4 m to allow more time before the arrival of the rarefaction fan in the test section, and (2) tailored driver gas mixtures of 30 to 40% N₂ in He were used to minimize shock wave-contact surface interactions. In some experiments, we have utilized a new strategy of inserting a properly designed cone-shaped obstacle into the driver section of the shock tube as a means of generating more constant reflected-shock temperature and pressure [30].

TDL measurements were made at a location 2 cm from the endwall, and the experimental setup in Fig. 2.4.11 shows the cross-section of the shock-tube and optical/electronics arrangement. The light from each laser was collimated and transmitted through optical windows on the shock tube side wall. The optical arrangement was based on the assumption that the gas properties across the shock tube were uniform, as expected for heating by a planar shock. The two diode lasers were modulated by 100 kHz digital waveforms, and the modulation depths were adjusted close to the optimum values. The time-histories of gas temperature and CO₂ concentration were inferred by comparing the background-subtracted 1f-normalized WMS-2f signals with simulated values. Fig. 2.4.12 plots the measured temperature time history and corresponding pressure behind a shock with 2% CO₂ in Ar at reflected shock conditions of $T_5 = 952 \text{ K}$ and $P_5 = 1.197 \text{ atm}$ using a tailored driver gas of 40% N₂ in He. The average measured temperature over the time interval 0 – 8 ms was 955 K, which was in excellent agreement with the value calculated from the ideal shock equations, $T_5 = 952 \text{ K}$. The relatively large CO₂ absorption strength near 2.7 μm and the use of the WMS-2f/1f strategy provided higher accuracy, better sensitivity, and improved SNR (over that achieved previously) as demonstrated in the difference plot (Fig. 2.4.13) of measured T and calculated T_5 . The standard deviation of ~3 K at the measured temperature of 952 K translated to an uncertainty of only 0.32%.

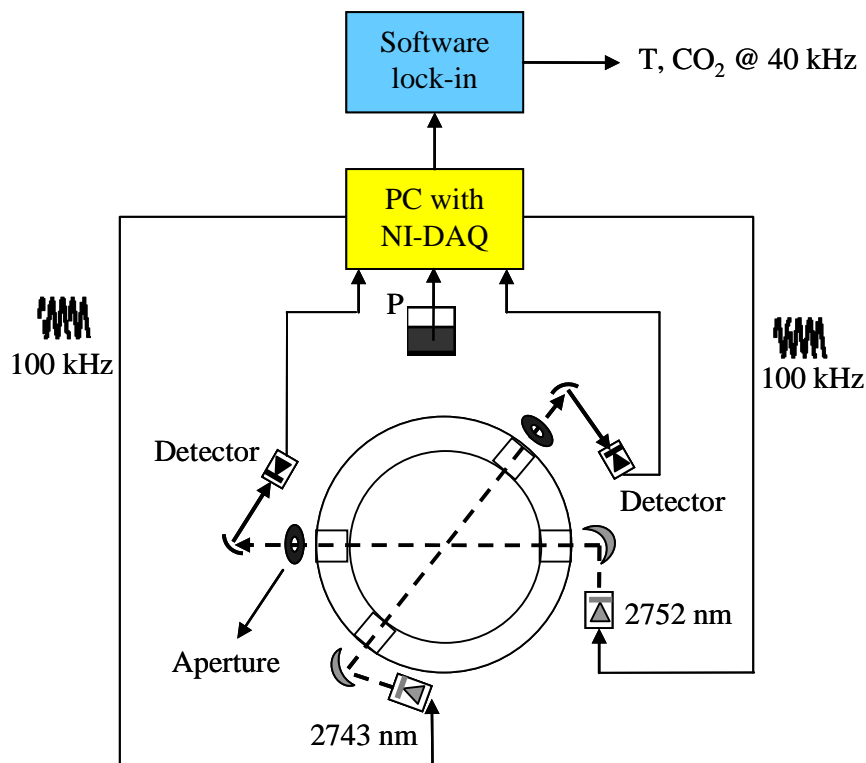


Figure 2.4.11 Schematic diagram of the experimental setup used for WMS-2f sensor measurements in the shock tube.

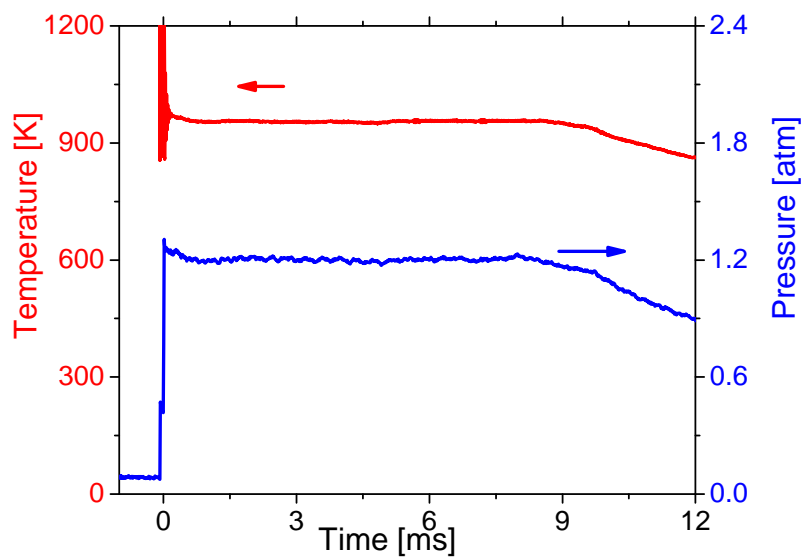


Figure 2.4.12 Measured temperature and pressure behind a reflected shock wave arriving at $t = 0$. Reflected shock conditions 952 K, 1.20 atm, 2% CO₂ in Ar, tailored driver 40% N₂ in He with driver insert.

The CO₂ mole fraction was computed using the measured pressure, temperature, and transmission signal of either laser. The measured mole fraction also was in excellent agreement with the known mixture value of 2%.

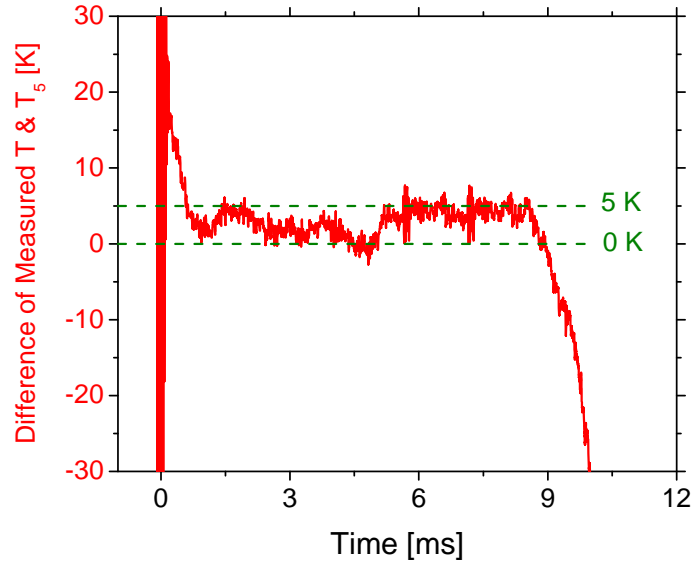


Figure 2.4.13. Difference in measured T and calculated T_5 (reflected shock temperature) for the same shock as in Fig. 2.4.12.

In shock tube experiments with very little energy release, it generally is assumed that the post-shock temperature follows the pressure isentropically. This assumption has been verified by temperature measurements using WMS-2f/1f in CO_2/Ar shocks. A typical case is shown in Fig. 2.4.14, where the measured temperature profile is plotted along with temperature calculated using isentropic compression:

$$\left(\frac{T_{\text{calculated}}}{T_5} \right) = \left(\frac{P_{\text{measured}}}{P_5} \right)^{\frac{\gamma-1}{\gamma}}, \quad \gamma_{\text{Ar}+\text{CO}_2} = 1.654$$

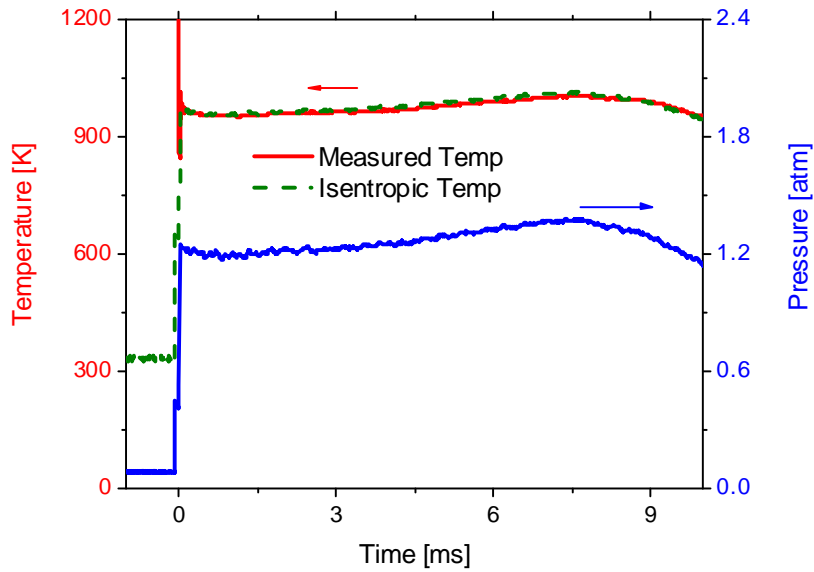


Figure 2.4.14 Comparison of the measured temperature with isentropic temperature for a shock arriving at $t = 0$. Reflected shock conditions 958 K, 1.20 atm, 2% CO_2 in Ar, tailored driver 40% N_2 in He.

Sensor Application in Reactive Shock Tube Experiments

The WMS-2f CO₂ sensor was used to measure temperature and CO₂ time-histories in the combustion of a heptane-O₂ mixture. The optical setup was similar to that shown in Fig. 2.4.11. The measured temperature and CO₂ mole fraction are plotted in Fig. 2.4.15 for a shock with 0.25% heptane and 2.75% O₂ in Ar (equivalence ratio $\phi = 1$) at the initial mixture and reflected shock conditions of $P_5 = 1.8$ atm and $T_5 = 1361$ K. The measured temperature profile was obtained after CO₂ began to form at the ignition event (~ 0.7 ms). The measurement results were compared with simulations performed using the JetSurf kinetic mechanism [31] in conjunction with a simple reactive gas dynamics model (CHEMSHOCK [32]).

For the case shown in Fig. 2.4.15, the temperature measurement was made after the ignition takes place when CO₂ was formed first as a combustion product. To obtain the pre-ignition temperature profile, CO₂ was seeded in the initial mixture as CO₂ where it is relatively inert and does not perturb the chemistry. An example is shown in Fig. 2.4.16 where 1% CO₂ was seeded into a stoichiometric mixture of 0.25% heptane in O₂/Ar, and temperature was measured for the entire test sequence. This temperature information can be quite helpful in understanding pre-ignition chemistry and gas dynamic effects. Measurements of the CO₂ profile and temperature can be made for a variety of fuels and hydrocarbons, and we expect that such data greatly will aid validation of existing kinetic mechanisms and will be useful for developing more accurate combustion mechanisms.

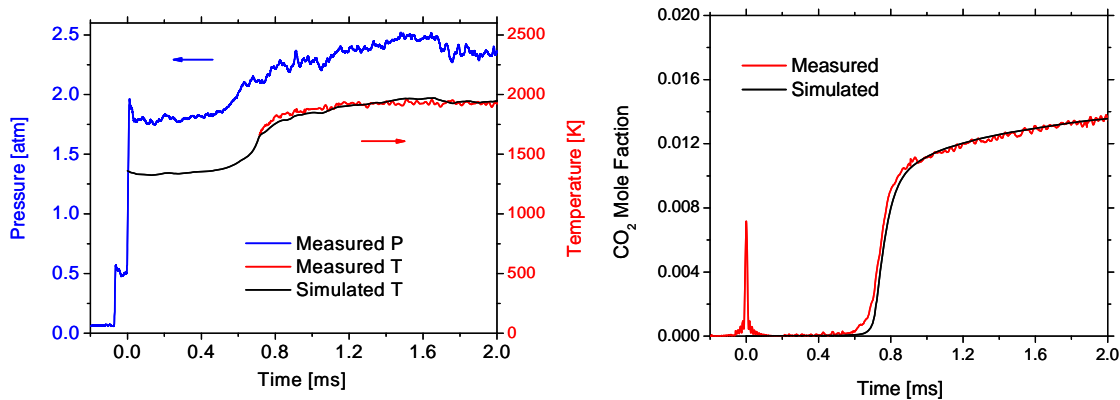


Figure 2.4.15. Left panel: Measured temperature and pressure behind the reflected shock wave. Mixture: 0.25% heptane, 2.75% O₂, balance Ar. Reflected shock initial conditions: $T_5 = 1361$ K, $P_5 = 1.8$ atm. Right Panel: Measured CO₂ mole fraction for the same shock. Simulations are based on the JetSurf kinetic mechanism.

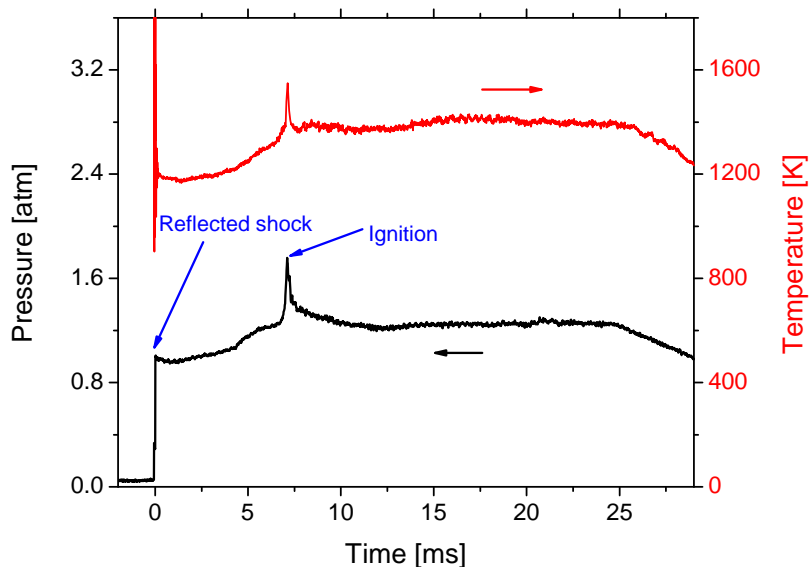


Figure 2.4.16 Measured temperature and pressure behind reflected shock wave. Mixture: 0.25% heptane, 2.75% O₂, 1% CO₂, balance Ar. Reflected shock initial conditions 1172 K, 0.98 atm, tailored driver gas with 40% N₂ in He.

2.5 Extended NIR TDL Absorption at High Pressures

Future engine concepts for efficient and clean combustion incorporate ultra-dilute mixtures at pressures considerably higher than are employed in current internal combustion engine technologies. New diagnostic methods are needed to make measurements of various combustion species at these high pressures. On this AFOSR grant, our work with extended NIR lasers (reported in section 2.4) was extended to investigate the feasibility of diagnostics for high-pressure environments [33,34].

2.5.1. CO₂ Concentration and T at High Pressure Using WMS-2f/1f

The next generation of clean, fuel-flexible and efficient engines will operate at pressures considerably higher than those commonly used today. At these pressures many of the fundamental assumptions underlying present combustion modeling become invalid. Basic research is needed to characterize the physical properties and chemical oxidation mechanisms of current and future transportation fuels at high pressures in order to understand reaction initiation and propagation under these conditions. A thorough fundamental understanding of the chemistry and physics of new fuels in high-pressure regimes will require new developments in experimental, theoretical and numerical techniques. The ability to predict fuel/species properties, reaction rates, and ignition behavior is crucial for developing clean and efficient combustion engines. New diagnostic methods hence are required for quantitative and time-resolved measurements of reactants, intermediate species, products, and temperature during the combustion of novel fuels at elevated pressures.

Extending sensor capability to high-pressure environments is complicated by the broadening and overlap of discrete spectral features at high gas density. Sensors operating under such conditions rely on comparisons between measurements and simulations to infer gas properties. A spectral database in conjunction with a line shape model was used to simulate the spectra at the experimental conditions. A number of line shape profiles including Voigt, Galatry, Dicke, Nelkin-Chatak, etc. have been used previously to model absorption spectra. These models ignore line mixing and finite duration of collision effects. These effects become quite important at high gas densities and thus the present line shape models cannot do a satisfactory job at elevated pressures. The WMS- $2f/1f$ strategy was shown to be less sensitive to the non-ideal effects seen at high pressures; however, the application of the WMS- $2f/1f$ method was limited by the available modulation range of commercial diode lasers.

Sensor Design for High Pressures

The first step in the design of a sensor is the selection of optimal absorption transitions. Since the WMS- $2f$ signal is sensitive to the curvature of the line shape and approximates the 2^{nd} derivative of the transition, it is desired to select lines that have sufficient curvature at high pressures. The feasibility of using the extended NIR transitions employed earlier for near-atmospheric pressure work was evaluated. The CO_2 transition near 3633.08 cm^{-1} was retained for the high-pressure work, but the transition near 3645.56 cm^{-1} was replaced with the one at 3645.20 cm^{-1} to achieve larger $2f$ signals at high pressures.

The magnitude of the WMS- $2f$ signal varies directly with the modulation depth. The strategy for finding the optimal modulation depth was to simulate the $1f$ -normalized WMS- $2f$ signal at the target conditions as a function of modulation depth. The maximum possible modulation depth was measured for the two lasers as a function of the modulation frequency. As expected for tunable distributed-feedback (DFB) lasers, the modulation depth (or scanning range) decreases with increasing modulation frequency. Although the WMS- $2f$ simulations suggested use of large modulation depths for high-pressure measurements, these modulation depths were not possible at the high modulation frequency required for measurements with rapid time resolution; therefore, smaller than optimal modulation depths were used, resulting in a reduction of the WMS- $2f$ signal strength.

The shape of the WMS- $2f$ line not only depends on the spectroscopic parameters (at the particular T and P) but also varies with laser parameters such as i_0 (linear amplitude of the intensity modulation). The WMS- $2f$ line shape was studied for different laser settings and modulation parameters for these new extended NIR lasers and compared with the previously used telecommunications lasers. The differences indicate that it is quite important to characterize the laser modulation parameters for each specific laser and that the resulting line shape can be different for different laser architectures.

Accurate measurements of fundamental spectroscopic parameters, including line strength, line broadening, and pressure shift, are essential for sensor development. For the WMS- $2f/1f$ sensor, measurements were compared with simulated values to infer gas properties (temperature, mole fraction), and accurate simulations relied on an accurate spectroscopic database. Pressure shift and collisional broadening of absorption lines are directly

proportional to the pressure of the gas and become even more important for sensors working at high pressures. For the transitions used in this work, all relevant spectroscopic parameters were measured in carefully performed laboratory experiments [33].

High-Pressure Measurements in a Static Cell

Scanned-wavelength direct absorption measurements were carried out at room temperature over a series of pressures (1 atm to 10 atm). Some representative data are shown in Fig. 2.5.1 for the 2743 nm laser. The measurements were compared with a Voigt profile, which is a convolution of the Lorentzian and Doppler components. The Voigt profile was chosen over the Lorentzian profile for accuracy at lower pressures; however, even at 1 atm the Voigt profile is dominated by the Lorentzian component. At 1 atm there was negligible difference between the simulation and the measurement; however, as pressure increased the simulation over-predicted the measured data. This non-ideal behavior at high densities, termed as non-Lorentzian behavior, resulted because of the breakdown of the impact approximation and the absence of line-mixing effects in the Voigt profile.

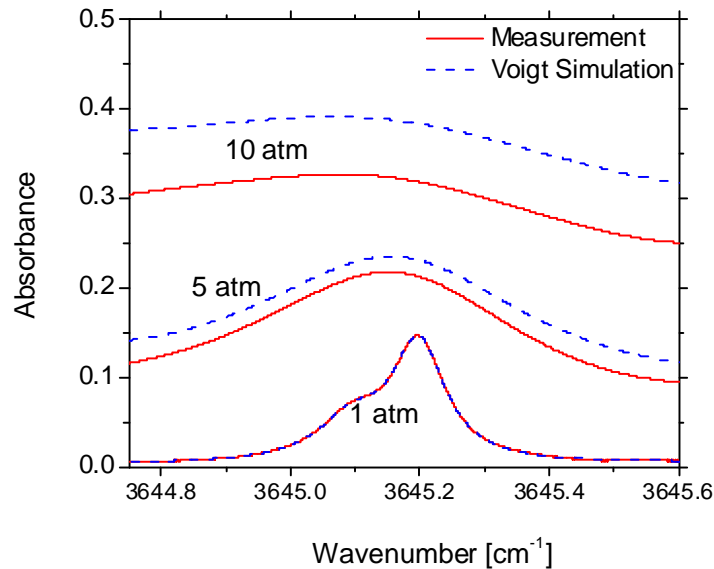


Figure 2.5.1. Direct absorption measurements for the CO₂ transition near 3645.20 cm⁻¹. T = 296 K, L = 100 cm, 0.49% CO₂ in Ar.

For WMS measurements, the two diode lasers were modulated with 100 kHz sinusoidal waveforms. The sampled signal from the detector was passed to a custom computer lock-in program that calculated values of $2f$ and $1f$ signals. Measured WMS- $2f/1f$ spectra are plotted in Fig. 2.5.2 for the two CO₂ transitions and compared with Voigt simulations at 5 and 10 atm. The measured and simulated values were in excellent agreement over the measured pressure range (1 – 10 atm). These measurements indicated that the peak WMS- $2f/1f$ measurements for both CO₂ transitions were not influenced by the non-Lorentzian effects, in contrast with direct absorption measurements where significant non-Lorentzian behavior was observed. These measurements also validated the accuracy of this new WMS- $2f/1f$ sensor for the measurements of CO₂ concentration and temperature at high pressures.

For a fixed modulation depth, an increase in the gas pressure leads to smaller $2f$ signals as the line gets broader and the curvature decreases. This result means that, although the WMS strategy alleviated the influence of non-Lorentzian line shape contributions to the absorption signal, WMS cannot be used at even higher gas densities where lower $2f$ signals result in unacceptably low values of the SNR.

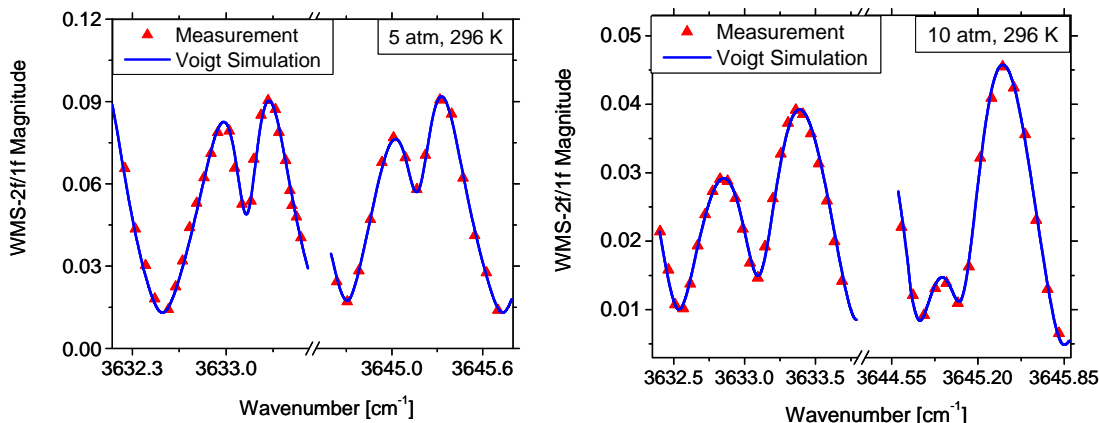


Figure 2.5.2. If -normalized WMS- $2f$ magnitude for the two CO_2 transitions. $f = 100$ kHz, $T = 296$ K, 2% CO_2 in Ar. 3633.08 cm^{-1} transition: $L = 6$ cm, $a = 0.201\text{ cm}^{-1}$; 3645.20 cm^{-1} transition: $L = 100$ cm, $a = 0.115\text{ cm}^{-1}$.

High-Pressure Measurements in a Shock Tube

Shock tubes can provide well-defined temperatures and pressures for kinetics investigations that cover broad regimes of engineering and scientific interest. Experiments were performed in the reflected-shock region of a high-purity, stainless steel shock tube. The light from each laser was collimated and transmitted through optical windows on the shock tube side wall. Measurements were carried out at 2 cm from the endwall. The time-histories of gas temperature and CO_2 concentration were inferred by comparing the background-subtracted If -normalized WMS- $2f$ signals with simulated values at the modulated wavelengths of the lasers. A sample measurement is shown in Fig. 2.5.3, which plots the time history of the gas temperature measured by the WMS- $2f/If$ sensor and the transducer-measured pressure trace. Time zero in the figure denotes the passage of the reflected shock wave. The low-pressure test gas was heated and compressed by the incident shock wave and then by the reflected shock wave. The average measured temperature over the time interval 0-1 ms was $820.4\text{ K} \pm 8.6\text{ K}$, which was in excellent agreement with the value calculated from the ideal shock equations ($T_5 = 826\text{ K}$). Similar tests performed at different temperatures and pressure range of $P_5 \sim 8 - 12$ atm achieved good accuracy and precision. These results validated the sensor accuracy for temperature and CO_2 concentration measurements at high pressures and high temperatures.

Kinetics measurements performed behind reflected shock waves have near-instantaneous heating times, spatially uniform mixtures, and occur in near-stationary (stagnant) flows. When combined with the use of non-intrusive, species-specific, quantitative laser diagnostics, shock tubes have become a primary tool for chemical kinetics measurements, providing ignition delay times, species time-histories, and elementary reaction rate

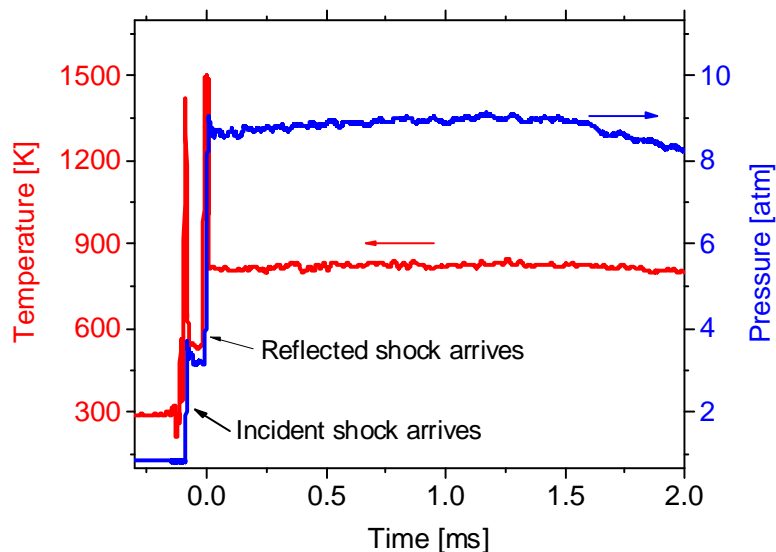


Figure 2.5.3. Measured temperature and pressure trace for a shock arriving at $t = 0$, reflected shock conditions: $T_5 = 826$ K, $P_5 = 8.7$ atm, 2% CO_2 -Ar, $L = 14.13$ cm.

determinations. There is a strong interest in the combustion community to extend the shock tube measurements to lower temperatures to study the the NTC (negative temperature coefficient) ignition regime or cool flame conditions [35]. Such measurements require longer test times and optical diagnostics validated at higher pressures. The high-pressure WMS-2f/1f sensor was demonstrated by measuring CO_2 time-histories in combustion experiments with an n-heptane/ O_2 /Ar mixture. An example measurement is shown in Fig. 2.5.4 for a shock with 0.2% heptane, equivalence ratio of 1.0, and reflected shock conditions of $T_5 = 1212$ K, $P_5 = 9.05$ atm. A tailored driver gas

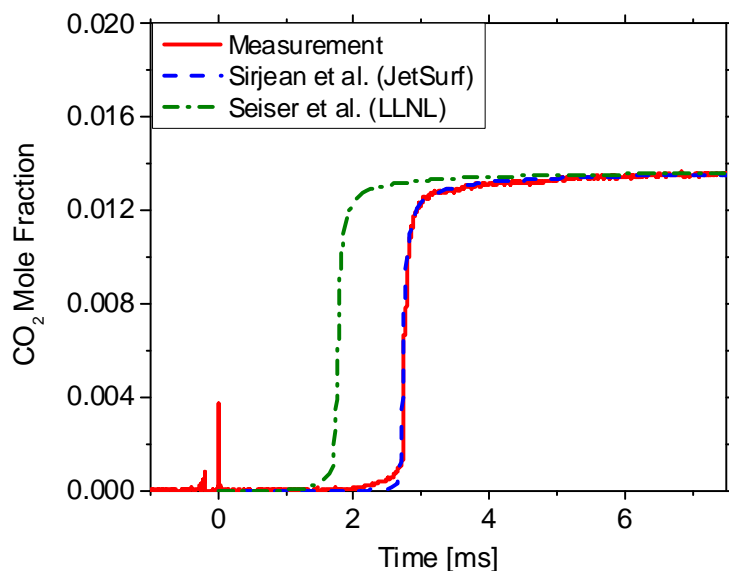


Figure 2.5.4. Measured CO_2 mole fraction behind a reflected shock wave arriving at $t = 0$. Mixture: 0.2% heptane, 2.2% O_2 , balance Ar. $T_5 = 1212$ K, $P_5 = 9.05$ atm, $L = 14.13$ cm, driver gas: 30% N_2 in He. Simulations using two kinetics mechanisms also are shown [31,36].

of 30% N₂/He and driver-inserts were used to achieve longer, uniform test time. The measurement was compared with two the predictions of chemical mechanisms from Sirjean et al.[31] and from Seiser et al [36]. The measured CO₂ time history was in significantly better agreement with the JetSurf simulation. Such measurements are very useful in the development, refinement, and validation of detailed kinetics mechanisms for new fuels and fuel blends.

2.5.2. Line Mixing and Finite Duration Collision Effects

As discussed earlier, sensors operating at high pressures compare the measured absorption with the simulated values to infer gas properties (mole fraction, temperature, etc.). At lower pressures, the diode laser wavelength can be swept across an entire absorption feature, and the mole fraction of the absorbing species can be deduced directly from the measured integrated absorbance and the knowledge of the line strength. At higher pressures the use of this strategy is limited by the broadening and overlap of discrete transitions. Thus, it is important to have an accurate line shape model that can be used to simulate high-pressure spectra at the experimental conditions. Most of the line shape models (e.g. Voigt, Lorentzian, Galatry, etc.) were developed for isolated lines and work very well at low gas densities. These models assumed the impact approximation and ignored collisional interference (line mixing) effects. At high gas densities, these assumptions break down, and the line shape cannot be simulated accurately with these models. Although there is a long history in the literature to model these high-pressure effects, this topic remains an active area of research.

During the current AFOSR grant period, direct absorption measurements of CO₂ absorption were carried out at high gas densities (~30 amg) using DFB diode lasers near 3631 – 3635 cm⁻¹ and 3644 – 3646 cm⁻¹. A room-temperature stainless steel cell was used for these experiments with dilute mixtures of CO₂ in air and argon. Measurements were compared with Voigt simulations to study non-ideal effects at high pressures. The measurements showed increasing deviation from the Voigt/Lorentzian behavior as the pressure increases. The measurements indicated that the absolute deviation was different for the two diode laser wavelengths used here [34].

FTIR Measurements

Measurements were made with a Nicolet 6700 FTIR spectrometer equipped with an XT-KBr beam splitter, IR light source, and HgCdTe detector. The entire system was purged with N₂ gas to minimize ambient interference absorption from CO₂ and H₂O. The FTIR measurements were made from 3500 cm⁻¹ to 3800 cm⁻¹ (2.63 to 2.85 μm) to cover the ν₁+ν₃ and 2ν₂+ν₃ vibrational bands of CO₂. Representative spectra at 1 and 30 atm are plotted in Fig. 2.5.5. Also plotted are simulations based on HITRAN 2008 parameters using Voigt lineshapes. The accuracy of the measurements was checked by comparing the integrated area over the entire wavelength region for the measured and simulated spectra. Although the measurements of peak absorbance deviated from the Voigt simulations at high pressures, the integrated absorption should be and was the same when collected for the entire band.

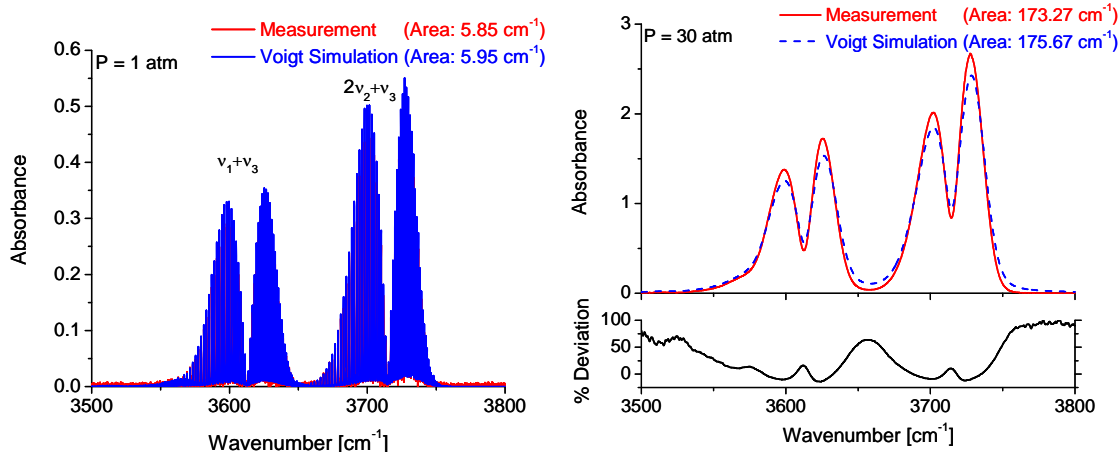


Figure 2.5.5 FTIR measurements for the CO₂ bands near 2.63 to 2.85 μm . T = 296 K, L = 5.77 cm, 1.49% CO₂ in air.

As was the case with DFB measurements over a wavelength range less than the entire band, the Voigt profile did a good job of describing the low-pressure spectra. At higher pressures, the Voigt/Lorentzian model underestimated the peaks and overestimated the wings of the vibrational bands. In other words, the measurements exhibited super-Lorentzian behavior near the band centers and sub-Lorentzian behavior in the wings of the bands. These two discrepancies were explained by the neglect of line mixing in the Voigt model [34]. The collisional population transfer (i.e. line mixing) moved intensity/population from the weak absorption regions to those of strong absorption. Hence, with respect to isolated line models that neglected internal population exchanges, line mixing induced a narrowing of spectral structures; hence, line mixing is often termed ‘rotational collisional narrowing’. The 30 atm plot also shows the % deviation of the measurement from the Voigt model. The deviation can be as high as 100% and was largest in the wings of the bands. Far from the most intense lines, the finite duration of collisions was observed to become important. The spectra in the far wings thus were affected by line mixing as well as finite duration of collision effects, and it was not possible to discriminate the individual influence from each mechanism. For radiators with closely spaced lines and relatively narrow vibrational bands (e.g. CO₂, CO), line mixing was efficient in the wings due to the overlapping of the line contributions. On the other hand, for radiators with widely spread lines and broad vibrational bands (e.g. H₂O), the influence of line mixing was important only in the far wings. In the intermediate region, the profile was dominated by the influence of the finite duration of collisions, which may have been the source of the observed super-Lorentzian behavior in the mid-wings.

Measurements of CO₂ absorption also were made in a CO₂-Ar mixture with the FTIR to study the effects from a different perturber. The Voigt simulation in this case was calculated by replacing the air broadening coefficient (γ_{Air}) of CO₂ transitions in the HITRAN file with a typical value of the Ar-broadening coefficient ($\gamma_{\text{Ar}} = \gamma_{\text{Air}}/1.25$). The deviation of the measured CO₂-Ar spectra with the Voigt model was compared with the deviation for CO₂-air mixture in Fig. 2.5.6. Except for the regions near the start and end of spectra where absorption was small and it was difficult to conclude which of the deviations was larger, almost everywhere else the deviation for the CO₂-Ar mixture was smaller compared with the CO₂-air. This observation can be attributed to the efficiency of

radiator-perturber collisions and the smaller line broadening of CO₂ transitions with Ar compared with air.

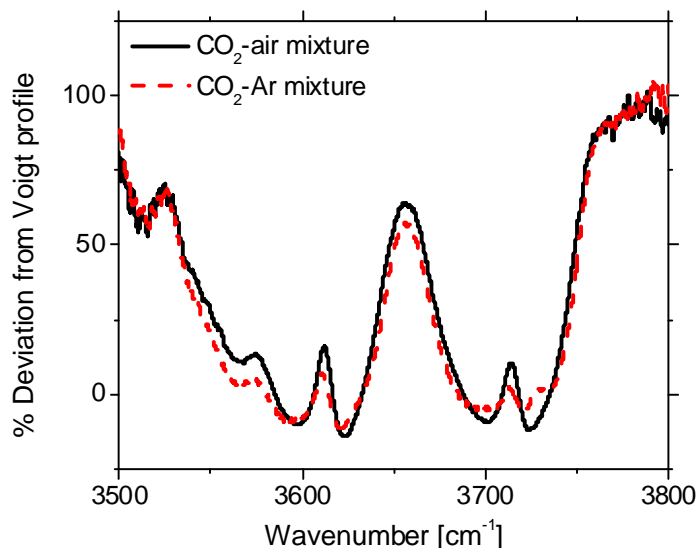


Figure 2.5.6 Deviation of the measured FTIR spectra with the Voigt model. $T = 296$ K, $L = 5.77$ cm, $P = 30$ atm.

Modeling of High-Pressure Spectra

The line shape models in common use were developed for isolated lines and rely on the impact approximation. As the gas density increases, these assumptions become invalid, and the models cannot predict the spectra accurately. There have been various modeling efforts to take high-pressure effects into consideration. Until recently, the most widely used approach was an empirical model, known as the ‘ χ factor approach’ [34]. This method introduced a frequency-dependent line shape correction χ modifying the Lorentzian/Voigt profile in the wings. This empirical approach can lead to very accurate predictions of the wings, when accurate laboratory measurements are used in the fits; however, there are a few problems associated with the use of χ factors. The first is that measured laboratory spectra generally do not cover all conditions of applications. Some spectral regions and/or temperature dependences may not have been studied because of experimental restrictions. Secondly, since the χ factors are deduced by fitting the measured spectra with a Lorentzian model based on a spectral database, the empirical χ factors are database dependent. As the database is updated or a new database is used, the χ factors must be reevaluated. Thirdly, the χ factor approach does a satisfactory job in the wings of the bands but usually it cannot model the super-Lorentzian behavior near the band centers.

We have used the χ functions of Perrin and Hartmann [37] to compute the simulated spectra at 30 atm, as shown in Fig. 2.5.7. The χ factor corrected Voigt model did a good job of predicting the absorbance in the wings but greatly under-estimated the absorption near band centers as χ was less than 1 for all frequencies.

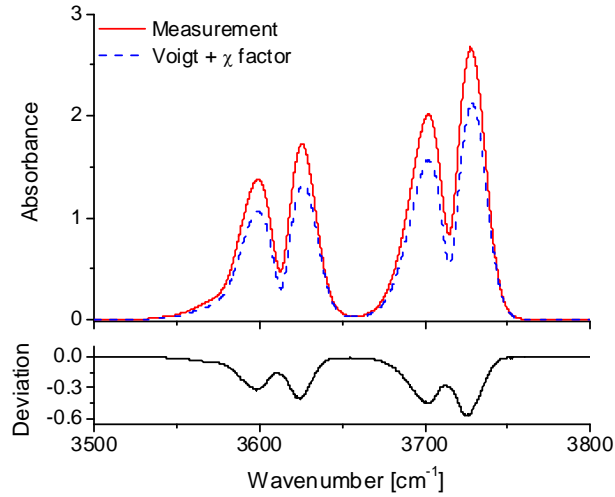


Figure 2.5.7 Comparison of the measurement with the χ factor-corrected Voigt model. T = 296 K, L = 5.77 cm, 1.49% CO₂ in air, P = 30 atm.

The phenomenon of line mixing has been the subject of various modeling efforts using empirical approaches, energy gap fitting laws, scaling laws, and quantum models. Among these models, scaling laws based on the energy-corrected sudden (ECS) approximation have generated the most interest. The basic idea of scaling laws is to separate the spectroscopic (related to the radiator internal states) and dynamical (related to the radiator-perturber interactions) effects. The ECS approach accounts for the coupling and relaxation of the angular momenta by representing the effective range of radiator-perturber interactions through a ‘scaling length’. A relatively new ECS based model was developed by Niro et. al.[38] for the CO₂ infrared bands between 10 and 20 μ m. The modeling was an extension of the earlier work that computed line mixing effects in CO₂ infrared Q branches. A comparison between the simulated spectra using this model and the measured spectra near 2.7 μ m is shown in Fig. 2.5.8 for the 30 atm case.

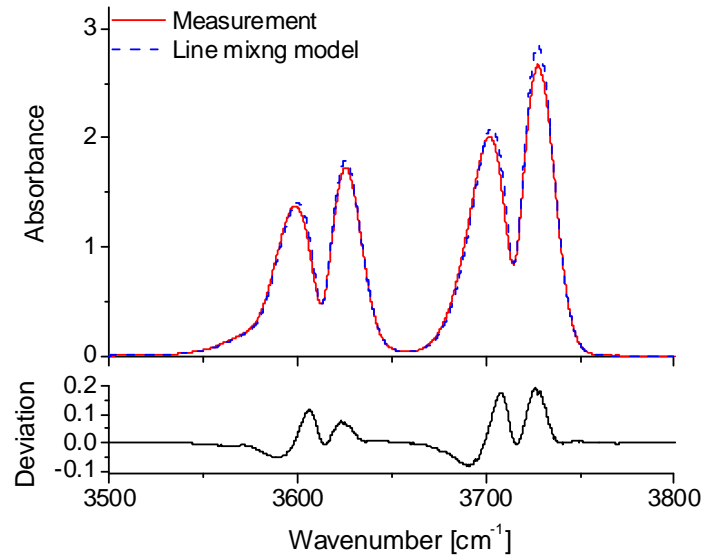


Figure 2.5.8 Comparison of the measurement with the line mixing model of Niro et. al. T = 296 K, L = 5.77 cm, 1.49% CO₂ in air, P = 30 atm.

The ability of this line mixing model to describe the absorption strength accurately in the wings of the two CO₂ bands points to the fact that at this density (~30 amg) and detuning (~100 cm⁻¹) the finite duration of collision effect was negligible. The sub-Lorentzian behavior in the wings was attributed predominantly to line mixing. At higher densities and/or further away from line centers, the finite duration of collisions may not be negligible and would require a non-impact treatment. For the experimental conditions of this work, the model did a great job at most of the frequencies except near the most intense lines of P and R branches where it overestimated absorption by ~ 4 – 9%. Although it was difficult to pinpoint the exact reason for the discrepancy between the model and the measurement, one possible explanation could be the use of ECS parameters (effective collision duration, vibrational band coupling) that were determined previously from the fits of measured Q branch (at 618 cm⁻¹) profiles and line widths. These parameters may need to be reevaluated for the 2.7 μm CO₂ bands. It should, however, be emphasized that the model did a good job overall and worked better than all other models tested for the 2.7 μm wavelength region.

High-Pressure Combustion Diagnostic

Previously we have demonstrated that WMS could be used for accurate CO₂ measurements up to ~ 10 amg by using the Lorentzian line shape model. At higher densities, the absence of discrete rotational structure limited the use of WMS strategies, and new diagnostic solutions were required. Previous CO₂ sensors near 2.7 μm have relied on using CO₂ rotational transitions that were free from water vapor interference; however, as the spectra were broadened and blended at high densities, access to discrete transitions was no longer possible and it became quite difficult to avoid H₂O interference. This difference between discrete and blended spectra is demonstrated in Fig. 2.5.9 by the simulated CO₂ and H₂O data at 50 atm and 1500 K. The water vapor lines are spaced more widely than CO₂ lines so the H₂O rotational structure exists even at such a high pressure. There are no wavelengths where CO₂ absorption is unaffected by the water vapor interference. Measuring CO₂ under such conditions would require the use of a multi-wavelength strategy. Such a diagnostic most probably will rely on simultaneous measurements of fixed-λ direct absorption, which requires comparing the measured absorption with simulations to infer mole fraction or other gas properties. To determine effective measurement strategies, it is critical to have reliable line shape models to simulate the CO₂ and H₂O spectra accurately at high pressures and temperatures. In addition, these models must include line mixing and the effects of the finite duration of collisions. As these effects are dependent on gas density, verifying the model performance in room-temperature, high-pressure experiments is an important first step. The final goal, however, would be to test the accuracy of the line shape model in controlled high-pressure, high-temperature experiments before its application to combustion problems.

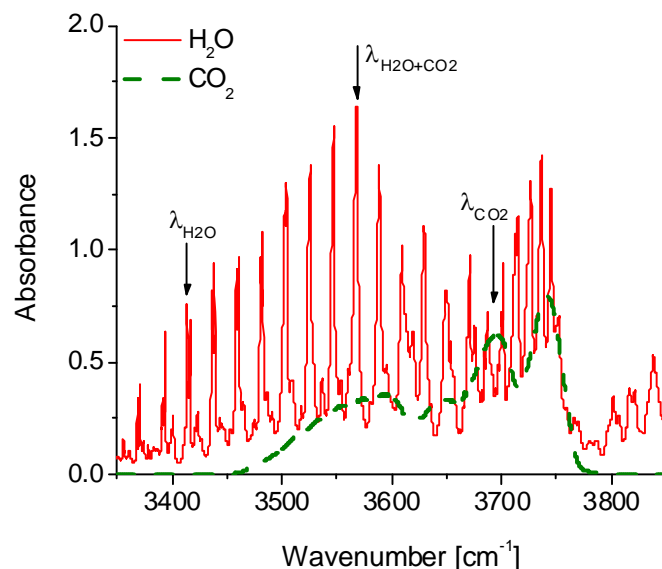


Figure 2.5.9 Simulated (Voigt) CO₂ and H₂O spectra. P = 50 atm, T = 1000 K, L = 10 cm, 1% CO₂, 1% H₂O, balance air [34].

2.6 Multi-Wavelength MIR Fuel Diagnostics

In AFOSR sponsored work, we demonstrated quantitative hydrocarbon fuel sensing using commercially available mid-infrared tunable diode laser sources [39,40]. Hydrocarbon absorption at MIR wavelengths uses transitions in the fundamental C-H stretching vibrational mode, where the absorption cross section is much larger than that of the vibrational overtone and combination bands accessed by NIR lasers. Thus, MIR fuel sensing offers substantially higher sensitivities, allowing accurate fuel measurements at low concentrations and short pathlengths. Furthermore, the broader spectral features of the large hydrocarbon molecules found in jet fuels allow different sensing strategies that are often insensitive to pressure broadening, removing the need for extensive characterization of pressure broadening common to NIR sensors probing discrete absorption transitions of smaller molecules. We have developed new approaches for fast measurements of fuel concentration and temperature in two important combustion environments: high temperature gases [41,42] and multi-phase [43,44], vapor in the presence of liquid aerosol and liquid films, both important for the characterization and study of air-breathing propulsion.

Background

The enabling technology for these new fuel sensing strategies is the recent commercial development of all-solid-state, wavelength-tunable MIR laser sources using difference-frequency-generation (DFG). The ability to tune or select the specific sensor wavelength is very important for MIR absorption sensing, as it allows selection of a wavelength that avoids potential interference from structured absorption of water vapor combustion products. The wavelength choice also allows the absorption strength to be selected from the broad unstructured hydrocarbon vibrational absorption features for the maximum

dynamic range of the absorption signal for the expected range of fuel concentrations and pathlength.

The spectroscopy of complex hydrocarbon fuel species is significantly different than those observed for small polyatomic compounds such as H_2O , CH_4 , C_2H_4 , or C_2H_2 , which all have well-resolved rotational-state-specific structure. The rotational structure in complex hydrocarbon fuel molecules is spaced closely and is blended by pressure and Doppler broadening into unresolved absorption features. The broad structure of the absorption spectrum motivates our work to develop multiple-wavelength absorption strategies that can provide quantitative measurements of the vapor concentration and temperature, even in the presence of attenuation of the laser beam from window fouling, scattering losses, or liquid films on windows.

Wavelength-Tunable MIR Laser Source Using DFG

Wavelength-tunable MIR lasers using difference-frequency-generation in periodically poled lithium niobate (PPLN) have been commercialized recently by a San Francisco start-up company (NovaWave). The laser design, illustrated in Fig. 2.6.1, combined and amplified two NIR wavelength-tunable diode signal lasers; this light then was combined with a powerful single-frequency diode laser (pump). The NIR signal and pump laser wavelengths then were mixed in a PPLN crystal to produce laser light at the difference frequency (here near $3.4\text{ }\mu\text{m}$ in the MIR). The wavelength of the MIR light was tuned by changing the wavelength of the NIR seed laser. When, as illustrated in Fig. 2.6.1, two signal lasers were time multiplexed rapidly (we have demonstrated up to 200 kHz), the output consisted of a beam that alternated between two different colors of MIR light. The current laser, procured on our AF DURIP, used a wavelength-dithering concept we suggested to the vendor, and enabled us to separate the two MIR colors by $\sim 20\text{ cm}^{-1}$, which was well-suited for measurements of fuel concentration and temperature as described below for n-dodecane and n-heptane vapor at high temperatures and n-decane vapor concentration and liquid film thickness measurements. Multiple DFG systems also were used to provide the greater wavelength separation needed for measuring n-decane vapor concentration and temperature in the presence of evaporating liquid fuel aerosols.

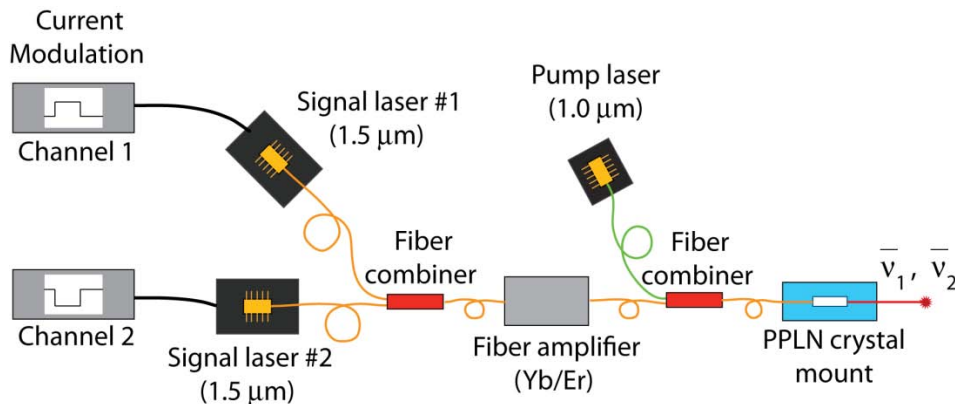


Figure 2.6.1 Schematic of DFG system. Two NIR signal lasers are modulated at 1 kHz to provide time-multiplexed MIR light at two wavelengths.

Laser Absorption Spectroscopy

In direct absorption spectroscopy, narrowband laser light is passed through a gas sample and the fractional transmission (I/I_o) of light is related to the concentration of the absorbing species by Beer's law (which briefly is discussed here to provide a self-contained report and define our notation):

$$Abs \equiv -\ln\left(\frac{I}{I_o}\right)_{\bar{\nu}} = \sigma(\bar{\nu}, T) n_a L \quad 2.6.1$$

where Abs refers to the absorbance, I_o and I are the incident and transmitted laser intensities, $\sigma(\bar{\nu}, T)$ [cm^2/mole] is the temperature- and wavelength-dependent absorption cross-section, n_a [mole/cm^3] is the concentration of the absorbing vapor species, $\bar{\nu}$ [cm^{-1}] is the optical frequency in wavenumbers, and L [cm] is the pathlength. For relatively large polyatomic hydrocarbons (e.g. n-heptane, n-dodecane) the individual absorption transitions overlap, forming a broad spectrum nearly independent of pressure. For such species, Beer's law is written in terms of absorption cross section instead of the line strength used for species with well-resolved spectra. The concentration of the absorbing species, n_a , (e.g. the fuel), can be determined by measuring the fractional transmission at one wavelength if the cross sections and temperature are known.

To measure the gas temperature, an additional wavelength is needed, as the ratio of absorbance at two wavelengths can be reduced to a function of temperature.

$$\frac{Abs_{\bar{\nu}_1}}{Abs_{\bar{\nu}_2}} = \frac{\sigma(\bar{\nu}_1, T) n_a L}{\sigma(\bar{\nu}_2, T) n_a L} = \frac{\sigma(\bar{\nu}_1, T)}{\sigma(\bar{\nu}_2, T)} = f(T) \quad 2.6.2$$

For accurate temperature measurements, the ratio of absorption at these wavelengths should vary strongly over the temperature range of interest, and the development of rules for wavelength selection has been an important part of this research.

2.6.1 FTIR Spectroscopy

Accurate laser-absorption measurements of concentration and temperature require quantitative absorption cross sections for the hydrocarbon fuels of interest. Common hydrocarbon fuels at room temperature primarily are liquid phase with a vapor pressure well below the value needed for stoichiometric combustion. These fuels fully vaporize only at elevated temperatures in combustion environments; thus, successful sensing must account for fuel vapor, liquid fuel droplets, and perhaps liquid fuel films on optical access windows and other surfaces. Such measurements require a spectroscopic absorption cross section database for both liquid and vapor phase fuel. The needed data were collected using a Nicolet 6700 Fourier transform infrared (FTIR) spectrometer fitted with vapor and liquid absorption cells. A schematic of the vapor FTIR experimental setup is shown in Fig. 2.6.2.

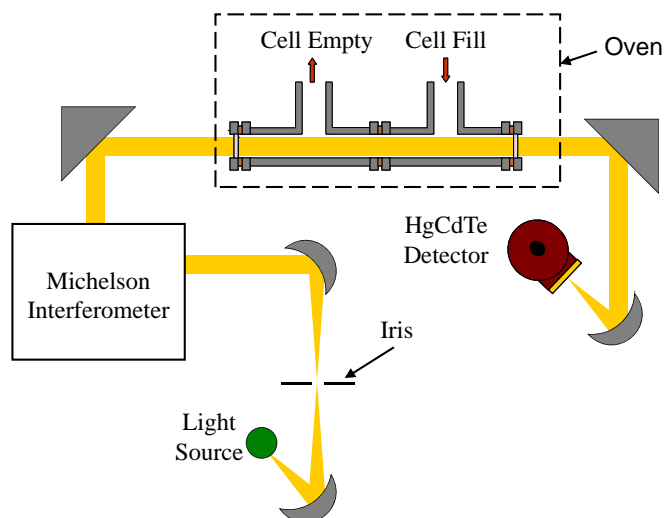


Figure 2.6.2 Experimental setup for optical absorption using an FTIR spectrometer.

As shown in Fig. 2.6.2, the broadband light source of the Nicolet 6700 was focused through an aperture and then collimated. The collimated beam entered a Michelson interferometer, where each wavelength was intensity modulated at a different modulation frequency. The modulated beam traveled through an external heated cell filled with either a gaseous or liquid sample and was collected and focused onto a detector. The detector signal was redirected back to the FTIR, where vendor software performed the Fourier transform calculations, separating the different frequency components and calculating the relative spectral intensity. The wavelength-dependent absorption cross sections were calculated from these data with knowledge of the sample composition, pressure, and pathlength.

Vapor-Phase Hydrocarbon Spectral Database

The temperature-dependent absorption cross sections of vapor-phase hydrocarbons were studied to tailor optical-absorption diagnostics to the hydrocarbon species or fuel blend of interest and to yield quantitative concentration measurements [45]. The temperature-dependent absorption spectra in the $3.4\ \mu\text{m}$ region of the C-H stretch of 26 hydrocarbon species were measured for temperatures ranging from 25 to 530°C at a nominal pressure of 1 atm (details of the measurement conditions are presented in Table 2.6.1). The selected species were among the most common species in blended hydrocarbon fuels, surrogate fuels, or exhaust gases of combustion systems and were therefore strong candidates for hydrocarbon diagnostics research. Because many of these hydrocarbons are present in systems where the temperature varies over a wide range (e.g., during injection into gas turbines), it is crucial to obtain spectral information over a large temperature range. The measured cross-section spectra were used to design the single- and multi-wavelength sensors described below. Sample temperature-dependent spectra for n-dodecane from these FTIR measurements are shown in Fig. 2.6.3.

Table 2.6.1 Experimental details of measured hydrocarbon spectra [45].

Name	Structural Class	Purity [%]	Temperature Range [C]	Resolution [cm ⁻¹]	Mole Fraction [%]	Vapor Pressure at 25 ° C [torr]	Molecular Weight [g/mole]
Ethanol	alcohol	99	25-325	0.1	1.0-2.3	59.55	46.07
Formaldehyde	aldehyde	??	100-350	0.1	0.4-1.0	gas	30.03
Methane	alkane	99	25-500	0.1	0.4	gas	16.04
Benzene	aromatic	99	25-500	0.1	1.6-3.7	95.8	78.11
Toluene	aromatic	99	25-500	1	1.0-1.5	28.3	92.14
m-xylene	aromatic	99	25-500	1	0.4-0.6	8.7	106.17
Ethyl-benzene	aromatic	99	25-500	1	0.3-0.6	9.5	106.17
O-xylene	aromatic	98	25-500	1	0.3-1.4	6.7	106.17
3-ethyl-toluene	aromatic	99	25-500	1	0.2-0.4	3.04	120.19
2-methyl-propane	branched alkane	99	25-500	0.1	0.3-1.7	gas	58.12
2-methyl-butane	branched alkane	99.5	25-500	1	0.2-1.1	686.3	72.15
2-methyl-pentane	branched alkane	99	25-500	1	0.4-1.3	211.4	86.18
3-methyl-hexane	branched alkane	99	25-500	1	0.6-1.0	62.2	100.2
2,2,4-trimethyl-pentane	branched alkane	99	25-500	1	0.3-1.6	49.6	114.23
Ethylene	olefin	99.5	25-500	0.1	0.7-1.7	gas	28.05
Propene	olefin	99	25-500	0.1	1.0-6.0	gas	42.08
1-butene	olefin	99	25-500	0.1	1.2-2.6	gas	56.11
2-methyl-2-butene	olefin	99	25-500	1	0.06-2.3	473.4	70.13
cis-2-pentene	olefin	98	25-500	1	0.7-2.5	501.2	70.13
2-methyl-2-pentene	olefin	98	25-500	1	0.4-1.8	156.5	84.16
1-heptene	olefin	97	25-500	1	0.2-1.2	56.5	98.19
2,4,4-trimethyl-1-pentene	olefin	99	25-450	1	0.3-1.3	46.1	112.21
Ethane	straight alkane	99	25-500	0.1	0.8-1.7	gas	30.07
n-pentane	straight alkane	99	25-500	1	0.4-1.3	521.6	72.15
n-heptane	straight alkane	99	25-500	1	0.3-1.1	46.2	100.2
n-dodecane	straight alkane	99	50-500	1	0.07-0.1	0.14	170.33

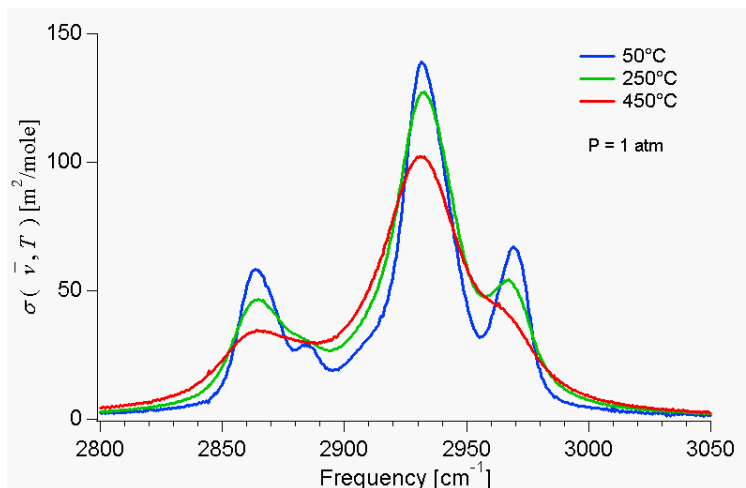


Figure 2.6.3 Temperature-dependent absorption spectrum of n-dodecane for temperatures ranging from 25 to 500± C at 1 atm of total pressure with resolution of ~1 nm (FWHM).

Liquid-Phase Hydrocarbon Absorption Measurements

Measurements of the absorption spectra of liquid-phase hydrocarbons in the 3.4 μm region of the C-H stretch were needed to develop quantitative diagnostics to account for droplets and films of liquid-phase hydrocarbons [46]. A FTIR transmission technique provided quantitative absorption and refractive index spectra of the fundamental C-H

stretch vibration band using a short pathlength optical cell designed for liquids. Very short pathlengths were required, as the absorption in liquids is orders of magnitude stronger than in vapor due to increased density.

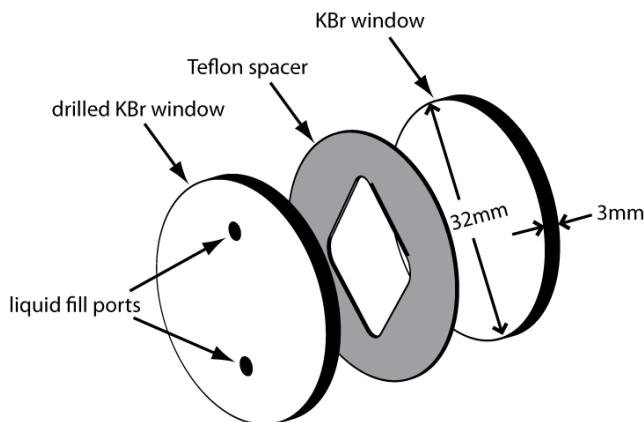


Figure 2.6.4 Optical cell used in liquid absorption measurements. Teflon spacers with thicknesses between 0.5 mm and 15 μm were used.

Liquid phase absorption measurements were used to determine the complex refractive index of the fuels studied. The wavelength-dependent refractive index of an absorbing medium can be written as a complex function.

$$m(\bar{\nu}) = n(\bar{\nu}) + ik(\bar{\nu}) \quad 2.6.3$$

The real part of the refractive index, n , is related, through the Fresnel equations, to the reflection and transmission of light at the interface of disparate media. The imaginary part of the refractive index, k , is related to optical absorption by the following relation:

$$k(\bar{\nu}) = \frac{n_a \sigma(\bar{\nu})}{4\pi\bar{\nu}} \quad 2.6.4$$

Thus, the imaginary refractive index is determined directly from the measured absorption cross section. For our work, the real part of the refractive index was found using Kramers-Kronig dispersion relations. Measurements were made of 3 pure hydrocarbons: toluene, n-decane, and n-dodecane, and 3 gasoline fuel blends. Example data for n-decane at 25°C and 1 atm are shown in Fig.2.6.5. The measured spectra also were compared with vapor-phase spectra of the same hydrocarbons revealing a shift of 8 cm^{-1} in the location of the liquid's absorption C-H stretching band relative to the vapor spectra, which was exploited to make liquid-fuel-film measurements.

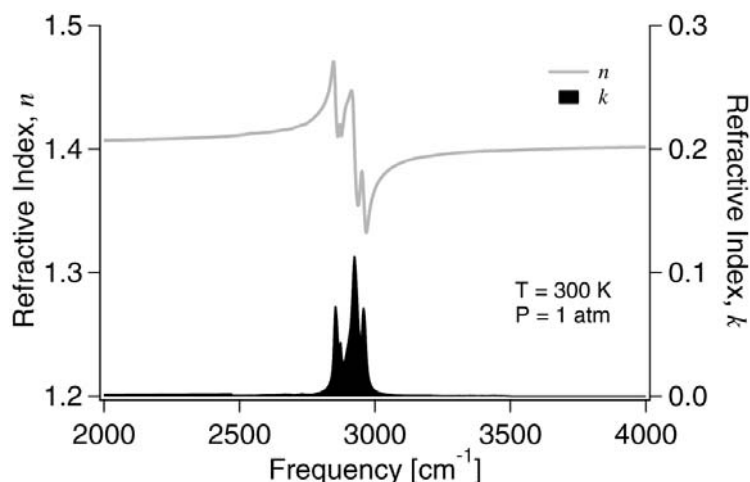


Figure 2.6.5 Measured complex refractive index of liquid n-decane in the infrared [40].

2.6.2 Vapor-Phase Fuel Diagnostics

Concentration and Temperature of n-Heptane and n-Dodecane in Shock Tubes

MIR laser-absorption diagnostics were developed for two important hydrocarbon compounds: n-heptane, which has chemistry that is an important sub-mechanism for any blended fuel [36,47] and n-dodecane, which is an important surrogate for jet fuel [48,49]. The study of fuel kinetics over a range of temperatures and pressures is an important research direction within our laboratory. In particular, we are interested in providing a full suite of laser-based diagnostics capable of measuring shock tube time histories of combustion reactants, intermediates and products, which are valuable data for validation of combustion chemistry mechanisms.

Wavelength Selection

Wavelengths for both the n-heptane and n-dodecane diagnostics were selected from the temperature-dependent cross section spectra measured with the FTIR. Wavelength pairs were chosen that provided sufficient absorption with maximum sensitivity to temperature. As shown in Fig.2.6.6, the same pair of wavelengths was chosen for both fuels ($\bar{\nu}_1 = 2913 \text{ cm}^{-1}$, $\bar{\nu}_2 = 2933 \text{ cm}^{-1}$) [41].

Experimental Setup

Fuel concentration and temperature were demonstrated in two different shock tube facilities over the range from 300K to 1300K. The n-heptane diagnostic was demonstrated in the high purity kinetics shock tube designed for higher vapor pressure species, and the n-dodecane diagnostic was demonstrated in the aerosol shock tube [50]. This aerosol was evaporated by the incident shock, and combustion chemistry of the vapor-phase fuel was studied behind the reflected shock. This shock tube provided relatively high concentrations of low-vapor pressure species (e.g., n-dodecane) by entraining a liquid aerosol in the test gas. The experimental setups are shown in Fig.2.6.7. In both shock tubes, DFG laser light was passed through the shock tube near

the endwall. This arrangement allowed the diagnostic to capture step increases in temperature as the incident shock passed by, followed by passage of the shock reflected from the endwall.

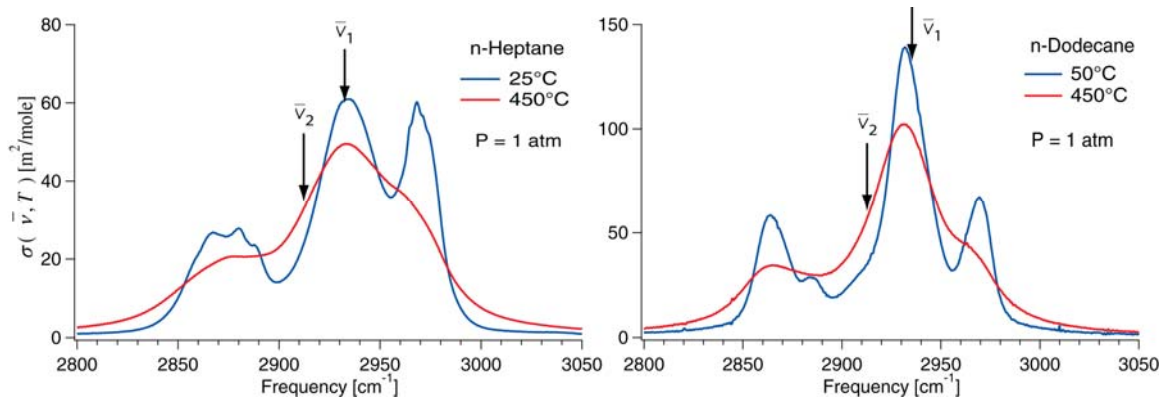


Figure 2.6.6 Wavelengths selected for concentration and temperature measurements in n-heptane (left) and n-dodecane (right).

Measurements

The high-purity shock tube was used with n-heptane diluted in an argon bath gas to provide high-temperature absorption cross section data (FTIR measurements were limited to 500°C) and to validate concentration and temperature measurements. The validated diagnostic then was used to study the high-temperature kinetics of n-heptane pyrolysis.

The two-wavelength temperature and vapor concentration diagnostic designed for n-dodecane was used to validate a model of post-evaporation conditions in an aerosol shock tube. The aerosol shock tube was filled with an n-dodecane aerosol with mean droplet diameter of $\sim 3 \mu\text{m}$ in an argon bath gas. The incident shock wave compressed the two-phase mixture, and the gas temperature increased, which caused the droplets to evaporate.

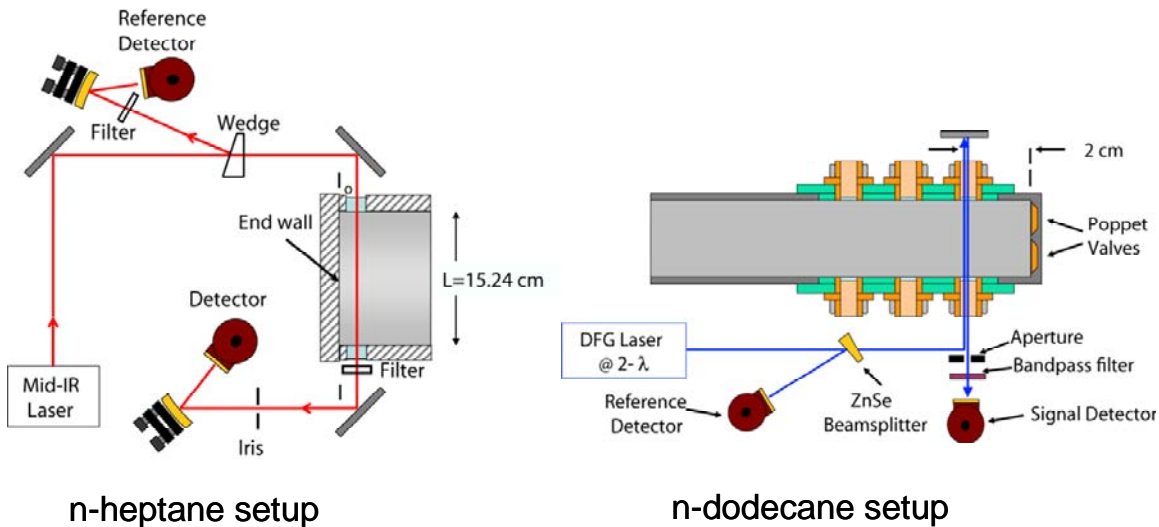


Figure 2.6.7 Experimental setup for shock tube demonstrations of diagnostics. n-heptane was measured in the high purity kinetics shock tube (left) [41]. n-dodecane was measured in the low vapor pressure fuel aerosol shock tube (right) [42].

When the reflected shock wave passed, the liquid had evaporated completely and the high-temperature chemistry of the gaseous mixture was examined. The 1-D shock-tube equations have been adapted to determine the post-shock conditions of a two-phase homogeneous mixture. Temperature-dependent cross sections were measured at the two wavelengths in shock-heated mixtures of vapor-phase n-dodecane and argon. The temperature-dependent cross sections then were used to infer post-evaporation temperature and n-dodecane vapor concentration in a series of two-phase shock tube experiments. The good agreement found between the model and the measurements provides confidence in the two-phase shock model [50].

Results

Representative concentration and temperature measurements using both diagnostics are shown in Fig. 2.6.8. The n-heptane shock measurements on the left side of the figure had a post-reflected shock temperature of ~ 1050 K and showed excellent agreement with the 1-D shock predictions for all three shock regions: pre-shock (region 1), post-incident shock (region 2) and post-reflected shock (region 5). The n-dodecane measurements on the right side of the figure showed significant thermal decomposition for a post-reflected shock temperature ~ 1200 K. Despite the significant decomposition, the diagnostic recovered the gas temperature within 10% in the post-reflected shock and within 3% in the pre-shock and post-incident shock regions.

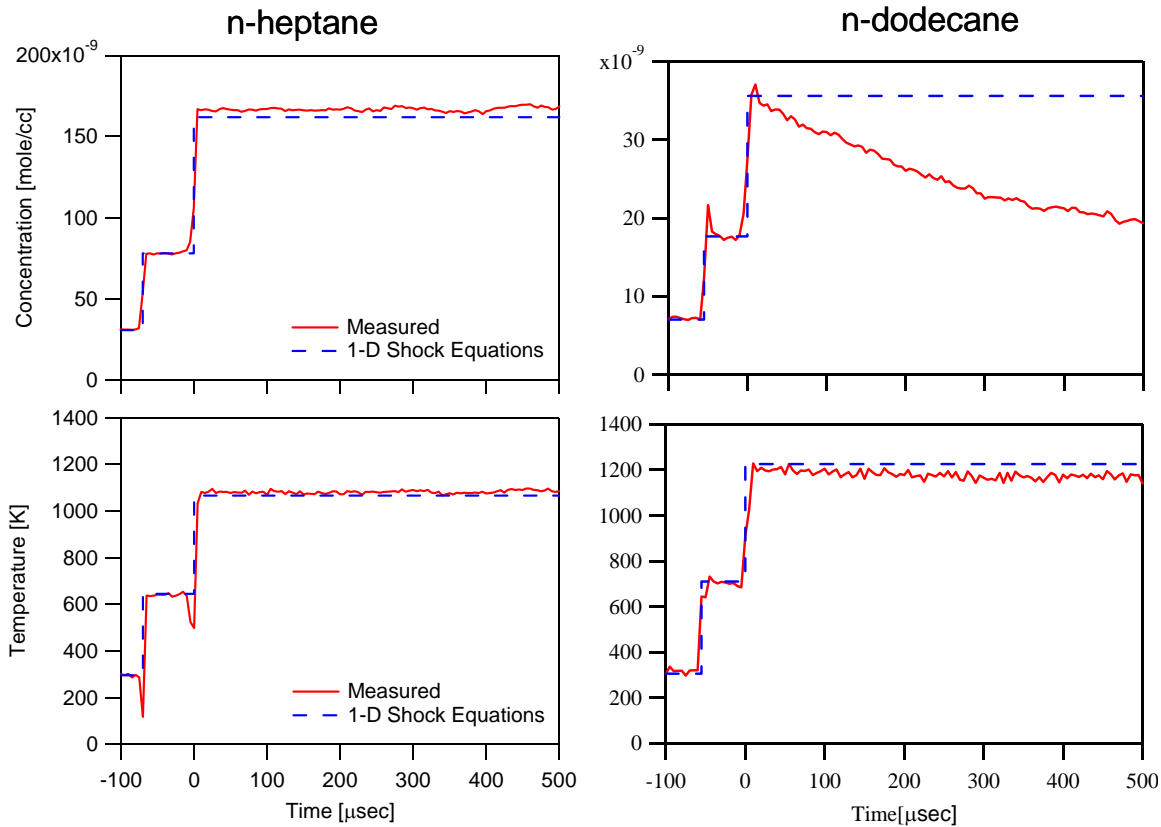


Figure 2.6.8 Time-resolved measurements of concentration and temperature of shock heated n-heptane with $T_5 \sim 1050$ K (left) and n-dodecane with $T_5 \sim 1200$ K (right) [42].

Figure 2.6.9 summarizes the data for all of the experiments performed covering the range of temperatures from 300 to 1320 K. The measured temperature and concentration were compared to the values using the 1-D shock equations. The measured n-heptane concentrations showed a 1.7% RMS deviation from the predicted values and the measured temperatures showed a 4.3% RMS deviation from the model, while the measured n-dodecane concentrations showed a 2.8% RMS deviation and the temperatures a 3.6% RMS deviation. Thus, the measured data were in excellent agreement with the values predicted by the 1-D equations.

n-Heptane Kinetics

The chosen wavelengths for the n-heptane diagnostic maximized the signal from n-heptane while avoiding many of the strong absorption features from product species. The measured removal rate of n-heptane was compared to model predictions using a mechanism developed by Chaos et al. [47] revealing that the mechanism underpredicted n-heptane removal rates. The unimolecular decomposition rates in the Chaos mechanism were adjusted to match the measured n-heptane time history, showing good agreement with our measurement (Fig. 2.6.10).

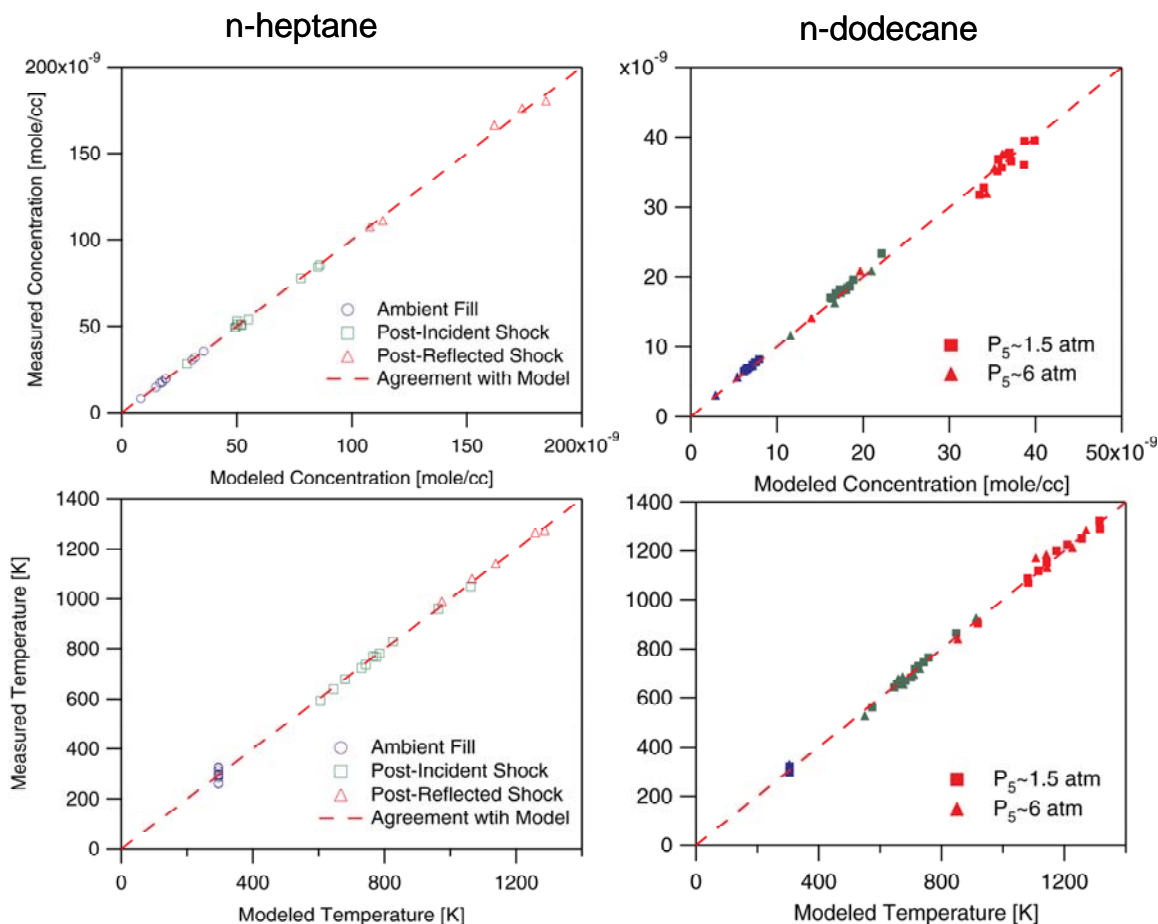


Figure 2.6.9 Accuracy of concentration and temperature measurements for all shocks of n-Heptane (left) and n-Dodecane (right).

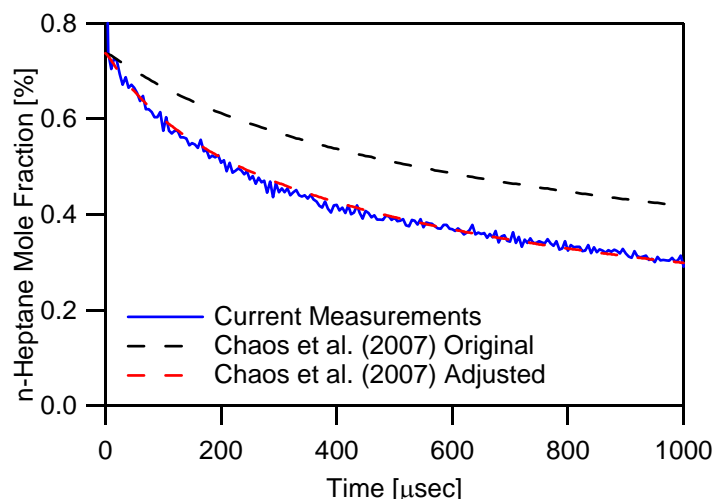


Figure 2.6.10 Measured and fit decomposition of 0.737% n-heptane in argon for a temperature of 1258 K and a pressure of 1.83 atm. Dashed lines represent calculations using the original and adjusted Chaos models [47].

2.6.3 Multi-Phase Fuel Measurements

As an extension of our work in hydrocarbon fuel sensing, we have begun work in multi-phase fuel environments. In practical combustion environments, fuels often are injected as a liquid spray that quickly evaporates at elevated temperatures and can produce liquid films on cold surfaces [51]. Direct measurement of vapor-phase properties (e.g. vapor-phase mole fraction and temperature) in the presence of droplets and films is valuable for studying the combustion of liquid sprays and aerosols, especially in practical devices such as gas turbine engines and direct-injection gasoline and diesel engines. Laser-absorption measurements at these conditions are difficult; however, because light scattering by liquid droplets and absorption from liquid fuel films on optical ports interferes with measurements of the vapor.

Two diagnostics were developed to study multi-phase fuel environments. First, a 3-wavelength MIR laser-based absorption diagnostic, which provides simultaneous measurement of temperature and vapor-phase mole fraction in a gas flow with evaporating aerosol, was designed and tested. Second, a two-wavelength MIR laser-based absorption diagnostic was designed and tested to provide simultaneous measurements of fuel vapor mole fraction and liquid fuel film thickness.

Vapor Concentration and Temperature in an Evaporating n-Decane Aerosol

FTIR measurements of the optical constants of liquid n-decane were combined with Mie theory to simulate the wavelength-dependent droplet extinction for an evaporating polydisperse n-decane aerosol. These simulations, combined with FTIR measurements of n-decane vapor, guided the selection of three wavelengths with temperature-dependent vapor absorption and constant droplet extinction ratios. Fast time-multiplexed measurements at these colors provided droplet extinction correction, gas temperature, and fuel vapor mole fraction. This technique was demonstrated using n-decane vapor and aerosol in a flow cell and aerosol shock tube [43].

Droplet Extinction by Fuel Aerosols

When an aerosol is present in the beam path, in addition to vapor-phase absorption, laser light is attenuated by droplet absorption and scattering (together called droplet extinction), which adds an additional term to Beer's law (2.6.1), leading to:

$$-\ln\left(\frac{I}{I_o}\right)_{\bar{\nu}} \equiv Ext(\bar{\nu}) = \sigma(\bar{\nu}, T)n_a L + \tau(\bar{\nu})L \quad 2.6.5$$

where $\tau(\bar{\nu})[\text{cm}^{-1}]$ is the droplet extinction coefficient, $Ext(\bar{\nu})$ is the combined extinction from the wavelength-dependent vapor absorption (first term) and droplet extinction (second term). From this expression and the ideal gas law, the vapor mole fraction and temperature can be found from the measured fractional transmission at two wavelengths using relations 2.6.1 and 2.6.2 if P and L are measured and if $\sigma(\bar{\nu}, T)$ and $\tau(\bar{\nu})$ are known at both wavelengths; however for an evaporating aerosol, $\tau(\bar{\nu})$ will vary in time, making any static correction prone to error. Instead, we used a three-wavelength technique that allowed us to infer a time-resolved $\tau(\bar{\nu})$. In a polydisperse aerosol, the droplet extinction coefficient is dependent on several parameters [52]; the total number density of droplets (droplet loading), $N[\text{cm}^{-3}]$, the droplet size distribution function, $f(D)[\text{cm}^{-1}]$; and the extinction efficiency, $Q_{ext}(D, m)$, which is a measure of a particle's ability to scatter and absorb light at different wavelengths. The extinction coefficient, $\tau(\bar{\nu})$, is determined by integrating these parameters over the full range of droplet diameters, D , present in the aerosol.

$$\tau(\bar{\nu}) = \int_{D_{\min}}^{D_{\max}} N \cdot f(D) \frac{\pi D^2}{4} Q_{ext}(D, m) dD \quad 2.6.6$$

The initial n-decane aerosol droplet size distribution produced by the nebulizer used in our measurements was measured previously to be approximately log-normal with a median diameter, D_{50} , of about $3.3 \mu\text{m}$. A simulation showing the initial $f(D)$ and the evolution of $f(D)$ with evaporation is shown in Fig. 2.6.11. This simulated evaporation

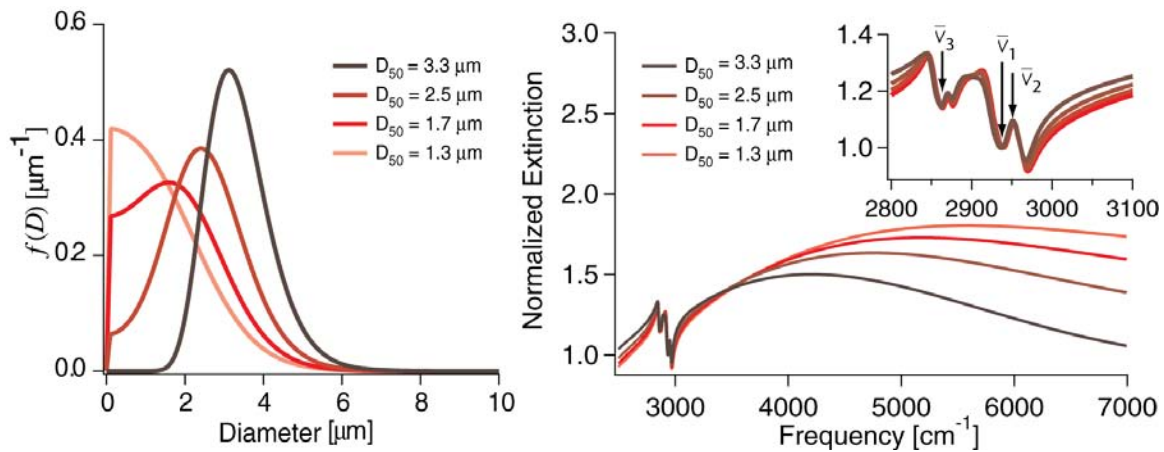


Figure 2.6.11 Modeled droplet size distribution and droplet extinction for evaporating n-decane aerosol. Normalized extinction curves reveal wavelengths with constant extinction ratios [43].

was used to calculate the expected droplet extinction using Mie theory calculations. Normalizing the wavelength-dependent droplet extinction resulted in 3 wavelengths for which the droplet extinction was constant (see the three labeled wavelengths in the inset of Fig. 2.6.11). These constant values of the normalized extinction provided the needed information to recover the three unknowns: concentration, temperature, and droplet extinction with measurements at only three wavelengths (3 equations and 3 unknowns).

Experimental Setup

The experimental setup is shown in Fig. 2.6.12, where the three MIR wavelengths were combined with a fourth NIR wavelength for droplet monitoring and passed through the aerosol shock tube near the endwall. The NIR wavelength was not absorbed by the gas and provided a direct measure of the presence of droplets.

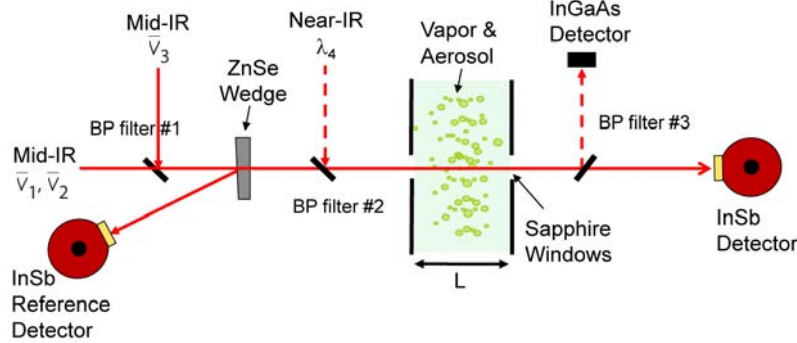


Figure 2.6.12 Aerosol diagnostic experimental setup. Three MIR wavelengths are combined with 1 NIR wavelength and passed through aerosol shock tube near the endwall.

Measurements

Measurements were made with an n-decane aerosol in an argon bath gas in the pre-shock, post-incident shock, and post-reflected shock regions. Example shocks are shown in Fig. 2.6.13 where the mole fraction and temperature are plotted versus time after the arrival of the incident shock. The NIR extinction was directly proportional to droplet loading and showed significant scattering interference in the quiescent aerosol-laden bath gas prior to arrival of the shock. Immediately after the shock's arrival the scattering signal rapidly increased due to the pressure rise behind the shock before quickly decreasing due to evaporation in the heated post-incident-shock gases. The measured mole fraction and temperature before the arrival of the shock agreed with the saturated condition and the ambient temperature, respectively. The measured mole fraction and temperature in the post-incident-shock region agree with the predicted amount of liquid evaporated to vapor and the modified 1-D shock equations, respectively. The modified shock equations include energy consumed due to the evaporation of the liquid aerosol, reducing the predicted temperature in the heated bath gas.

Results

Data from all the measured shocks are shown in Fig. 2.6.14. Results indicated that accurate measurements were possible when vapor absorption was less than droplet extinction. Measurements were made for vapor mole fractions below 2.3% with errors less than 10%. Temperature measurements were made over the range $300\text{ K} < T < 900\text{ K}$, with errors less than 3%. To our knowledge, these results were the first laser-

absorption measurements of both vapor mole fraction and temperature in the presence of an evaporating polydisperse hydrocarbon aerosol.

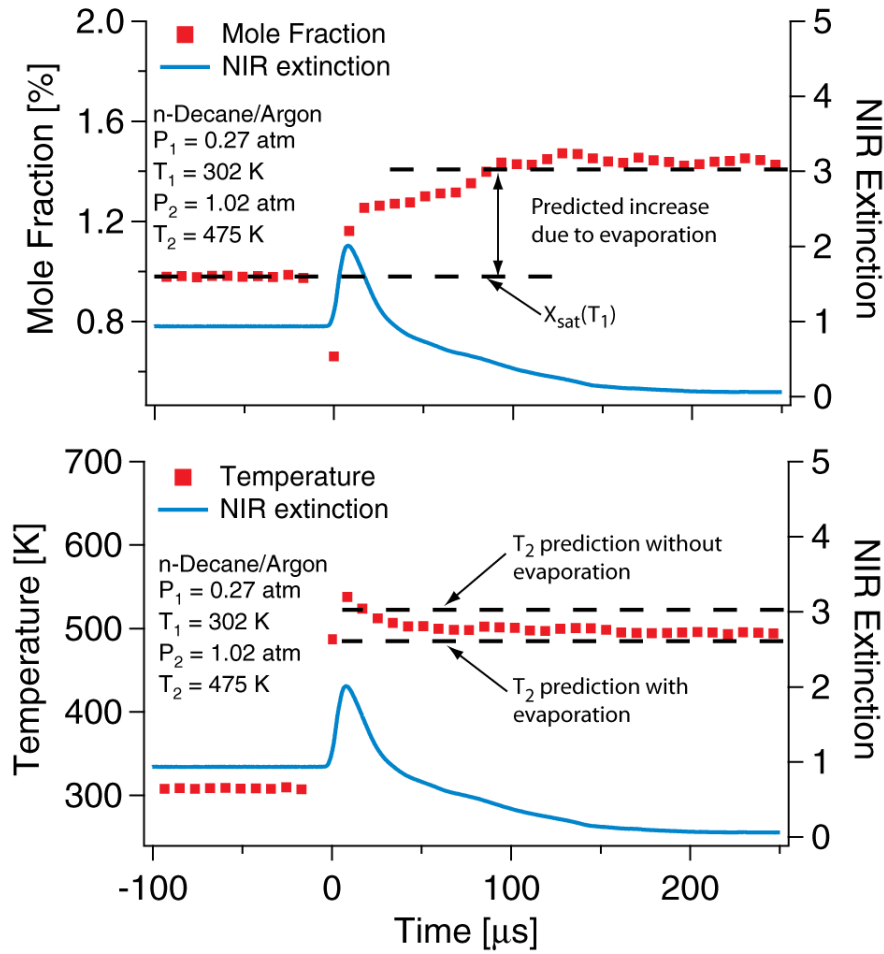


Figure 2.6.13 Measured mole fraction and temperature in the presence of evaporating n-decane aerosol before and after arrival of the incident shock wave.

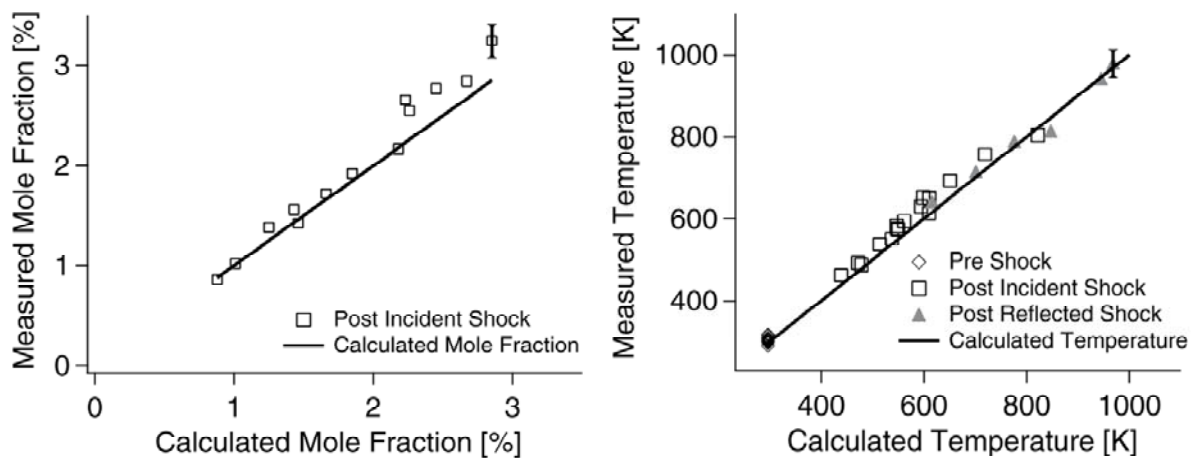


Figure 2.6.14 Results from all measured shocks: mole fraction compared to calculations (top) and temperature compared to calculations for all three shock regions (bottom) [43].

Vapor Concentration and Liquid Fuel Film Thickness

The second multi-phase laser absorption diagnostic [44] was developed for measuring vapor mole fraction and liquid film thickness for potential application in combustion environments where strong absorption by liquid fuel or oil films on windows make conventional direct absorption measurements of the gas problematic. The situation is presented in Fig. 2.6.15, where a film of unknown thickness, δ , is present on the optical window of a gas measurement cell. When laser absorption is due to a vapor and liquid film, Beer's law is modified to the following form, which assumes that light reflection at the window-film interface is minimized by refractive index matching:

$$-\ln\left(\frac{I}{I_o}\right)_{\bar{\nu}} = \sigma_g(\bar{\nu}, T_g)n_g L + \sigma_L(\bar{\nu}, T_L)n_L \delta \quad 2.6.7$$

The quantities are n_g and n_L , which are the molar densities of the gas and liquid, σ_g and σ_L , which are the absorption cross sections for the gas and liquid, T_g and T_L , which are the temperatures of the gas and liquid, δ , which is the liquid film thickness. Using this equation, if the liquid and gas temperatures are known, n_g and δ can be determined from the absorbance measured at two wavelengths (2 equations in 2 unknowns). Note this development assumes the thickness of the film is nearly constant over the diameter of the laser beam to avoid significant beam steering by refraction. Also the film roughness must be on a smaller scale than the beam diameter. Liquid hydrocarbons readily wet window surfaces and these assumed conditions are not unusual.

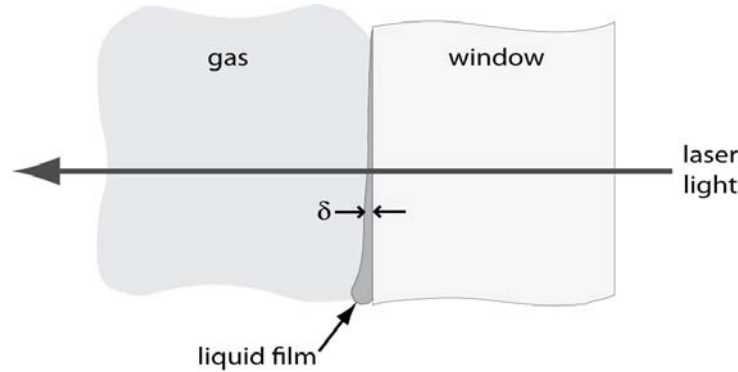


Figure 2.6.15 Schematic of laser light passing through a window, a fuel film of thickness δ , and fuel vapor.

Wavelength Selection

Optimal wavelengths were chosen from FTIR measurements of the C-H stretching band of vapor n-decane and liquid n-dodecane near $3.4 \mu\text{m}$ (3000 cm^{-1}), as constrained by the wavelength tuning range of our DFG laser. The measured spectral shift of 8 cm^{-1} in the location of the liquid's absorption C-H stretching band relative to the vapor spectra made this diagnostic approach possible. Wavelengths were chosen that maximized the independence of the two Beer's law equations: one wavelength was dominated by vapor and the other by liquid ($\bar{\nu}_1 = 2854.7 \text{ cm}^{-1}$, $\bar{\nu}_2 = 2864.7 \text{ cm}^{-1}$). Different fuels were used for film and vapor to avoid interference from evaporated liquid during the validation tests, as n-dodecane has a very low vapor pressure ($<0.1 \text{ torr}$ at 25°C).

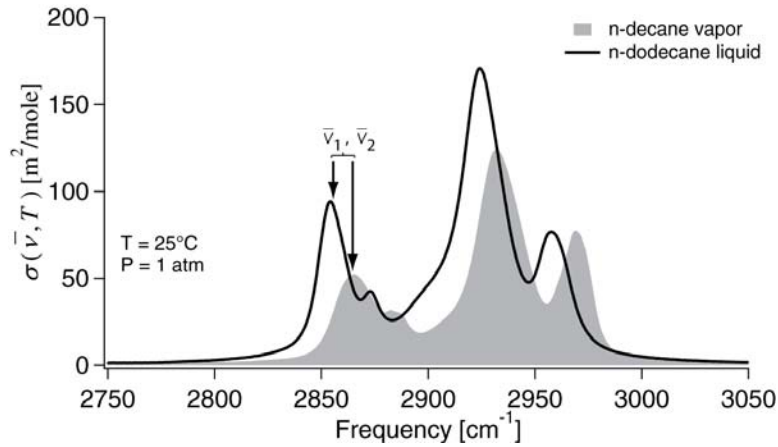


Figure 2.6.16 Wavelengths selected for measuring n-dodecane film thickness and n-decane vapor concentration simultaneously [44].

Experimental Setup

The diagnostic was demonstrated for n-dodecane films on CaF_2 windows in the absence and presence of n-decane vapor near 25°C. A schematic of a laser-absorption measurement of liquid film and vapor is shown in Fig. 2.6.17.

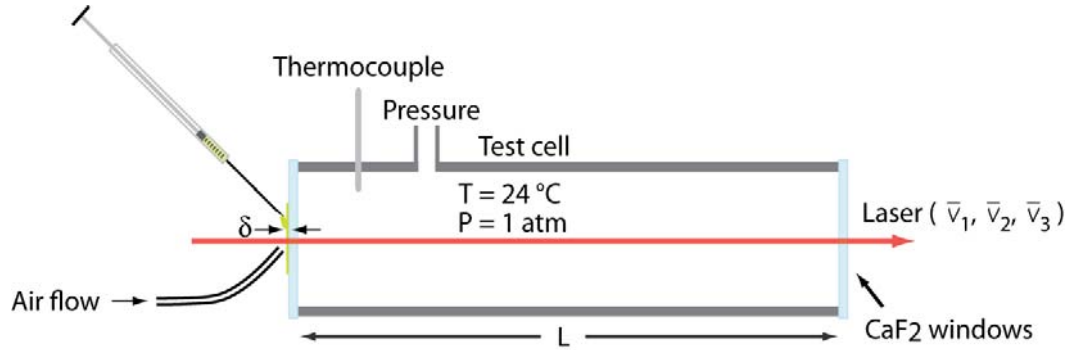


Figure 2.6.17 Schematic of gas cell used to hold n-decane vapor with n-dodecane film injected and removed from one window's outer surface. One NIR wavelength was used to monitor beam steering and scattering from the fuel injection.

Measurements

An example measurement is shown in Fig. 2.6.18. The top plot shows the total extinction of all three wavelengths versus time. The extinction at $\bar{\nu}_3$ (the NIR wavelength) showed initial beam steering and/or scattering due to the injection of the film. After this interference subsides, the MIR measurements were initially optically thick but quickly became measurable as the film thickness decreased below 10 μm . The resulting measurements of n-decane mole fraction and n-dodecane film thickness are shown in the bottom panel of Fig. 2.6.18.

Results

n-Dodecane films $< 20\ \mu\text{m}$ thick were measured accurately in the absence of n-decane vapor, as limited by an absorbance of ~ 4 for the thickest films. Thicker films could be measured by choosing wavelengths with smaller absorption cross-sections. By adjusting the wavelengths used, this technique is suitable for fuel films with thicknesses from $< 1\ \mu\text{m}$ up to $> 100\ \mu\text{m}$. Simultaneous measurements of n-dodecane films and n-decane vapor were demonstrated with 300 ppm of n-decane measured with $< 10\%$ uncertainty in the presence of n-dodecane films $< 10\ \mu\text{m}$.

Current Status

We continue to develop new MIR laser-absorption diagnostics using our DFG laser systems. Three directions of work are being pursued currently. First, we are extending liquid-phase sensing to three wavelengths to include gas temperature in addition to gas concentration and liquid film thickness, as temperature is important for practical applications in combustion environments. Second, we are extending our vapor-phase MIR diagnostics to include smaller hydrocarbons such as methane and ethylene, which are important intermediates in combustion chemistry. Finally, we are demonstrating the application of these MIR vapor-phase diagnostics for chemical kinetics studies of jet fuels and jet fuel surrogates in our aerosol shock tube.

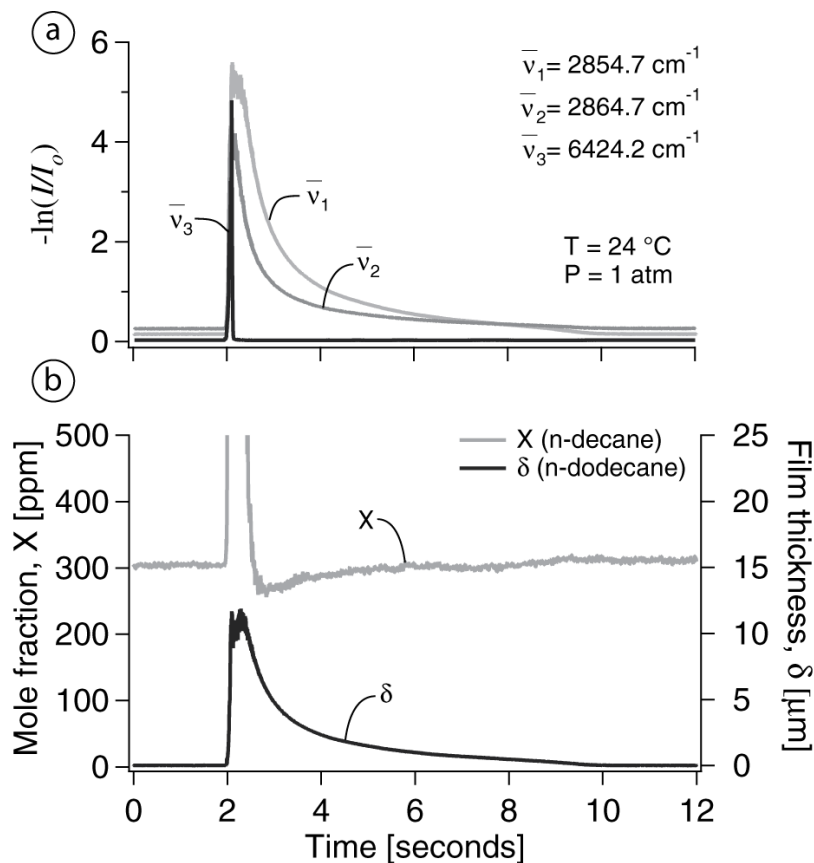


Figure 2.6.18 Measurements of n-dodecane film thickness and n-decane vapor mole fraction (b). The total absorption is shown in (a) [44].

2.7 Applications of TDL Sensors to Scramjets at AFRL

WMS- $2f/1f$ was introduced in section 2.4 of this report for laboratory measurements near atmospheric pressure and in section 2.5 for measurements at elevated pressures. In this section, the use of the WMS- $2f/1f$ method for measurements of gas temperature and concentration in the harsh environments of practical propulsion ground test is reported with emphasis on the laser theory and laser characterization needed for calibration-free implementation [53]. The method is applicable to measurements using lasers with synchronous wavelength and intensity modulation (such as injection current-tuned diode lasers). The key factors that enable measurements without the *in situ* calibration normally associated with WMS are: 1) normalization of the $2f$ signal by the first-harmonic ($1f$) signal to account for laser intensity, and 2) the inclusion of laser-specific tuning characteristics in the spectral absorption model that is used to compare with measured $1f$ -normalized, WMS- $2f$ signals to infer gas properties. The uncertainties associated with the calibration-free WMS method were studied in detail, with particular emphasis on the influence of pressure and optical depth on the WMS signals. Many of these uncertainties also were applicable to calibrated WMS measurements. The calibration-free WMS technique was used for measurements of temperature, H_2O , and CO_2 in a model scramjet combustor during operation at Mach 5-equivalent flight speed in a flow facility at AFRL [54,55].

These demonstration measurements were conducted in collaboration with Dr. Campbell Carter and Dr. Mark Gruber at the AFRL at Wright-Patterson AFB, OH. These collaborative measurements showed a factor-of-four increase in SNR with WMS for measurements of weakly-absorbing CO_2 in the supersonic flow compared to direct absorption measurements (for signals with significant absorbance). The WMS measurements of temperature and H_2O were compared to two-dimensional computational fluid-dynamics (CFD) calculations using a new scheme that accounts for the influence of line-of-sight (LOS) non-uniformity on the absorption measurements. These comparisons showed the ability of the LOS technique for validation of multi-dimensional CFD simulations [54]. In addition, fluctuations in temperature nonuniformity along the laser LOS were found to increase significantly prior to backpressure-induced unstart [55]. Though the precise cause of the fluctuations remains unknown, the detection method showed promise for use in control schemes to avoid back pressure-induced unstart in scramjets. Overall, these demonstrations showed that accurate, non-intrusive, high-bandwidth measurements could be made in harsh propulsion test stand environments using the calibration-free WMS technique.

2.7.1 Calibration-Free $1f$ -normalized WMS- $2f$ Sensors

The calibration-free WMS method studied in this AFOSR program is applicable to any WMS light source that exhibits synchronous wavelength and intensity modulation. In 1982, Cassidy and Reid [28] first recognized that injection-current-tuned diode lasers provide a $1f$ signal that can be used to normalize the $2f$ signal from optically thin absorption and that this normalization accounts for any non-absorption variations in laser intensity. During the last grant period, our AFOSR-sponsored research found that combining this intensity normalization with a model for the WMS signals based on the specific laser tuning characteristics for the probe laser and a spectral database for the

target transitions can eliminate all calibration factors between the experiment and model [56]. Thus, the experiment and model can be compared directly without *in situ* calibration. As discussed in section 2.5, this method works at any pressure where a $2f$ signal can be obtained and the absorption spectrum is well known. The method does not require that the laser scan across the entire feature –only the $2f$ peak must be captured – which is helpful at high pressures (as seen in section 2.5 of this report). The method does have intricacies, such as different optimal implementations depending on the environment and conditions, and drawbacks, such as the need for knowledge of the gas pressure in the probe region [53].

WMS- $2f$ has several benefits that make it desirable over direct absorption for certain sensing applications. Generally the second harmonic ($2f$) is used because, like direct absorption, the $2f$ signal is dependent strongly on spectral parameters and gas properties and therefore can be compared with spectral simulations to infer gas properties.

The $2f$ signal is sensitive to spectral shape or curvature rather than absolute absorption levels, which is useful for certain high-density spectra [see section 2.5 above], particularly those that are affected by broadband absorption or emission. Also, the use of a lock-in amplifier serves to reject noise that falls outside of the lock-in pass band.

For laser sources that have synchronous tuning of the laser wavelength and intensity (such as diode lasers), the intensity modulation is typically the strongest component of the first harmonic ($1f$) signal, and can be used to normalize the $2f$ signal against perturbations to the laser intensity by laser drift, window fouling, beam steering, or scattering. This attribute of WMS is particularly useful in harsh environments and is demonstrated in a laboratory equipment. Fig. 2.7.1 shows the simple setup where a laser was tuned to an absorption feature of H_2O in ambient laboratory air. The $2f$ and $1f$ signals were recorded as the laser beam was blocked partially (left panel of Fig. 2.7.2), and the laser optics were vibrated periodically (right panel of Fig. 2.7.2). Despite the large and rapid changes in the laser intensity (which affect both the $2f$ and $1f$ signals), the $1f$ -normalized, WMS- $2f$ signal remained unchanged in the left and right panels of Fig. 2.7.2, illustrating the usefulness of $1f$ -normalization of WMS- $2f$ for harsh environments with non-absorbing losses in the transmitted laser intensity.

The WMS model was developed during the previous AFOSR grant period and has been verified by a wide range of experiments (most recently, those described in sections 2.4 and 2.5 above). This model extends the work of many researchers to be compatible with phase-insensitive lock-in detection and to include laser-specific tuning characteristics. During this past AFOSR grant period, the model was extended further to be compatible with any optical depth [53] (the earlier work assumed an optically thin medium). The incident laser intensity is represented by:

$$I_0(t) = \bar{I}_0 [1 + i_1 \cos(\omega t + \psi_1) + i_2 \cos(2\omega t + \psi_2)] \quad (2.7.1)$$

where \bar{I}_0 is the mean laser intensity at line center, i_1 and i_2 are the amplitudes of the linear and first term of the nonlinear laser intensity modulation (normalized by \bar{I}_0), and ψ_1 and ψ_2 are the phase shifts between the laser intensity modulation and laser frequency (wavelength) modulation for linear and nonlinear intensity modulation, respectively. These parameters, i_0 , i_2 , ψ_1 , and ψ_2 , are laser specific and must be characterized in the



Figure 2.7.1 Schematic shows the transmission of laser light in laboratory air with the laser tuned to line center of the absorption of ambient water vapor.

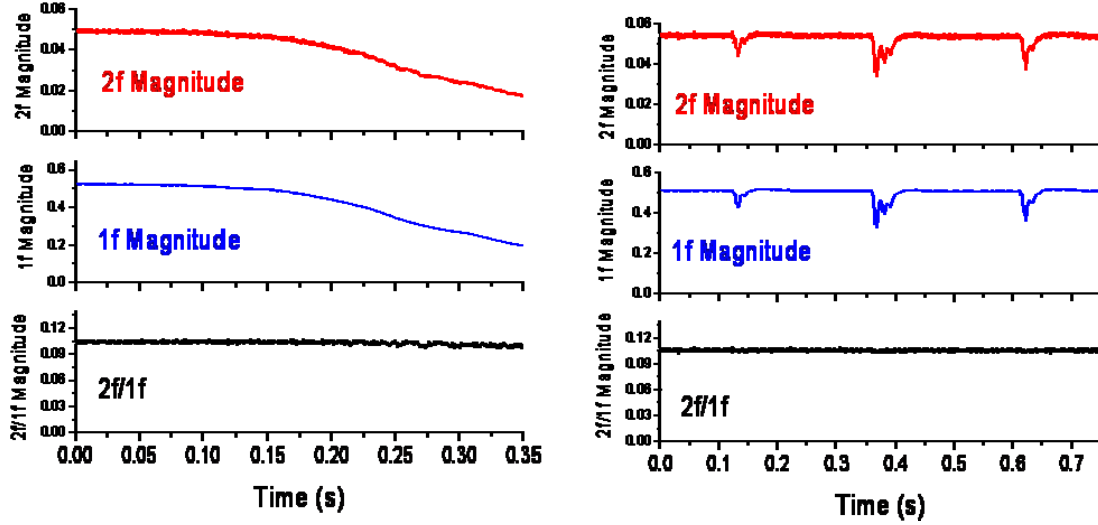


Figure 2.7.2 The laser wavelength from Fig. 2.7.1 was modulated at frequency f , and the $2f$ and $1f$ components of the detector signal were extracted with lock-in amplifiers. The $1f$ normalized $2f$ signal was immune to non-absorption losses in the transmitted laser intensity.

laboratory for the specific operation settings (injection current, modulation frequency, etc.) that are to be used for the measurements. Absorption is simulated by defining a transmission coefficient for the laser light through the absorbing medium (which depends on the laser frequency (wavelength)) in terms of a Fourier series:

$$\tau(\nu(t)) = \sum_{k=0}^{k=+\infty} H_k(\bar{\nu}, a) \cos(k\omega t) \quad (2.7.2)$$

where $\nu(t) = \bar{\nu} + a \cos(\omega t)$ is the instantaneous laser frequency (wavelength), $\bar{\nu}$ is the average laser frequency (wavelength), and a is the amplitude of the frequency (wavelength) modulation. The parameters $\bar{\nu}$ and a also must be measured for the specific laser and laser operation procedures used for the measurements. Combining this with the Beer-Lambert relation, the H terms can be defined as:

$$H_0(T, P_i, \bar{\nu}, a) = \frac{1}{2\pi} \int_{-\pi}^{\pi} \exp \left\{ - \sum_j S_j(T) \cdot \phi_j(T, P, x, \bar{\nu} + a \cos \theta) \cdot P \cdot x_i \cdot L \right\} d\theta \quad (2.7.3)$$

$$H_k(T, P_i, \bar{\nu}, a) = \frac{1}{\pi} \int_{-\pi}^{\pi} \exp \left\{ - \sum_j S_j(T) \cdot \phi_j(T, P, x, \bar{\nu} + a \cos \theta) \cdot P \cdot x_i \cdot L \right\} \cos k\theta d\theta \quad (2.7.4)$$

Where $S_j(T)$ is the linestrength at temperature T of absorption transition j , P is the total pressure, x_i is the mole fraction of the absorbing species i , L is the pathlength of laser beam travel through the absorbing medium, and ϕ_j is the line shape function of transition j . Depending on the experimental conditions, the line shape function can be modeled with a Gaussian, Voigt, or Lorentzian profile using broadening parameters that are known either through careful laboratory measurements or from HITRAN [26]. The line strength also must be known in order to calculate the H terms.

The detector signal then is modeled by multiplying the incident laser intensity (Eq. 2.7.1) with the first few terms of the transmission function (Eq. 2.7.2). To simulate the X and Y components of the phase-insensitive lock-ins tuned to measure the $2f$ signal, the detector signal is multiplied by $\cos(2\omega t)$ and $\sin(2\omega t)$, respectively. Only DC terms are carried after the multiplication to simulate the effect of the low-pass filtering step of the lock-in:

$$X_{2f} = \frac{G\bar{I}_o}{2} \left(H_2 + \frac{i_o}{2} (H_1 + H_3) \cos \psi_1 + i_2 \left(H_o + \frac{H_4}{2} \right) \cos \psi_2 \right) \quad (2.7.5)$$

$$Y_{2f} = -\frac{G\bar{I}_o}{2} \left(\frac{i_o}{2} (H_1 - H_3) \sin \psi_1 + i_2 \left(H_o - \frac{H_4}{2} \right) \sin \psi_2 \right), \quad (2.7.6)$$

where G is the electro-optical gain of the detection system, which does not need to be known or measured since normalization with the $1f$ signal in the next step cancels this term.

Using the same method but changing the lock-in reference signals to $\cos(\omega t)$ and $\sin(\omega t)$, the components of the $1f$ signal can be calculated:

$$X_{1f} = \frac{G\bar{I}_o}{2} \left(H_1 + i_o \left(H_o + \frac{H_2}{2} \right) \cos \psi_1 + \frac{i_2}{2} (H_1 + H_3) \cos \psi_2 \right) \quad (2.7.7)$$

$$Y_{1f} = -\frac{G\bar{I}_o}{2} \left(i_o \left(H_o - \frac{H_2}{2} \right) \sin \psi_1 + \frac{i_2}{2} (H_1 - H_3) \sin \psi_2 \right) \quad (2.7.8)$$

The $1f$ magnitude is then calculated using the root-sum-square: $R_{1f} = \sqrt{X_{1f}^2 + Y_{1f}^2}$.

The WMS $1f$ and $2f$ signals now can be calculated using the measured laser specific tuning characteristics and the transition specific spectral parameters for the target absorption feature.

2.7.2 Sensor Used for AFRL Scramjet Measurements

Wavelength-multiplexing several lasers targeted at multiple transitions of the same species with differing internal energy (E'') can provide good temperature sensitivity over a wide range of conditions and the ability to extract information about temperature and species non-uniformity along the laser line-of sight (LOS). For the most recent AFRL measurement campaign we used a six-laser sensor for H_2O and CO_2 based on a hybrid demultiplexing scheme using wavelength and frequency. Wavelength-multiplexed systems combine all of the laser wavelengths into a single beam and a grating located

after the light passes through the measurement region was used to separate each wavelength spatially onto a separate detectors. This method provided simultaneous measurements of multiple parameters; however, this method introduced a requirement that the laser wavelengths have sufficient spectral separation for successful spatial separation by the grating. This constraint became important in harsh high-speed flows, where there was significant beam steering by flow eddies of varying density. Thus, large area detectors were used to minimize this noise at the expense of requiring large spatial separation of wavelength demultiplexed beams. WMS offers the possibility of frequency demultiplexing, where each laser is modulated with a different frequency and the lock-in amplifiers separate the $2f$ and $1f$ signals of each laser from the same detector signal, based on the modulation frequency; however, the number of lasers that can be demultiplexed in this method is somewhat limited by the temporal resolution bandwidth.

For the AFRL scramjet measurements, a hybrid demultiplexing approach was used, in which wavelength and frequency demultiplexing were combined to separate six laser signals using four detectors, as illustrated in Fig. 2.7.3. Five lasers tuned to H_2O absorption features ranging from 1338 nm to 1469 nm and one laser tuned to a CO_2 transition near 1997 nm were combined onto a single mode optical fiber (Corning SMF-28). The wavelength multiplexed beam was delivered to the scramjet test section on a 10 m fiber. Then the beam was collimated with an uncoated aspheric lens, directed across the scramjet flow just downstream of the model combustor, collected with a large diameter lens, and focused into a multimode fiber with a 600 micron core. The beam traveled through the multimode fiber to the hybrid demultiplexing setup a few meters from the test section, where it was collimated by a large diameter aspheric lens onto a 600 grooves/mm diffraction grating. The dispersed wavelength groups were focused onto four 3 mm diameter InGaAs photodetectors (1997 and 1469 nm lasers used individual detectors, while the 1338/1343 nm pair and the 1388/1392 nm pair each shared a detector). The laser pairs were modulated at 160 kHz and 200 kHz to allow them to be

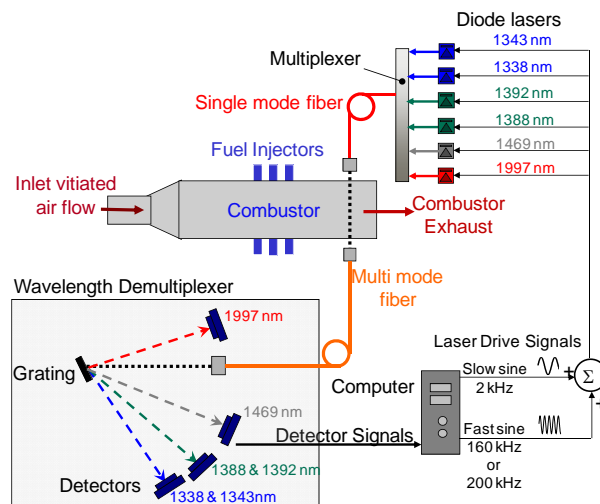


Figure 2.7.3 Schematic of hybrid demultiplexing system configured for the scramjet experiments at AFRL/WPAFB [54,55].

frequency-demultiplexed. Water vapor measurements were made on 5 transitions with a large variety of lower state energies: near 6807.8 cm^{-1} ($E''=3319\text{ cm}^{-1}$), 7185.6 cm^{-1} ($E''=1045\text{ cm}^{-1}$), 7205.2 cm^{-1} ($E''=79\text{ cm}^{-1}$), 7444.4 cm^{-1} ($E''=1790\text{ cm}^{-1}$), and 7472.2 cm^{-1} ($E''=2952\text{ cm}^{-1}$). These transitions covered a wide range of E'' , $79 < E'' < 3319\text{ cm}^{-1}$, thus providing the potential to explore the temperature uniformity over the sensor LOS.

2.7.3 CO₂/H₂O Concentration in a Vitiated Supersonic Flow

The sensor system described in Section 3 was used for measurements in the direct-connect, ground test scramjet combustor at AFRL/WPAFB to measure temperature and H₂O and CO₂ concentrations under a variety of operating conditions. These were the first TDL absorption measurements of CO₂ in a supersonic flow and the flow from the vitiated air heater passing through the combustor duct was used to validate sensor performance. The vitiator used fuel-lean combustion of methane and air upstream of the expansion nozzle prior to the isolator of the scramjet test section. The vitiator increased the incoming air temperature to ensure that the proper scramjet inlet conditions were met when the supersonic flow was generated in the expansion nozzle. The lean methane/air mixture produces a well known H₂O/CO₂ ratio and provides a convenient test of the new CO₂ sensor.

The laser beam passed across the supersonic flow downstream of the scramjet combustor flameholders in an expanding section of the duct. The approximate static pressure at the measurement location for the vitiator-only condition was 0.26 atm with a static temperature around 600 K. The sensor was tested using both direct absorption and calibration-free WMS to probe absorption on the R50 transition of the 20012 \leftarrow 00001 band of CO₂ near 5007.8 cm^{-1} . This transition is relatively free of water vapor interference and has a lower-state energy (E'') of 994 cm^{-1} , which makes it suitable for measurements in this temperature range. The water vapor feature near 7185.6 cm^{-1} ($E''=1045\text{ cm}^{-1}$) was used for the water vapor measurements in this temperature range.

Figure 2.7.4 shows representative results of the H₂O and CO₂ measurements. The left panels show a single-scan of CO₂ absorption using (a) $2f$ and (b) direct absorption on consecutive runs of the scramjet test rig. The WMS signal appeared smooth compared to the direct absorption because the lock-in amplifier rejects $1/f$ laser noise and electronic noise. Only the peak of the feature was scanned, and the line shape appeared distorted near the beginning and end of the scan due to the sinusoidal scan waveform used (instead of a linear ramp). Also shown are the $2f$ peak value and the Voigt fit. The $2f$ peak value and the integrated absorbance extracted from the Voigt fit were used to infer the CO₂ concentration with the WMS and direct absorption methods, respectively. The right panels show the measured concentrations in terms of partial pressures for a 0.2s time period using both of these methods at a measurement rate of 4 kHz.

The SNR was calculated from the partial pressure data and was defined as the ratio of the mean partial pressure divided by the standard deviation. The SNR of the calibration-free WMS measurement (13.2) was 4x better than the direct absorption measurement (3.2). From the single scan data shown in the left panel one might expect the difference in SNR to be even larger, however the SNR of the direct absorption measurement benefitted from the use of a Voigt fit while the WMS relies on a single point at the line center of the transition. The SNR obtained with the WMS measurements was excellent considering

the low CO₂ absorbance levels (<2%) and the supersonic nature of the flow. The measured H₂O/CO₂ ratio using calibration-free WMS is 1.99, which was within 0.5% of the expected value of 2.00 for the methane-air vitiated heater. Taken together, these results confirm the SNR benefits of WMS and show that accurate results can be obtained with WMS without *in situ* calibration.

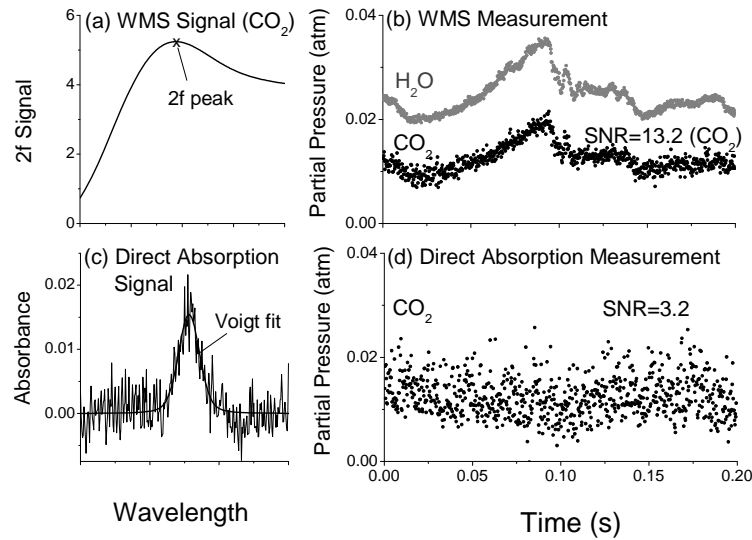


Figure 2.7.4 Comparison of direct absorption and $2f$ signals and CO₂ partial pressure measurements in a vitiated supersonic flow using the 1997 nm absorption feature of CO₂. The left panels show single-scan data with (a) the WMS- $2f$ and (c) direct absorption techniques, along with the peak or voigt fit values that are used to calculate the CO₂ concentration. The right panels show the measured CO₂ partial pressure at 4 kHz using (b) $2f$ peak magnitudes and (d) integrated absorbance [54].

2.7.4 Comparison of TDL LOS Measurements with 2D CFD

Laser absorption is a path integrated LOS technique and is interpreted most easily for uniform gas composition and temperature on the sensor LOS; however, practical systems have boundary layers and other flow field non-uniformities. Therefore, sensor measurements are desired that can determine the non-uniformities on the LOS and that can be used to validate 2D CFD simulations. We combined our WMS model with the CFD calculations to predict an expected two-line TDL absorption temperature that can be compared with the TDL measurements. At each point along the LOS the CFD values of concentration, pressure, and temperature are used to simulate the two-line WMS signals and inferred temperature. In this way, the effect of any non-uniformity on the nonlinear absorption response of the probed spectral features will be included in both the measurement and the CFD-calculated expected temperature.

An example result is shown in Fig. 2.7.5 for measurements and CFD calculations for the scramjet combustor at AFRL/WPAFB for ethylene and air at a fuel/air stoichiometry, $\phi=0.7$. The laser-measured temperature and H₂O partial pressure were inferred from calibration-free I_f -normalized WMS- $2f$ using the 6807.8 cm⁻¹ ($E''=3319$ cm⁻¹) and 7185.6 cm⁻¹ ($E''=1045$ cm⁻¹) transitions at nine vertical locations in the combustor duct (represented by the solid squares). The expected laser-measured values based on 2D

CFD calculations of the flow field are represented by the open circles. Figure 2.7.5 also shows the regular path-averaged temperature based on the 2D CFD (gray line, no symbols). Though the expected laser-measured temperature was different than the path-averaged temperature, the trends were retained and showed that information about the path-averaged temperature could be gained from the laser-measured temperature.

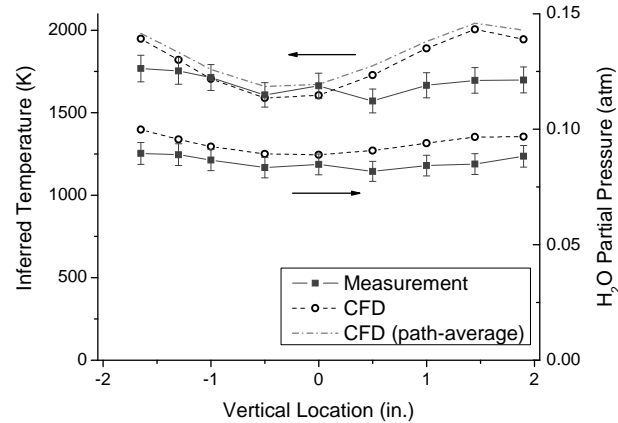


Figure 2.7.5 Static temperature and H₂O partial pressure for different vertical locations in the scramjet combustor during full operation on ethylene and air. Each point is the LOS laser-measured value for the experiment (solid squares) and the expected LOS laser-measured value from the CFD calculated flow field (open circles). The gray line (no symbols) represents the path-average temperature from the CFD calculated flow field.

By considering data from multiple vertical locations, information about the non-uniform gas properties in the combustor could be inferred. For example, the temperature from the sensor measurement and the CFD agreed well in the core flow region (within 4%). The measurements also indicated a lower measured temperature than expected near the top and bottom walls of the combustor. These results suggested that the heat loss or turbulence models used in the CFD may be under-predicting mass and energy transport. The H₂O partial pressure measurements in the actual combustor were ~5-12% lower than predicted by the CFD, which may indicate that the OH to H₂O conversion rate was overpredicted by CFD or that the combustion was not complete (although separately measured thrust suggested complete combustion).

2.7.5 Fluctuations in Temperature Non-Uniformity Predict Unstart

The 4kHz time resolution of the TDL sensor offered the potential of correlating combustor instabilities with fluctuations in the sensor measurements of gas properties. Temperature non-uniformity was monitored by ratios of two pairs of absorption transitions. When the temperature along the sensor LOS is not uniform, the contribution to the path integrated absorbance for a low E'' line is dominated by the colder regions along the path, and similarly the contribution to the absorbance on a high E'' line is dominated by the hotter regions along the path; therefore, if we chose a pair of relatively high E'' lines, the two-line absorption temperature will discriminate against the low temperature regions, and the temperature even may exceed the average temperature. Whereas a pair of relatively low E'' lines will discriminate against the high temperature regions and their ratio will indicate a temperature less than the average value. The ratio

of the two-line temperatures from a high and low E'' pair provided a measure of the temperature non-uniformity. Although it was difficult to quantify this non-uniformity, fluctuations in the ratio of two line temperatures were a good measure of fluctuation in temperature non-uniformity. For example, if the boundary layer of the flow was colder (or hotter) than the core flow, fluctuations of the temperature non-uniformity given by the ratio of the high and low E'' two line temperatures provided a good measure of fluctuations in the boundary layer. We exploited the multi-line temperature sensor shown in Fig. 2.7.3 to monitor fluctuations in the temperature non-uniformity. The two line ratio of the absorbance of 7444.4 cm^{-1} ($E''=1790\text{ cm}^{-1}$) and 7472.2 cm^{-1} ($E''=2952\text{ cm}^{-1}$) provided the time-resolved high temperature sensor $[T_{\text{high}}(t)]$, and the ratio 7185.6 cm^{-1} ($E''=1045\text{ cm}^{-1}$) and 7205.2 cm^{-1} ($E''=79\text{ cm}^{-1}$) provided $T_{\text{low}}(t)$. The short-time Fourier transforms (STFTs) of $T_{\text{high}}(t)/T_{\text{low}}(t)$ were used to monitor these fluctuations in temperature non-uniformity [55].

The diode laser sensor was used to monitor 99 combustor runs of the scramjet test rig, and an unstable case in which unstart occurred was compared with a representative stable case to demonstrate the utility of the fluctuation monitoring. All operating parameters for the scramjet were identical for the two cases shown except the overall fuel/air equivalence ratio, which was $\phi \approx 0.7$ for the stable case and $\phi \approx 0.85$ for the unstable case.

The average gas temperature was measured with multiple absorption feature ratios for the stable and unstable combustor conditions. Both type experiments began at $t=0$ with only vitiated air at $\sim 575\text{ K}$ passing the measurement location, and combustor fuel injection began at approximately $t=24\text{ s}$. No ignition source was used for these measurements, so the autoignition and flame stabilization process occurred for 6-7 seconds as the flame developed across the combustor and approached steady-state. Gas temperatures appeared to plateau for several seconds when a sudden blowout/re-ignition event occurred for the unstable $\phi \approx 0.85$ case. After this event the average gas temperature at the measurement location was reduced for the $\phi \approx 0.85$ case.

The ratio between the fractional STFTs of $T_{\text{high}}(t)/T_{\text{low}}(t)$ is plotted in Fig. 2.7.6, as the ratio distinguish between the ignition transients (common to $T_{\text{high}}(t)$ and $T_{\text{low}}(t)$) and the fluctuations preceding unstart,. The data showed a strong increase in the low-frequency fluctuations in the temperature non-uniformity $\sim 4.8\text{ s}$ before the unstart event. This phenomenon was recorded for all cases that experienced unstart, with varying initiation times up to 10s before the unstart event. The blowout/re-ignition event was not always present. These data were correlated with the isolator pressure history for the unstable combustor runs to confirm that the observed phenomena were a back pressure-induced unstart. The scramjet flowpath contains 248 pressure taps that record the unstart by tracking the location of the isolator shock train.

It is unclear presently what physical processes caused the increase in low-frequency fluctuations of the temperature non-uniformity prior to unstart. Isolator boundary layer growth and separation are associated with unstart, as well as several potential instabilities for transverse fuel jets at increased heat-addition rates. Interactions between the combustor and isolator also are likely to occur but have not been studied. Overall, the likelihood is high for large-scale flow-instabilities to exist during the unstart process. Because the increase in low-frequency fluctuations began in advance of unstart, one can see the potential utility of the ratio of fractional STFT information from two absorption

line pairs as a control variable. The variable could be used to limit fuel flow to the combustor or modify the distribution of fuel among a series of injection sites at the onset of fluctuations and thereby avoid a back pressure-induced unstart.

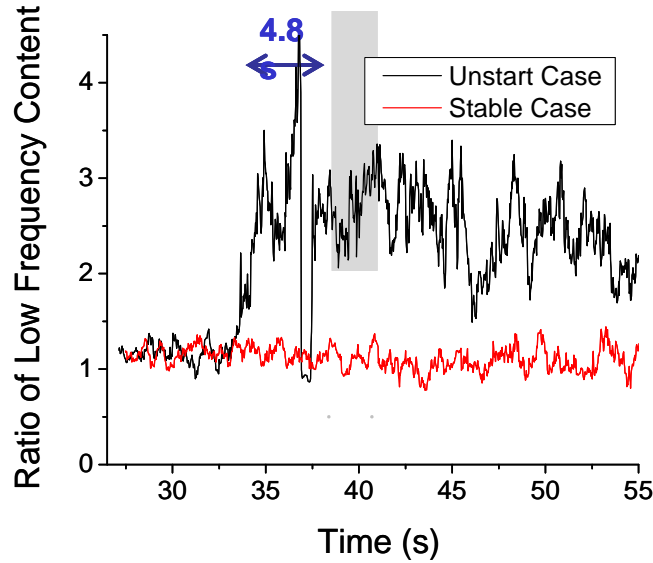


Figure 2.7.6 Low-frequency fluctuations in temperature non-uniformity (see text) versus time for a typical stable combustor trial and a combustor trial where unstart was observed. A large increase in the low-frequency fluctuations precedes the occurrence of pressure induced inlet unstart [55].

2.8 References

- [1] C. Schulz and V. Sick, "Tracer-LIF diagnostics: quantitative measurement of fuel concentration, temperature and fuel/air ratio in practical combustion systems," *Progress in Energy and Combustion Science* **31** (2005), 75-121.
- [2] J. D. Koch, *Fuel tracer photophysics for quantitative planar laser-induced fluorescence*, Stanford University, PhD thesis (2005); available from <http://thermosciences.stanford.edu/pdf/TSD-159.pdf>.
- [3] V. Modica, C. Morin and P. Guibert, "3-Pentanone LIF at elevated temperatures and pressures: measurements and modeling," *Applied Physics B* **87** (2007), 193-204.
- [4] A. Braeuer, F. Beyrau and A. Leipertz, "Laser-induced fluorescence of ketones at elevated temperatures for pressure up to 20 bars by using a 248 nm excitation laser wavelength: experiments and model improvements," *Applied Optics* **45** (2006), 4982-9.
- [5] J. Koch, J. Gronki and R. K. Hanson, "Measurements of near-UV absorption spectra of acetone and 3-pentanone at high temperatures," *Journal of Quantitative Spectroscopy and Radiative Transfer* **109** (2008), 2037-2044.
- [6] J. D. Koch, R. K. Hanson, W. Koban and C. Schulz, "Rayleigh-calibrated fluorescence quantum yield measurements of acetone and 3-pentanone," *Applied Optics* **43** (2004), 5901-10.
- [7] J. Koch and R. K. Hanson, "A photophysics model for 3-pentanone wavelengths dependencies: temperature, pressure, and excitation wavelength dependencies," *AIAA* 2003-403 (2003).
- [8] C. M. Fajardo, J. D. Smith and V. Sick, "Sustained simultaneous high-speed imaging of scalar and velocity fields using a single laser," *Applied Physics B* **85** (2006), 25-31.
- [9] C. F. Kaminski, J. Hult and M. Alden, "Rapid Communication: High repetition rate planar laser induced fluorescence of OH in a turbulent non-premixed flame," *Applied Physics B* **68** (1999), 757-760.
- [10] A. Y. Chang, B. E. Battles and R. K. Hanson, "Simultaneous measurements of velocity, temperature, and pressure using rapid cw wavelength-modulation laser-induced fluorescence of OH," *Optics Letters* **15** (1990), 706-708.
- [11] M. D. DiRosa, A. Y. Chang and R. K. Hanson, "Continuous wave dye-laser technique for simultaneous, spatially resolved measurements of temperature, pressure, and velocity of NO in an underexpanded free jet," *Applied Optics* **32** (1993), 4074-4087.
- [12] B. H. Cheung and R. K. Hanson, "CW laser-induced fluorescence of toluene for time-resolved imaging of gaseous flows," *Applied Physics B* **98** (2010), 581-591.
- [13] B. K. McMillin, M. P. Lee, and R. K. Hanson, "Planar laser-induced fluorescence imaging of shock-tube flows with vibrational nonequilibrium," *AIAA*, **30** (1992), 436-443.
- [14] A. Lozano, B. Yip, and R. K. Hanson, "Acetone: a tracer for concentration measurements in gaseous flows by planar laser-induced fluorescence," *Experiments in Fluids* **13** (1992), 369-376.

-
- [15] J. M. Seitzman, G. Kychakoff, and R. K. Hanson, "Instantaneous temperature field measurement using planar laser-induced fluorescence," *Optics Letters*, **10** (1985), 439-441
 - [16] H. Neij, B. Johansson, and M. Alden, "Development and demonstration of 2D-LIF for studies of mixture preparation in SI engines," *Combustion and Flame*, **99** (1994), 449-457.
 - [17] M. Luong, W. Koban, and C. Schulz, "Novel strategies for imaging temperature distribution using toluene LIF," *Journal of Physics: Conference series*, **45** (2006), 133-139.
 - [18] D. Frieden, V. Sick, J. Gronki, and C. Schulz, "Quantitative oxygen imaging in an engine," *Applied Physics B*, **75** (2002), 137-141.
 - [19] W. Koban, J. D. Koch, R. K. Hanson, and C. Schulz, "Absorption and fluorescence of toluene vapor at elevated temperatures," *Physical Chemistry Chemical Physics*, **6** (2004), 2940-2945.
 - [20] A. E. Klingbeil, J. B. Jeffries, and R. K. Hanson, "Temperature-dependent mid-IR absorption spectra of gaseous hydrocarbons," *Journal of Quantitative Spectroscopy & Radiative Transfer*, **107** (2007), 407-420.
 - [21] F. R. Menter, "Two-equation eddy-viscosity turbulence models for engineering application," *AIAA Journal*, **32** (1994), 1598-1605.
 - [22] A. Farooq, J. B. Jeffries and R. K. Hanson, "In situ combustion measurements of H₂O and temperature near 2.5 μ m using tunable diode laser absorption," *Measurement Science and Technology* **19** (2008), 075604.
 - [23] A. Farooq, J. B. Jeffries and R. K. Hanson, "CO₂ concentration and temperature sensor for combustion gases using diode-laser absorption near 2.7 μ m," *Applied Physics B: Lasers and Optics* **90** (2008), 619-628.
 - [24] A. Farooq, J. B. Jeffries and R. K. Hanson, "Sensitive detection of temperature behind reflected shock waves using wavelength modulation spectroscopy of CO₂ near 2.7 μ m," *Applied Physics B: Lasers and Optics* **96** (2009), 161-173.
 - [25] X. Zhou, X. Liu, J. B. Jeffries and R. K. Hanson, "Development of a sensor for temperature and water concentration in combustion gases using a single tunable diode laser," *Measurement Science and Technology* **14** (2003), 1459-1468.
 - [26] L. S. Rothman, I. E. Gordon, A. Barbe, D. C. Benner, P. F. Bernath and M. Birk, "The HITRAN 2008 molecular spectroscopic database," *Journal of Quantitative Spectroscopy and Radiative Transfer* **110** (2009), 533-72.
 - [27] J. Reid and D. Labrie, "Second-harmonic detection with tunable diode lasers — Comparison of experiment and theory," *Applied Physics B: Lasers and Optics* **26** (1981), 203-210.
 - [28] D. T. Cassidy and J. Reid, "Atmospheric pressure monitoring of trace gases using tunable diode lasers," *Applied Optics* **21** (1982), 1185-1190.
 - [29] H. Li, G. B. Rieker, X. Liu, J. B. Jeffries and R. K. Hanson, "Extension of wavelength-modulation spectroscopy to large modulation depth for diode laser absorption measurements in high-pressure gases," *Applied Optics* **45** (2006), 1052-1061.

-
- [30] Z. Hong, G. Pang, S. Vasu, D. Davidson and R. Hanson, "The use of driver inserts to reduce non-ideal pressure variations behind reflected shock waves," *Shock Waves* **19** (2009), 113-123.
 - [31] E. D. B. Sirjean, D. A. Sheen, X.-Q. You, C. Sung, A. T. Holley, F. N. Egolfopoulos, H. Wang, S. S. Vasu, D. F. Davidson, R. K. Hanson, H. Pitsch, C. T. Bowman, A. Kelley, C. K. Law, W. Tsang, N. P. Cernansky, D. L. Miller, A. Violi, R. P. Lindstedt, "A high-temperature chemical kinetic model of n-alkane oxidation, JetSurF version 0.2," http://melchior.usc.edu/JetSurF/Version0_2/Index.html (2008).
 - [32] H. Li, Z. C. Owens, D. F. Davidson and R. K. Hanson, "A simple reactive gasdynamic model for the computation of gas temperature and species concentrations behind reflected shock waves," *International Journal of Chemical Kinetics* **40** (2007), 189 - 198.
 - [33] A. Farooq, J. B. Jeffries and R. K. Hanson, "Measurements of CO₂ concentration and temperature at high pressures using 1f-normalized wavelength modulation spectroscopy with second harmonic detection near 2.7 μm ," *Applied Optics* **48** (2009), 6740-6753.
 - [34] A. Farooq, J. B. Jeffries and R. K. Hanson, "High-pressure measurements of CO₂ absorption near 2.7 μm : Line mixing and finite duration collision effects," *Journal of Quantitative Spectroscopy and Radiative Transfer* **111** (2010), 949-960.
 - [35] C.K. Westbrook, W. J. Pitz, O. Herbinet, H. J. Curran, and E. J. Silke, "A Detailed chemical kinetic reaction mechanism for n-alkane hydrocarbons from n-octane to n-hexadecane," *Combustion Flame* **156** (2009) 181-199.
 - [36] H. Seiser, H. Pitsch, K. Seshadri, W. J. Pitz, H. J. Curran, "Extinction and autoignition of n-heptane in counterflow configuration," *Proceedings of the Combustion Institute* **28** (2000), 2029-2037.
 - [37] M. Y. Perrin and J. M. Hartmann, "Temperature-dependent measurements and modeling of absorption by CO₂-N₂ mixtures in the far line-wings of the 4.3 μm CO₂ band," *Journal of Quantitative Spectroscopy and Radiative Transfer* **42** (1989), 311-317.
 - [38] F. Niro, C. Boulet and J. M. Hartmann, "Spectra calculations in central and wing regions of CO₂ IR bands between 10 and 20 μm . I: model and laboratory measurements," *Journal of Quantitative Spectroscopy and Radiative Transfer* **88** (2004), 483-498.
 - [39] Adam E. Klingbeil, *Mid-IR laser absorption diagnostics for hydrocarbon vapor sensing in harsh environments*, Stanford University, PhD thesis (2007) available from: <http://thermosciences.stanford.edu/pdf/TSD-175.pdf>.
 - [40] Jason Porter, *Laser-based diagnostics for hydrocarbon fuels in the liquid and vapor phases*, Stanford University, PhD thesis (2009) available from: <http://thermosciences.stanford.edu/pdf/TSD-182.pdf>
 - [41] A.E. Klingbeil, J.B. Jeffries, D.F. Davidson, R.K. Hanson, "Two-wavelength mid-IR diagnostic for temperature and n-dodecane concentration in an aerosol shock tube," *Applied Physics B* **93** (2008) 627-638.
 - [42] A.E. Klingbeil, J.M. Porter, J.B. Jeffries, R.K. Hanson, "Two-wavelength mid-IR absorption diagnostic for simultaneous measurement of temperature and

-
- hydrocarbon fuel concentration,” *Proceedings of the Combustion Institute* **32** (2009) 821-829.
- [43] J.M. Porter, J.B. Jeffries, R.K. Hanson, “Mid-infrared laser-absorption diagnostic for vapor-phase measurements in an evaporating n-decane aerosol,” *Applied Physics B*, **97** (2009) 215-225.
- [44] J.M. Porter, J.B. Jeffries and R.K. Hanson, “Mid-infrared laser-absorption diagnostic for vapor-phase fuel mole fraction and liquid film thickness,” *Applied Physics B*, submitted October, 2009.
- [45] A.E. Klingbeil, J.B. Jeffries, and R.K. Hanson, “Temperature-dependent mid-IR absorption spectra of gaseous hydrocarbons” *Journal Quantitative Spectroscopy and Radiative Transfer* **107** (2007) 407-420.
- [46] J.M. Porter, J.B. Jeffries and R.K. Hanson, “Mid-infrared absorption measurements of liquid hydrocarbon fuels near 3.4 μm ,” *Journal Quantitative Spectroscopy and Radiative Transfer* **110** (2009) 2135-2147.
- [47] M. Chaos, A. Kazakov, Z.W. Zhao, F.L. Dryer, *Interntional Journal Chemical Kinetics* **39** (7) (2007) 399–414.
- [48] M. Colket, et al., “Development of an experimental database and kinetic models for surrogate jet fuels,” AIAA 2007-770.
- [49] S.S. Vasu, D.F. Davidson, Z. Hong, V. Vasudevan, R.K. Hanson, “n-Dodecane oxidation at high-pressures: measurements of ignition delay times and OH concentration time-histories,” *Proceedings of the Combustion Institute* **32** (2009) 173-180.
- [50] D. R. Haylett, D. F. Davidson, R. K. Hanson, “A second generation aerosol shock tube and its application to combustion research,” AIAA-2010-0196.
- [51] M. C. Drake, T. D. Fansler, A. S. Solomon, J. Gerald A. Szekely, “Piston fuel films as a source of smoke and hydrocarbon emissions from a wall-controlled spark-ignited direct- injection engine,” *SAE 2003 World Congress and Exhibition*, Detroit, MI, USA, 2003, 2003-01-0547.
- [52] C.F. Bohren, D.R. Huffman, *Absorption and Scattering of Light by Small Particles*, Wiley, New York (1998)
- [53] G.B. Rieker, J.B. Jeffries, R.K. Hanson, “Calibration-free wavelength modulation spectroscopy for measurements of gas temperature and concentration in harsh environments,” *Applied Optics* **48** (2009) 5546-5560.
- [54] M. Gruber, C. Carter, M. Ryan, G. B. Rieker, J. B. Jeffries, R. K. Hanson, J. Liu, T. Mathur, “Laser-based measurements of OH, temperature, and water vapor concentration in a hydrocarbon-fueled scramjet,” *44th AIAA/ASME/SAE/ASEE Joint Propulsion Conference & Exhibit*, 2008, AIAA 2008-5070.
- [55] G.B. Rieker, J.B. Jeffries, R.K. Hanson, T. Mathur, M.R. Gruber, and C.D. Carter, “Diode laser-based detection of combustor instabilities with application to a scramjet engine,” *Proceedings Combustion Institute* **32** (2009) 831-838.
- [56] H. Li, G.B. Rieker, X. Liu, J.B. Jeffries, and R.K. Hanson, “Extension of wavelength modulation spectroscopy to large modulation depth for diode laser absorption measurements in high-pressure gases,” *Applied Optics* **45** (2006) 1052-1061.

3 Publications and Presentations

The results of the AFOSR-sponsored research were published in thirty-six archival and AIAA papers, five PhD theses, and thirty-two presentations and invited lectures.

3.1 AFOSR Sponsored Publications

1. X. Liu, X. Zhou, J.B. Jeffries, and R.K. Hanson, "Experimental study of H₂O spectroscopic parameters in the near-IR (6940 - 7440 cm⁻¹) for gas sensing applications at elevated temperatures," *Journal Quantitative Spectroscopy and Radiative Transfer* **103**, 565-577 (2006).
2. A.E. Klingbeil, J.B. Jeffries, and R.K. Hanson, "Temperature- and pressure-dependent absorption cross-sections of gaseous hydrocarbons at 3.39μm," *Measurement Science and Technology* **17**, 1950-1957 (2006).
3. T. Lee, J.B. Jeffries, and R.K. Hanson, "Experimental evaluation strategies for quantitative laser-induced fluorescence imaging of nitric oxide in high-pressure flames," *Proceedings Combustion Institute* **31**, 757-764 (2007).
4. A.E. Klingbeil, J.B. Jeffries, and R.K. Hanson, "Tunable mid-IR laser absorption sensor for time-resolved hydrocarbon measurements," *Proceedings Combustion Institute* **31**, 807-815 (2007).
5. H. Li, X. Zhou, J.B. Jeffries, R.K. Hanson, "Active control of lean blowout in a swirl-stabilized combustor using a tunable diode laser," *Proceedings Combustion Institute* **31**, 3215-3223 (2007).
6. H. Li, X. Zhou, J.B. Jeffries, R.K. Hanson, "Sensing and control of combustion instabilities in swirl-stabilized combustors using diode-laser absorption," *AIAA Journal* **45**, 390-398 (2007).
7. X. Liu, J.B. Jeffries, R.K. Hanson, "Measurements of nonuniform temperature distributions using line-of-sight absorption spectroscopy," *AIAA Journal* **45**, 411-419 (2007).
8. A.E. Klingbeil, J.B. Jeffries, and R.K. Hanson, "Design of a fiber-coupled mid-IR fuel Sensor for pulse detonation engines," *AIAA Journal* **45**, 772-778 (2007).
9. G.B. Rieker, X. Liu, H. Li, J.B. Jeffries, R.K. Hanson, "Measurements of near-IR water vapor absorption at high pressure and temperature," *Applied Physics B* **87**, 169-178 (2007).
10. A.E. Klingbeil, J.B. Jeffries, and R.K. Hanson, "Temperature-dependent mid-IR absorption spectra of gaseous hydrocarbons" *Journal Quantitative Spectroscopy and Radiative Transfer* **107**, 407-420 (2007).
11. H. Li, A. Farooq, J.B. Jeffries, R.K. Hanson, "Near-infrared diode laser absorption sensor for rapid measurements of temperature and water vapor in a shock tube," *Applied Physics B* **89**, 407-416 (2007).
12. H. Li, A. Farooq, J.B. Jeffries, R.K. Hanson, "Diode laser measurements of temperature-dependent collisional narrowing and broadening parameters of Ar-

- perturbed H₂O transitions at 1391.7 and 1397.8 nm,” *Journal of Quantitative Spectroscopy and Radiative Transfer* **109**, 132-143 (2008).
13. H. Li, X. Zhou, J.B. Jeffries, and R.K. Hanson, “Sensing and control of combustion instabilities in swirl-stabilized combustors using a diode laser,” *42nd AIAA Joint Propulsion Conference*, Sacramento, CA, July 2006, AIAA-2006-4395.
 14. C. Cathey, F. Wang, T. Tang, A. Kuthi, M. Gundersen, J. Sinibaldi, C. Brophy, E. Barbour, R. Hanson, J. Hoke, F. Schauer, J. Corrigan, J. Yu, *45th AIAA Aerospace Sciences Meeting and Exhibit*, Reno, Nevada, 2007, AIAA-2007-443.
 15. A. Farooq, H. Li, J.B. Jeffries, and R.K. Hanson, “Measurements of CO₂ and H₂O near 2.7 μ m using tunable diode laser absorption,” *43rd AIAA Joint Propulsion Conference*, Cincinnati, OH, July 2007, AIAA 2007-5015.
 16. A. Farooq, J.B. Jeffries, R.K. Hanson, “CO₂ concentration and temperature sensor for combustion gases using diode-laser absorption near 2.7 μ m,” *Applied Physics B* **90**, 619-628 (2008).
 17. J.H. Yoo, T. Lee, J.B. Jeffries, R.K. Hanson, “Detection of trace NO concentrations using 1-D NO LIF imaging,” *Applied Physics B* **91**, 661-667 (2008).
 18. H. Li, A. Farooq, J.B. Jeffries, R.K. Hanson, “Diode laser measurements of temperature-dependent collisional narrowing and broadening parameters of Ar-perturbed H₂O transitions at 1391.7 and 1397.8 nm,” *Journal of Quantitative Spectroscopy and Radiative Transfer* **109**, 132-143 (2008).
 19. J.D. Koch, J. Gronki and R.K. Hanson, “Measurements of near-UV absorption spectra of acetone and 3-pentanone at high temperatures,” *J. Quantitative Spectroscopy and Radiative Transfer* **109**, 2037-2044 (2008).
 20. A.E. Klingbeil, J.B. Jeffries, D.F. Davidson, R.K. Hanson, “Two-wavelength mid-IR diagnostic for temperature and n-dodecane concentration in an aerosol shock tube,” *Applied Physics B* **93**, 627-638 (2008).
 21. A. Farooq, J.B. Jeffries, R.K. Hanson, “*In situ* combustion measurements of H₂O and temperature using tunable diode laser absorption near 2.5 μ m,” *Measurement Science and Technology* **19**, 075604 (11pp) (2008).
 22. T. Lee, W. G. Bessler, J. Yoo, C. Schulz, J.B. Jeffries, R.K. Hanson, “Fluorescence quantum yield of carbon dioxide for quantitative UV laser-induced fluorescence in high-pressure flames,” *Applied Physics B* **93**, 677-685 (2008).
 23. M. Gruber, C. Carter, M. Ryan, G. B. Rieker, J. B. Jeffries, R. K. Hanson, J. Liu, T. Mathur, “Laser-based measurements of OH, temperature, and water vapor concentration in a hydrocarbon-fueled scramjet,” *44th AIAA/ASME/SAE/ASEE Joint Propulsion Conference & Exhibit*, 2008, AIAA 2008-5070.
 24. G.B. Rieker, J.B. Jeffries, R.K. Hanson, “Measurements of high-pressure CO₂ absorption near 2.0 μ m and implications on tunable diode laser sensor design,” *Applied Physics B* **94**, 51-63(2009).

25. G.B. Rieker, J.B. Jeffries, R.K. Hanson, T. Mathur, M.R. Gruber, and C.D. Carter, "Diode laser-based detection of combustor instabilities with application to a scramjet engine," *Proceedings Combustion Institute* **32**, 831-838 (2009).
26. A.E. Klingbeil, J.M. Porter, J.B. Jeffries, R.K. Hanson, "Two-wavelength mid-IR absorption diagnostic for simultaneous measurement of temperature and hydrocarbon fuel concentration," *Proceedings Combustion Institute* **32**, 821-829 (2009).
27. A. Farooq, J.B. Jeffries, R.K. Hanson, "Sensitive detection of temperature behind reflected shock waves using wavelength modulation spectroscopy of CO₂ near 2.7 μm ," *Applied Physics B* **96**, 161-173 (2009).
28. H. Li, J.B. Jeffries, R.K. Hanson, "Control of instabilities in a swirl-stabilized flame with a tunable diode laser temperature sensor," *Nihon Nensho Gakkaishi (J. of Combustion Society of Japan)* **50**, 289-296 (2008).
29. J.M. Porter, J.B. Jeffries, R.K. Hanson, "Mid-infrared laser-absorption diagnostic for vapor-phase measurements in an evaporating n-decane aerosol," *Applied Physics B* **97**, 215-225, (2009).
30. J.M. Porter, J.B. Jeffries and R.K. Hanson, "Mid-infrared absorption measurements of liquid hydrocarbon fuels near 3.4 μm ," *J. Quantitative Spectroscopy and Radiative Transfer* **110**, 2135-2147 (2009).
31. X Chao, J B Jeffries, R K Hanson, "Absorption sensor for CO in combustion gases using 2.3 μm tunable diode lasers," *Measurement Science and Technology* **20**, 115201 (9pp) (2009).
32. G.B. Rieker, J.B. Jeffries, R.K. Hanson, "Calibration-free wavelength modulation spectroscopy for measurements of gas temperature and concentration in harsh environments," *Applied Optics* **48**, 5546-5560 (2009).
33. A. Farooq, J.B. Jeffries, R.K. Hanson, "Measurements of CO₂ concentration and temperature at high pressures using *1f*-normalized WMS-*2f* spectroscopy near 2.7 μm ," *Applied Optics*, **48** (2009) 6740-6753.

3.2 Refereed and AIAA Publications to appear 2010

34. B.H. Cheung and R.K. Hanson, "CW laser-induced fluorescence of toluene for time-resolved imaging of gaseous flows," *Applied Physics B*, 2010, in press.
35. J.M. Porter, J.B. Jeffries and R.K. Hanson, "Mid-infrared laser-absorption diagnostic for vapor-phase fuel mole fraction and liquid film thickness," *Applied Physics B*, 2010 in press.
36. A. Farooq, J.B. Jeffries, R.K. Hanson, "High-pressure measurements of CO₂ absorption near 2.7 μm : Line mixing and finite duration collision effects," *Journal of Quantitative Spectroscopy and Radiative Transfer*, 2010 in press.

3.3 Ph.D. Theses with AFOSR Support 2007-2009

1. Hejie Li, *Near-infrared diode laser absorption spectroscopy with applications to reactive systems and combustion control*, Thermosciences Division, Department of Mechanical Engineering, Stanford University; thesis at: <http://thermosciences.stanford.edu/pdf/TSD-172.pdf> August, 2007.
2. Adam E. Klingbeil, *Mid-IR laser absorption diagnostics for hydrocarbon vapor sensing in harsh environments*, Thermosciences Division, Department of Mechanical Engineering, Stanford University; thesis at: <http://thermosciences.stanford.edu/pdf/TSD-175.pdf> December, 2007.
3. David Rothamer, *Development and application of infrared and tracer-based planar laser-induced fluorescence imaging diagnostics*, Thermosciences Division, Department of Mechanical Engineering, Stanford University; thesis at: <http://thermosciences.stanford.edu/pdf/TSD-174.pdf> December, 2007.
4. Gregory Rieker, *Wavelength-modulation spectroscopy for measurements of gas temperature and concentration in harsh environments*, Thermosciences Division, Department of Mechanical Engineering, Stanford University; thesis at: <http://thermosciences.stanford.edu/pdf/TSD-178.pdf> May 2009.
5. Jason Porter, *Laser-based diagnostics for hydrocarbon fuels in the liquid and vapor phases*, Thermosciences Division, Department of Mechanical Engineering, Stanford University; thesis at: <http://thermosciences.stanford.edu/pdf/TSD-182.pdf> November 2009.

3.4 Participation/Presentations at Meetings, Conferences, Seminars

1. R.K. Hanson and J.B. Jeffries, "Diode sensors for combustion and propulsion," *JANNAF 41st Combustion Subcommittee, 29th Airbreathing Propulsion Subcommittee, 23rd Propulsion Systems Hazards Subcommittee*, San Diego, CA, December 2006.
2. R.K. Hanson (invited) "Diode laser sensing: Tools for practical R&D," *Stanford University, Mechanical Engineering, Thermosciences Affiliates Meeting*, February 2007.
3. R.K. Hanson (invited), "Gas sensing based on tunable diode laser absorption," *The Ohio State University, Engineering Winter School*, February 2007.
4. R.K. Hanson (invited), "Planar laser-induced fluorescence (PLIF) imaging of gaseous flows," *The Ohio State University, Engineering Winter School*, February 2007.
5. G.B. Rieker, J.B. Jeffries, and R.K. Hanson, "Comparison of wavelength modulation and direct absorption spectroscopy for measurements of gas temperature in a scramjet combustor," *5th U.S. Combustion Meeting*, San Diego, March 2007.

6. A.E. Klingbeil, J.M. Porter, J.B. Jeffries, and R.K. Hanson, "Two-wavelength mid-IR absorption sensor for simultaneous temperature and n-heptane concentration experiments," *5th U.S. Combustion Meeting*, San Diego, March 2007.
7. J.H. Yoo, T. Lee, J.B. Jeffries, R.K. Hanson, "Detection of trace NO concentrations using 1-D NO-LIF imaging," *5th U.S. Combustion Meeting*, San Diego, March 2007.
8. R.K. Hanson (invited), "Advances in diode laser sensing for propulsion and combustion," *Penn State University*, April, 2007.
9. J.B. Jeffries (invited), R.K. Hanson: "Tunable diode laser sensors for combustion and propulsion applications," *Tunable Diode Laser Conference*, Riems, France, July 2007.
10. H. Li, A. Farooq, R.C. Cook, D.F. Davidson, J.B. Jeffries, and R.K. Hanson, "Rapid measurements of temperature and species concentrations in shock tubes with a diode-laser absorption sensor," *26th International Symposium on Shock Waves*, Göttingen Germany, July 2007.
11. H. Li, A. Farooq, J.B. Jeffries, R.K. Hanson, "High speed diode laser absorption diagnostic for temperature and water vapor in reactive systems," *21st ICDERS Meeting*, Poitiers, France, July 2007.
12. R.K. Hanson (invited), "Recent developments in tunable diode laser sensors and applications," *Gordon Research Conference: Laser Applications to Combustion*, Oxford, England, August 2007.
13. R.K. Hanson (invited), "Tunable diode laser sensors for combustion and propulsion," *University of Texas*, February, 2008.
14. Jay B. Jeffries (invited), "Mid-infrared gas sensing for combustion applications," *Laser Applications to Chemical, Environmental and Security Applications, OSA Topical Meeting*, St Petersburg, FL, March, 2008.
15. Ron Hanson (invited), Tunable diode laser sensors for combustion and propulsion, *University of Michigan*, March, 2008.
16. Ron Hanson (invited), "Diode laser sensing in harsh environments: applications to propulsion and combustion," *Iowa State University*, April, 2008.
17. Ron Hanson (invited), "Diode laser sensing in harsh environments: applications to propulsion and combustion," *University of Science and Technology in China*, April, 2008.
18. Ron Hanson (invited), "Diode laser sensing in harsh environments: applications to propulsion and combustion," *Zhejiang University*, Hangzhou, China, April, 2008.
19. Ron Hanson (invited), "Non-intrusive measurements of velocity and mass flux using tunable diode laser absorption," *AIAA Ground Test Conference*, June, 2008.
20. A. Farooq, J.B. Jeffries, and R.K. Hanson, "Tunable diode laser absorption diagnostics for CO₂ and H₂O in the 2.5- 2.9 μ m spectral region," *WIP poster at 32nd Symp (Int.) on Combustion*, Montreal, August 2008.

21. J.M. Porter, G.L. Pilla, J.B. Jeffries, and R.K. Hanson, "Time-resolved n-decane vapor concentration measurement of CO in a shock-heated evaporating aerosol" WIP poster at 32nd Symp (Int.) on Combustion, Montreal, August 2008.
22. X. Chao, J.B. Jeffries, and R.K. Hanson, "2.3 μ m tunable diode laser absorption measurement of CO in combustion gasses," WIP poster at 32nd Symp (Int.) on Combustion, Montreal, August 2008.
23. X. Chao, J.B. Jeffries and R.K. Hanson, "Tunable diode laser sensing of NO near 5.2 μ m and CO near 2.3 μ m in combustion exhaust gases," paper 11A3 at 6th U.S. National Meeting on Combustion, Ann Arbor, MI, May 2009.
24. A. Farooq, J.B. Jeffries and R.K. Hanson, "Wavelength-modulation spectroscopy of CO₂ near 2.7 μ m for sensitive measurements of temperature in combustion gases," paper 11A4 at 6th U.S. National Meeting on Combustion, Ann Arbor, MI, May 2009.
25. R.K. Hanson (invited), "Tunable diode laser sensing in harsh environments: applications to propulsion and combustion," invited plenary at 6th U.S. National Meeting on Combustion, Ann Arbor, MI, May 2009.
26. R.K. Hanson (invited), "Diode laser sensing in harsh environments: Applications to propulsion and combustion," United Technologies Research Center, East Hartford, CT, May 2009.
27. J.B. Jeffries (invited), R.K. Hanson, "Tunable diode laser sensing applications for propulsion and combustion," Field Laser Applications in Industry and Research 2009, Grainau, Germany, September 6-11, 2009.
28. R.K. Hanson (invited), "Diode laser sensing in harsh environments: Applications to propulsion and combustion," SAOT, Graduate School in Advanced Optical Technology, University of Erlangen, Germany, 2009.
29. R.K. Hanson (invited), "Diode laser sensing in combustion environments," Sandia National Laboratory, CRF, July 2009
30. R.K. Hanson (invited), "Diode laser sensing in harsh environments," Applications to Propulsion and Combustion," *Purdue University*, November 2009
31. R.K. Hanson (invited), "Laser diagnostics of reacting flows: Planar laser-induced fluorescence (PLIF) imaging," *Beijing, China*, December 2009.
32. R.K. Hanson (invited), "Diode laser sensing in harsh environments: Applications to propulsion and combustion," *Beijing and Hangzhou, China*, December 2009.

4 Personnel

Individual researchers partially or fully supported by the program during the reporting period are listed below. All the work has been carried out in the High Temperature Gasdynamics Laboratory, in the Department of Mechanical Engineering, under the supervision of Professor R. K. Hanson.

Research Staff

Dr. Jay B. Jeffries, Senior Research Associate

Current Graduate Research Assistants

Brian Chung
Aamir Farooq
Xing Chao
Sung Hung Pung
Jordan Snyder
John Yoo

Ph.D Degrees Awarded 2007-2009 with Partial AFOSR Support

1. Hejie Li, 2007, currently at GE Global Research
2. Adam E. Klingbeil, 2007, currently at GE Global Research
3. David Rothamer, 2007, currently Assistant Professor, University of Wisconsin
4. Gregory Rieker, 2009, currently postdoctoral associate, Stanford University
5. Jason Porter, 2009, currently Assistant Professor, Colorado School of Mines

5 Interactions and Collaboration with AFRL

In September of 2004, Stanford began collaborating with Dr. Campbell Carter and Dr. Mark Gruber of AFRL to develop tunable diode laser sensing for use in the scramjet test facility at Wright-Patterson. AFRL has hosted a series of measurement campaigns over the past six years. For each measurement campaign, Stanford has built prototype TDL absorption sensor. Each of these sensors has become progressively more complex, and the most recent sensor used six lasers to monitor the absorption by combustion products H_2O and CO_2 as well as gas temperature. Comparison of the combustion product H_2O concentration near the combustor walls was in agreement with PLIF measurements of OH taken by the AFRL researchers, but was less than predicted by CFD at AFRL. These results were reported in paper 5 below. Multiple wavelengths also enabled this sensor to monitor temperature non-uniformity, and paper 6 below describes the use of the sensor to correlate fluctuations in temperature non-uniformity for early warning of back-pressure

induced unstart in the model scramjet. Here we direct the reader to the seven presentations and publications that report the results of this active collaboration:

Grant period 2004-2006

1. M. Gruber, D. Eklund, T. Mathur, J. Jeffries, "In-stream measurements at the exit of dual-mode hydrocarbon-fueled scramjet combustors," *40th Combustion Subcommittee, 28th Airbreathing Propulsion Subcommittee, 22nd Propulsion Systems Hazards Subcommittee, and 4th Modeling and Simulation Subcommittee Joint Meeting*, JANNAF, June 2005.
2. G.B. Rieker, J.T.C. Liu, J.B. Jeffries, R.K. Hanson, T. Mathur, M.R. Gruber, and C. Carter, "Wavelength-Multiplexed Tunable Diode Laser Sensor for Temperature and Water Concentration in a Scramjet Combustor," *41st Joint Propulsion Conf.*, AIAA-2005-3710.
3. J.T.C. Liu, G.B. Rieker, J.B. Jeffries, R.K. Hanson, M.R. Gruber, C.D. Carter, and T. Mathur, "Near-infrared diode laser absorption diagnostics for temperature and water vapor in a scramjet combustor," *Applied Optics* **44** (2005) 6701-6711.

Grant period 2007-2009

4. G.B. Rieker, J.B. Jeffries, R.K. Hanson, T. Mathur, C.D. Carter, M. R. Gruber, "Comparison of wavelength modulation and direct absorption spectroscopy for measurements of gas temperature in a scramjet combustor," *Fifth Meeting of the US Sections of the Combustion Institute*, San Diego, March, 2007.
5. M. Gruber, C. Carter, M. Ryan, G. B. Rieker, J. B. Jeffries, R. K. Hanson, J. Liu, T. Mathur, "Laser-based measurements of OH, temperature, and water vapor concentration in a hydrocarbon-fueled scramjet," *44th AIAA/ASME/SAE/ASEE Joint Propulsion Conference & Exhibit*, 2008, AIAA 2008-5070.
6. G.B. Rieker, J.B. Jeffries, R.K. Hanson, T. Mathur, M.R. Gruber, and C.D. Carter, "Diode laser-based detection of combustor instabilities with application to a scramjet engine," *Proc. Comb. Inst.* **32**, 831-838 (2009).
7. G.B. Rieker, J.B. Jeffries, R.K. Hanson, "Calibration-free wavelength modulation spectroscopy for measurements of gas temperature and concentration in harsh environments," *Applied Optics* **48**, 5546-5560 (2009).

The TDL sensor measurement campaigns have transitioned from research on diode laser sensing to the use of TDL sensors for scramjet research and development, and this evolution is well documented in the joint publications listed above.

6 New Discoveries, Inventions, Patent Disclosures

No patent or invention disclosures.

7 Honors/Awards

Professor Ronald K. Hanson recieved the Alfred C. Egerton Gold Medal of the Combustion Institute in 2008 "For distinguished, continuing and encouraging contributions to the field of combustion"

Lifetime awards of Professor Ronald K. Hanson:

- 1990 Fellow, Optical Society of America (OSA)
- 1990 Woodard Chair of Mechanical Engineering, Stanford University
- 1996 Aerodynamic Measurement Technology award from the AIAA (first recipient)
- 1997 Fellow, American Institute of Aeronautics and Astronautics (AIAA)
- 2002 Elected to the National Academy of Engineering (NAE)
- 2002 Silver Medal of the Combustion Institute
- 2004 Fellow, American Society of Mechanical Engineers (ASME)
- 2005 Propellants and Combustion award from the AIAA
- 2008 Egerton Gold Medal of the Combustion Institute